ENHANCEMENT OF CAVITATION INTENSITY IN CO-FLOW AND ULTRASONIC CAVITATION PEENING

A Dissertation
Presented to
The Academic Faculty

by

AMEY VIDVANS

In Partial Fulfillment
of the Requirements for the Degree
Doctor of Philosophy in the
George W. Woodruff School of Mechanical Engineering

Georgia Institute of Technology
December 2022

ENHANCEMENT OF CAVITATION INTENSITY IN CO-FLOW AND ULTRASONIC CAVITATION PEENING

Approved by:

Dr. Shreyes Melkote, Advisor
School of Mechanical Engineering
Georgia Institute of Technology

Dr. Minami Yoda
School of Mechanical Engineering
Georgia Institute of Technology

Dr. Richard Neu
School of Mechanical Engineering
Georgia Institute of Technology

Dr. Christopher Saldana
School of Mechanical Engineering
Georgia Institute of Technology

Dr. James Castle
Boeing Research and Technology
The Boeing Company

Date Approved: December 12th, 2022

To my family and friends

who kept me going through tough times

ACKNOWLEDGEMENTS

I would like to thank my advisor, Prof. Melkote for his guidance and help. The work would not have been possible without his patience. I would also like to thank my family and friends, some who have graduated and some who are still here. I would also like to thank all the Montgomery Machining Mall (MMM) staff. I would like to specifically thank Dr. Yoda for helping me fix major portions of the thesis and make sense of the results. Lastly, I thank the other members of the committee, Dr. Castle, Dr. Saldana and Dr. Neu for their time to be on my committee.

TABLE OF CONTENTS

LIST OF TABLES

LIST OF FIGURES

LIST OF IMPORTANT SYMBOLS AND ABBREVIATIONS

mm	millimeter
m	meter
s	second
µs	micro-second
kPA	kilopascal
MPa	megapascal
XRD	X-ray-Diffraction
CFD	Computational Fluid Dynamics
RANS	Reynolds Averaged Navier Stokes
LES	Large Eddy Simulation
PEO	Poly-Ethylene Oxide
wppm	parts per million by weight
SP	Shot Peening
LSP	Laser Shock Peening
WCP	Water Cavitation Peening
WJP	Water Jet Peening
FEM	Finite Element Method
JIS	Japanese Industrial Standards
CJA	Cavitating Jet in Air
CJW	Cavitating Jet in Water
St	Strouhal Number
WEDM	Wire Electro Discharge Machining
C_d	Coefficient of discharge
L_o	Length of inner jet orifice
d	diameter of inner jet orifice
CMM	Coordinate Measuring Machine
$nSOD$	Normalized Standoff Distance
Hz	Hertz

kHz	Kilo Hertz
PSD	Power Spectral Density
MHz	Mega Hertz
PC	Personal Computer

SUMMARY

Water cavitation peening is a surface treatment process used to generate beneficial compressive residual stresses while being environmentally sustainable. Compressive residual stresses generated by the collapse of the cavitation cloud at the workpiece surface result in enhanced high cycle fatigue and wear performance. Co-flow water cavitation peening, a variant of cavitation peening involves injection of a high-speed jet into a low-speed jet of water, which makes the process amenable to automation and imparts the variant with the ability to process large structural components. Ultrasonic cavitation peening, another variant of cavitation peening, is used for peening small areas. However, an increase in cavitation intensity is needed to reduce the processing time for practical applications and to enhance process capabilities for a wide range of materials in both these variants. An experimental investigation along with numerical modelling is presented to demonstrate cavitation intensity enhancement through suitable modifications to the inner jet nozzle design in co-flow water cavitation peening. Particularly, the effects of upstream inner jet organ pipe nozzle geometry, inner jet nozzle orifice taper, and inner jet nozzle orifice length are studied to show enhanced cavitation intensity, measured via extended mass loss tests, strip curvature and residual stress measurements, high-speed videography, and impulse pressure measurements.

It is found that the optimum inner jet organ pipe nozzle design, which generates enhanced pressure fluctuations through the introduction of a resonating chamber in the upstream section of the inner jet nozzle, generates 61% greater mass loss compared to the unexcited inner jet nozzle. Strip curvature, high speed imaging, and impulse pressure measurements support the mass loss results. Finally, residual stresses generated with the optimum organ pipe nozzle are shown to be deeper and more compressive than those generated with the unexcited nozzle design.

The inner jet nozzle variants with diverging, zero and converging tapers are investigated experimentally and numerically to understand their influence on cavitation intensity. It is shown that the converging taper nozzle generates greater cavitation intensity, measured via mass loss and strip curvature measurements, than the zero and diverging taper nozzles. Impulse pressure measurements show the greater frequency of high-intensity events generated by the converging taper nozzle compared to the zero and diverging taper nozzles. Computational fluid dynamics (CFD) simulations help explain the experimental findings.

Four nozzle variants with varying inner jet nozzle orifice length to orifice diameter ratios of 1,2,5 and 10 are investigated experimentally and numerically. The inner jet nozzle with an orifice length to orifice diameter ratio of 2 is shown to generate greater cavitation intensity than the other inner jet nozzles.

A PEO aqueous solution (cavitation media) with 1000 parts per million by weight (wppm) polymer concentration is shown to enhance cavitation intensity by 69% over cavitation media with only water. High speed videography, impulse force, and surface roughness measurements confirm the greater cavitation activity in the 1000 wppm PEO aqueous solution. This demonstrates that suitable modifications can be engineered in the cavitation media to enhance cavitation intensity in ultrasonic cavitation peening.

Thus, this thesis presents experimental and numerical investigations leading to superior inner jet nozzle design in co-flow cavitation peening and an experimental investigation of the role of polymer additives for suitable modification of cavitation media to enhance cavitation intensity in ultrasonic cavitation peening.

CHAPTER 1. INTRODUCTION

The surfaces of safety-critical metal components used in aerospace applications are often subjected to surface treatment to improve their high cycle fatigue, fretting fatigue, and stress corrosion cracking resistance [1-4]. Surface treatment processes such as shot peening and laser shock processing are used widely for industrial applications [5,6]. Other surface modification processes such as deep rolling and ball burnishing are also utilized for industrial applications albeit less so [7,8]. Processes such as water jet peening have been explored in research for treatment of metal surfaces but are not commonly used in practice [9]. The most widely used peening process in industry is Shot Peening (SP), which involves the impact of high velocity spherical steel or ceramic shots to produce inhomogeneous plastic deformation in the surface layers of metallic materials [10]. This plastic deformation produces compressive residual stress, which increases the high-cycle fatigue, fretting wear, and stress corrosion cracking resistance of the metal surface [5,11,12]. However, shot peening is often characterized by significant surface roughening and contamination that negatively influence the low-cycle fatigue and corrosion behavior of the treated component [13,14]. In Laser Shock Peening (LSP), due to the ablation of a sacrificial coating on the component to be treated, a shockwave is formed, which plastically deforms the metallic surface beneath the sacrificial layer [6]. Even though LSP is capable of generating high compressive residual stresses at large depths with no surface contamination, it involves long setup times and high operating costs, which limit its industrial application [11,15]. Less frequently used techniques such as ball burnishing cannot be applied to complex and thin-walled geometries [16]. Water jet peening utilizes the water hammer pressure of a high-pressure jet discharged in air to generate plastic deformation and compressive residual stresses [9]. However, the high pressures required (~ 600 MPa) make the process impractical for large scale industrial application.

Water cavitation peening utilizes a cavitation cloud, which collapses on the surface to be treated, to induce inhomogeneous surface plastic deformation and compressive residual stresses [17,18]. The cloud is typically generated through either ultrasonic or hydrodynamic means. Ultrasonic cavitation peening involves a high frequency sonifier and horn assembly submerged in a cavitating media, typically water, that generates a cavitation cloud [18]. Cavitation peening through hydrodynamic cavitation can be achieved via submerged or co-flow nozzle configurations [19]. In submerged water cavitation peening, a high-pressure jet of water is injected into a stationary column of water, which generates a pulsating cloud [17]. In co-flow water cavitation peening, a high-pressure jet of water is injected into an encapsulating low-pressure water jet, which also generates a pulsating cavitation cloud due to shearing action between these co-flowing jets [20]. Schematics of the three variants of water cavitation peening process variants are shown in Fig. 1-1.

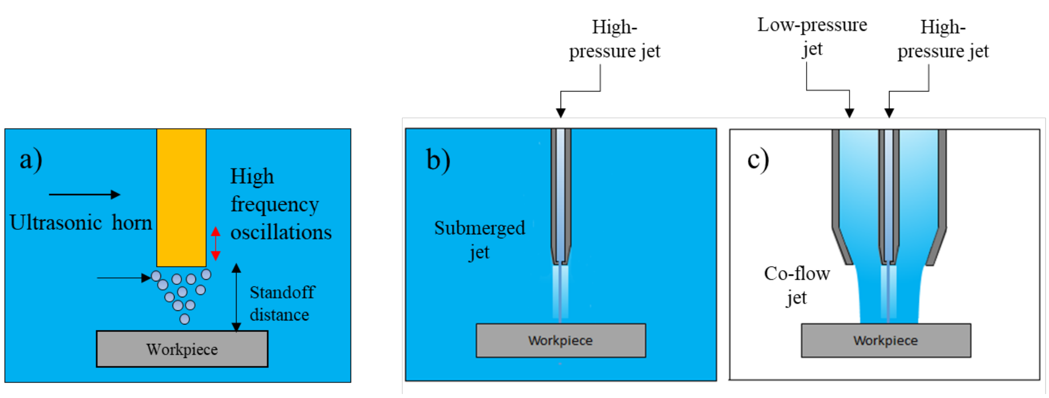

Fig. 1-1 Schematics of a) ultrasonic cavitation peening b) submerged cavitation peening and c) co-flow cavitation peening.

A limitation of submerged cavitation peening is that it necessitates submergence of the component to be peened in water, which restricts the size of the component to be peened. Co-flow water cavitation peening, where a high-pressure jet of water is injected into a surrounding low-pressure jet, is more amenable to peening large components since the nozzle assembly discharging the co-flow jet can be mounted on a gantry system or a robotic arm. Ultrasonic cavitation peening on the other hand is suited for treatment of small areas [18,21]. There is also no detrimental surface contamination if a suitable cavitation media is used in both these processes. This thesis focuses on co-flow water cavitation peening and ultrasonic cavitation peening due to the abovementioned advantages.

However, there is a need to reduce the processing time in co-flow water cavitation peening and ultrasonic cavitation peening and to expand the range of materials that can be treated, particularly higher yield strength metals. This can be realized through increases in cavitation intensity of the respective processes. Scaling of nozzles that produce the co-flow jet and increasing the inner jet velocity in co-flow water cavitation peening to enhance shear cavitation may necessitate equipment of higher capacity, which may not always be feasible. Hence, nozzle design changes that can increase cavitation intensity without an increase in equipment capacity are desired. An alternate modality to increase cavitation intensity is by suitable modification of cavitation media to enhance cavitation intensity. However, there is limited literature on design changes that enhance cavitation intensity in co-flow water cavitation peening. A limited study on nozzle design shows the influence of inner jet nozzle design on cavitation intensity in co-flow cavitating water jets used for mining applications [22]. However, a detailed investigation of the effects of inner jet nozzle design on cavitation intensity in co-flow water cavitation peening is lacking. The cavitation behavior and cavitation intensity are highly influenced by the design of the high-pressure inner jet nozzle seen in Fig. 1-2.

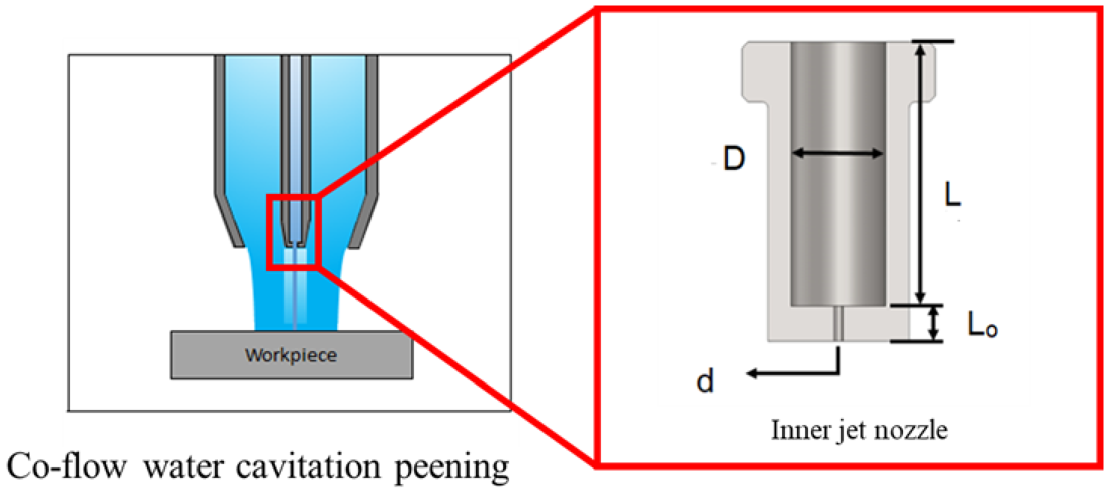

Fig. 1-2 Co-flow water cavitation peening with the inner jet nozzle in the inset.

There are a few studies that show the potential for increased cavitation intensity in ultrasonic cavitation peening through addition of certain water-soluble polymer additives although the studies are not directed towards peening for surface treatment applications [23-25]. Thus, suitable modification of cavitation media may enhance cavitation intensity in ultrasonic cavitation peening.

In summary, despite the advantages of co-flow water cavitation peening and ultrasonic cavitation peening, there is a need for a better understanding of modalities to increase cavitation intensity in these processes.

1.1 Research Objectives and Approach

This thesis aims to research inner jet nozzle designs and the use of polymer additives to enhance cavitation intensity in water cavitation peening. The following specific research objectives are framed:

1. Design, develop, and evaluate organ pipe nozzles for co-flow water cavitation peening.

2. Evaluate and elucidate the effect of inner jet nozzle orifice taper on cavitation intensity in co-flow water cavitation peening.
3. Investigate and elucidate the effect of inner jet nozzle orifice length on cavitation intensity in co-flow water cavitation peening.
4. Investigate the effect of polymer additives in water on cavitation intensity in ultrasonic water cavitation peening.

These research objectives are addressed through experiments and numerical modeling. Specifically, cavitation intensification for co-flow and ultrasonic cavitation peening is pursued through two modalities: 1) inner jet nozzle design, and 2) polymer additives in cavitation media to enhance peening ability. The first research objective is achieved through design, testing, and evaluation of an upstream inner jet organ pipe nozzle geometry. The increased cavitation intensity is demonstrated through extended mass loss and strip curvature experiments. Cloud behavior is investigated through impulse pressure measurements and high-speed videography. Residual stress measurements via X-Ray Diffraction (XRD) are used to show the increased peening ability of co-flow cavitating jets with upstream inner jet organ pipe nozzle geometry. Next, the effect of inner jet nozzle orifice taper on cavitation intensity is evaluated. The taper is defined by the slope angle or alternatively with the area reduction of the inner jet nozzle orifice measured at the entry and exit of the inner jet flow. Thus, a nozzle orifice with a diverging, zero and converging taper have negative, zero and positive values of area reduction respectively. The enhanced cavitation intensity is evaluated through extended mass loss and strip curvature tests. Cloud behavior is investigated through impulse pressure measurements. Computational fluid dynamics (CFD) simulations are performed to explain and gain mechanistic insights into the experimental results. Lastly, the effect of inner jet nozzle orifice length on cavitation intensity is investigated and evaluated through extended mass loss and strip curvature measurements.

The second modality of cavitation intensity enhancement focuses on the ultrasonic cavitation peening process, where the effect of soluble polymer additives to the cavitation media on cavitation intensification is investigated. Extended mass loss, impact force measurements, high speed videography, and surface morphology modification are analyzed to demonstrate the ability of polymer additives to enhance cavitation intensity. These research objectives and the corresponding approaches are summarized graphically in Fig. 1-3.

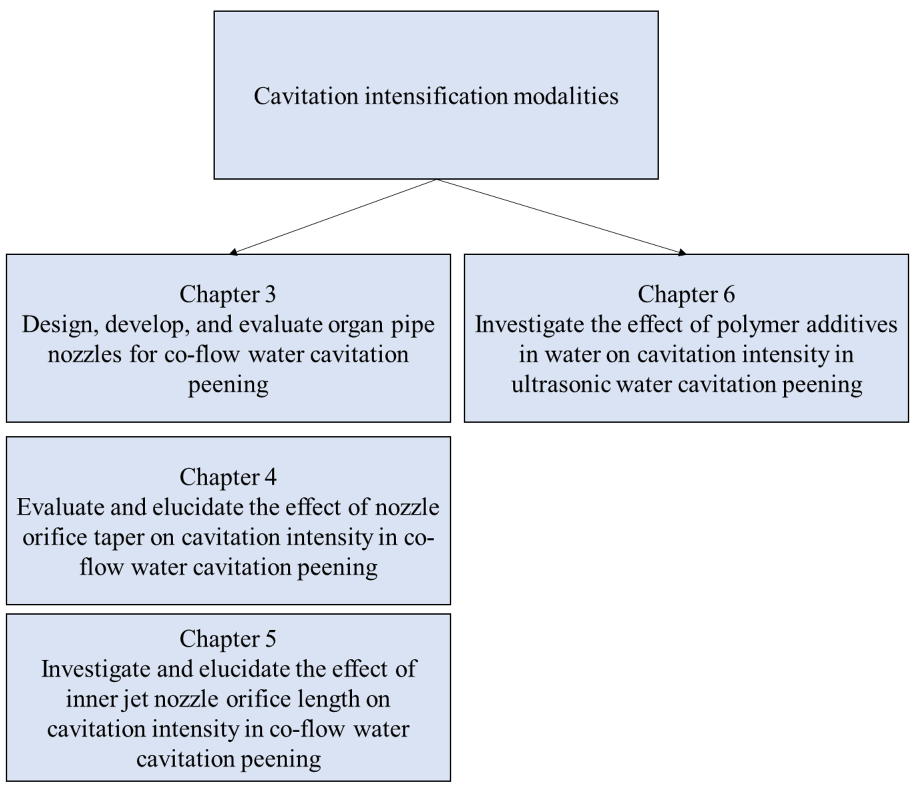

Fig. 1-3 Summary of approach.

1.2 Dissertation Outline

The outline of the dissertation is as follows. Chapter 2 presents a detailed literature survey of the specific topics relevant to the research objectives of this thesis. Chapter 3 focuses on the effect of inner jet organ pipe nozzle geometry on cavitation intensification and peening. Chapter 4 elucidates the effect of inner jet nozzle orifice taper on cavitation intensity and peening characteristics. Chapter 5 covers the effect of inner jet nozzle orifice length in co-flow water cavitation peening. Chapter 6 investigates the role of certain polymer additives on cavitation generation in ultrasonic cavitation peening since ultrasonic cavitation peening is quite amenable to experimentation with smaller volumes of cavitation media, which facilitates experimentation. Finally, the major conclusions and recommendations for future work are summarized in Chapter 7.

CHAPTER 2. LITERATURE REVIEW

This section contains a review of prior work relevant to the topics addressed by this thesis. The specific areas reviewed include 1) Peening, 2) Cavitation erosion, 3) Water cavitation peening, 4) Cavitation intensification in water cavitation peening.

Peening and surface treatment processes have been extensively used for surface modification and surface integrity enhancement for a range of applications in the aerospace and nuclear industries. The common objective of these processes is enhancement of high-cycle fatigue, fretting fatigue, and stress corrosion cracking performance through introduction of compressive residual stresses. This chapter presents a review of the current state of knowledge in peening processes along with a discussion of the limitations and disadvantages. A closely related area of research is the cavitation erosion of structural metals, which is undesirable in peening but can aid in understanding material response during cavitation peening. An outline of the development of water cavitation peening and different modalities of cavitation intensification follows the discussion on cavitation erosion.

2.1 Peening processes

Widely used processes for peening of critical components include Shot Peening (SP), Laser Shock Peening (LSP) [26,27]. Water Cavitation Peening (WCP) and Ball burnishing are lesser used processes for surface modification [16,19]. Water Jet Peening (WJP) has also been researched in academia for surface modification [9]. Due to inhomogeneous plastic deformation that occurs in the metal surface layer in all the above cited processes, compressive residual stresses are generated, which are known to increase surface integrity. However, due to the deformation induced by these processes, there is typically an undesirable increase in surface roughness. It is noted that due to the inherent differences in these processes, material response is varied [28].

The most widely used process among peening processes is shot peening, which employs spherical steel or ceramic shots that impact the metal surface to be treated. These impacts produce surface pitting and inhomogeneous plastic deformation, which results in generation of beneficial compressive residual stresses and undesirable surface roughness. The effect of compressive residual stresses generated by SP on high cycle fatigue, fretting fatigue, and corrosion life have been explored by many researchers for a range of materials including aluminum alloys (20xx, 70xx series), titanium alloys, and steel [29-35]. A schematic of shot peening and a depiction of resulting the residual stress depth profile in the treated surface can be seen in Fig. 2-1.

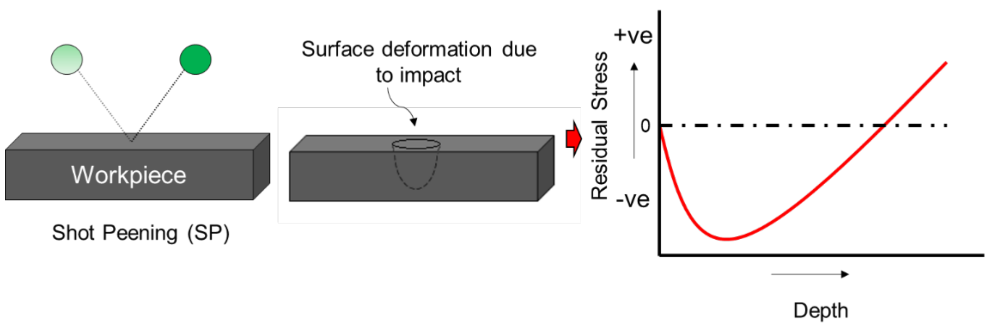

Fig. 2-1 Schematic of Shot Peening (SP).

Benedetti et al. have shown the effects of shot peening on residual stress distribution in Al 7075-T651, which can be seen in Fig. 2-2 for the most intense shot peening treatment Z 150 [29].

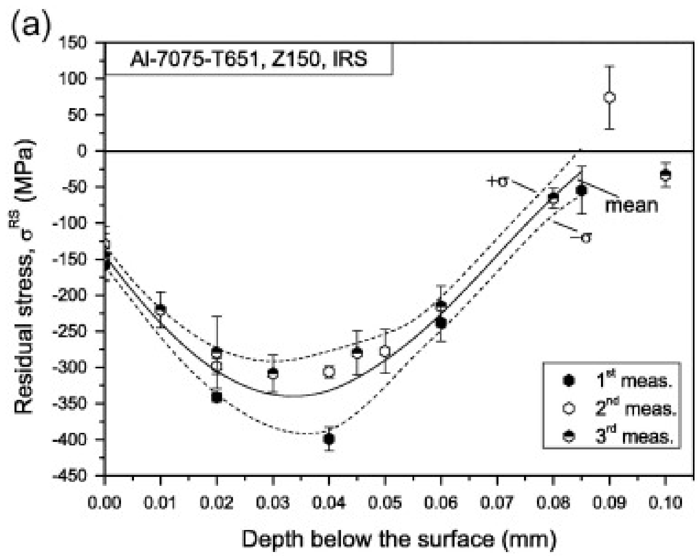

Fig. 2-2 Longitudinal residual stress profile (solid line) of the sample subjected to Z150 treatment by Benedetti et al [29].

The high cycle fatigue response of the samples peened with different shot peening intensities including Z 150 can be seen in Fig. 2-3.

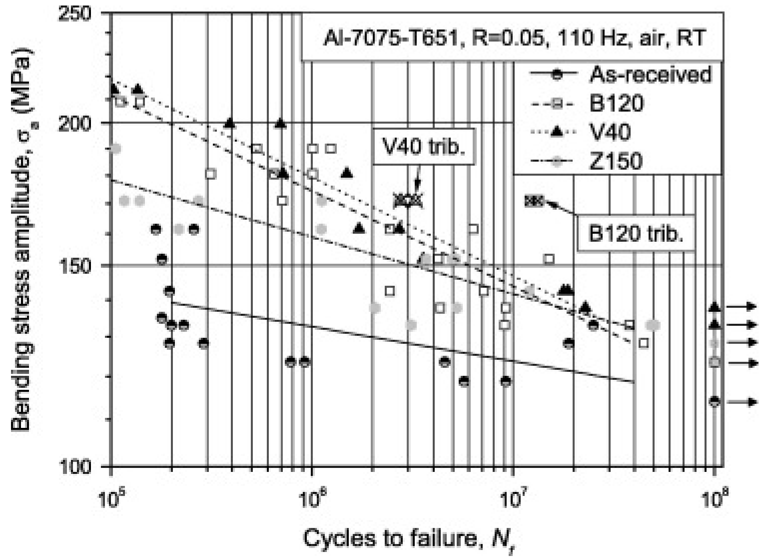

Fig. 2-3 Pulsating bending fatigue curves from Benedetti et al. showing improved performance of peened samples as compared to as received conditions [29].

The increase in high cycle fatigue life is attributed to the presence of compressive residual stresses in the surface layers, which prevent crack initiation and growth [36].

Martin et al. investigated the effect of shot peening induced residual stresses on fretting fatigue life for Al 7075-T651 [30]. The increase in fatigue performance, measured in terms of fatigue life, is plotted for four (4) different residual stress conditions in Fig 2-4. It can be seen that the fretting fatigue life is greater for the samples subjected to shot peening as compared to samples with no treatment.

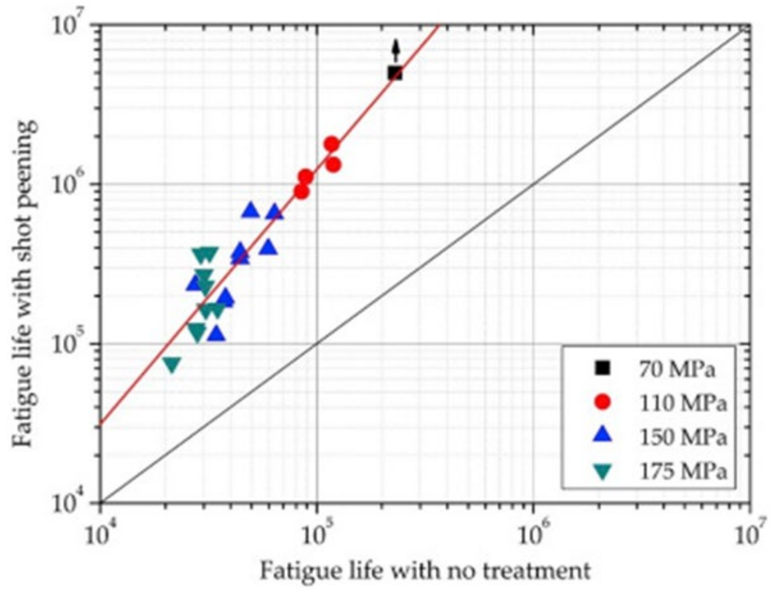

Fig. 2-4 Fatigue life for shot peened specimens with different residual stresses vs. life with as-machined specimens (no treatment) for Al 7075- T651 [30].

Numerical modeling of the SP process has also been carried out via finite element models for prediction of residual stress distribution [37-39]. However, the models are restricted to simulating a few impacts only, which is not representative of a process that involves multiple impacts. Other surface modification techniques similar to shot peening include Ultrasonic Shot Peening, Hammer Peening, and rotary flap peening [40-42]. However, as noted earlier, SP tends to cause excessive surface roughening, which can lead to stress concentration in the pitted region and detrimental surface contamination [43,44].

Laser Shock Peening (LSP) is a surface modification technique that can introduce compressive residual stresses up to large depths with less surface roughening compared to shot peening. LSP can be performed in either the direct mode or the confined mode with pulsed Nd-glass lasers with output energies of 80-100J [45]. A schematic of the process in the direct and confined modes can be seen in Fig. 2-5.

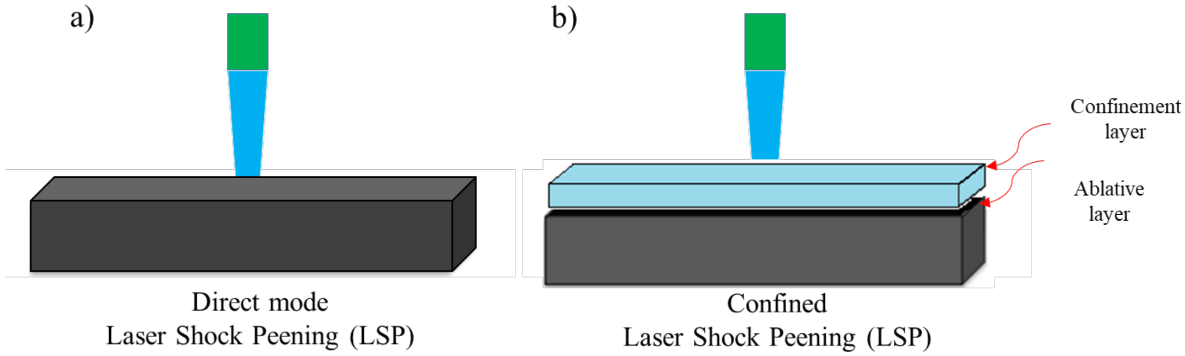

Fig. 2-5 Schematic of laser shock peening in a) direct mode and b) confined mode.

In the direct mode, the laser directly irradiates the surface of the metal, which, upon ablation, releases a shock wave. In the confined mode, a small ablative sacrificial layer and a dielectric "confinement" layer are overlayed on the metal surface. The confinement layers may be stationary water, flowing water, or glass [45,46]. The plasma that is generated in this process is responsible for the shockwave, which propagates and plastically deforms the material. In the direct mode, the shock wave is generated by direct ablation of the metal surface. During the "blow off", which is the expanding plasma created by ablation, a mechanical impulse and shockwave are generated [46]. In confined laser shock peening, this plasma is generated by the ablation of the opaque overlay material and is confined to the gap between the overlay and confining transparent medium. This prevents thermal ill-effects such as ablation on the underlying metal substrate, which may damage the work surface. Due to the confinement, greater pressures are generated, which results in a more intense shock wave compared to direct laser shock peening [45]. The inhomogeneous surface deformation generates compressive residual stresses like other processes [47]. A raster scan of laser shock peening may be utilized to generate residual stresses over large surface areas. Increases in high-cycle fatigue, fretting fatigue, and stress corrosion failure life in aluminum alloys due to laser shock peening has been documented by several researchers

[27,48,49]. Laser shock peening, however, may require long setup times and extensive surface preparation, making industrial application uneconomical [15].

Water Jet Peening (WJP) is a peening technique that has been investigated for generating compressive residual stresses through water hammer pressure induced surface plastic deformation. The water hammer pressure is produced by the impact of a high-pressure water jet (> 500 MPa) [9]. A schematic of WJP is shown in Fig. 2-6.

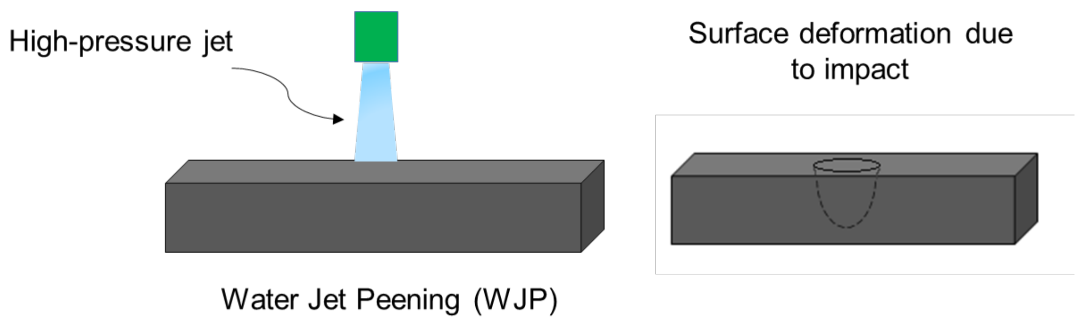

Fig. 2-6 Schematic of Water Jet Peening (WJP) producing surface deformation.

Increases in fatigue life of aluminum alloy Al-7075-T6 using water jet peening (WJP) have been reported by Ramulu et al. [50]. Modeling of WJP through finite element analyses for residual stress prediction has augmented the experimental studies reported in the literature [51]. Lesser used peening processes like ball burnishing and deep rolling also impart inhomogeneous plastic deformation to the workpiece surface via suitable contacting tools [52,53]. Schematics of these processes are shown in Fig. 2-7. However, these processes can only be applied to simple geometries [52,53]

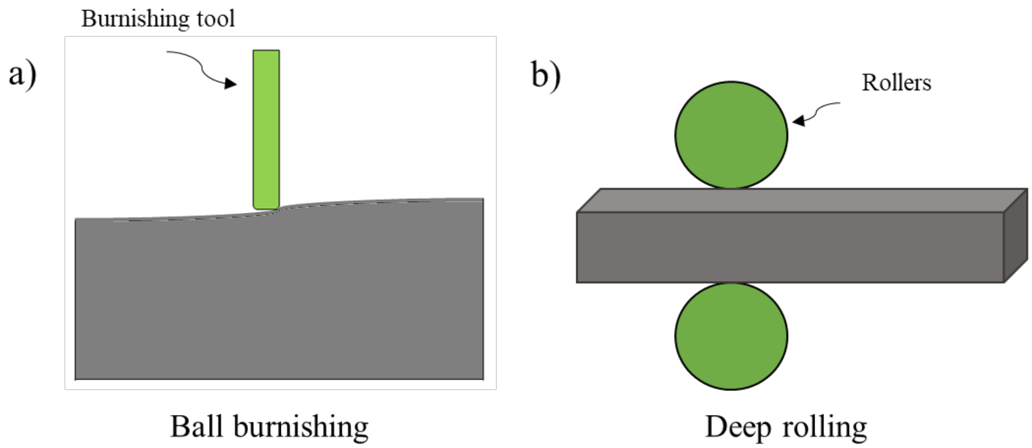

Fig. 2-7 Schematic of a) ball burnishing and b) deep rolling.

2.2 Cavitation erosion

Cavitation erosion refers to the undesirable damage produced by cavitation cloud collapse on solid surfaces, and especially metals, which are of particular interest [54]. Cavitation erosion commonly occurs when a metal surface is exposed to hydrodynamic and ultrasonic cavitation [55,56]. Cavitation bubbles are created in fluids when the static pressure drops below a critical threshold in either of these modes of cavitation [57]. The cavitation cloud is an agglomeration of many individual cavitation bubbles that collapse either in the bulk liquid or on impact at a solid boundary [58]. A high-speed micro reentrant jet and the shockwave generated upon cloud collapse impact the metal surface, which undergoes plastic deformation, producing damage accumulation leading to fatigue and ultimately failure [59-61]. However, before actual erosion begins, there exists an incubation period where there is negligible mass loss and the plastic deformation in the form of localized pits generates compressive residual stresses [62]. Cavitation erosion induced surface pitting and high-pressure impulse pressure measurement are of particular interest since they provide useful ways of characterizing cavitation erosion [63].

The pits produced during cavitation erosion are of particular interest as they are an indicator of cavitation intensity and help in understanding cavitation loading and impact pressures [63]. It is seen from Fig. 2-8 that there is a strong linear relationship between impact load and pit volume. Impact loads are estimated from indentation stress-strain curves while the pit volume is obtained from stylus measurements.

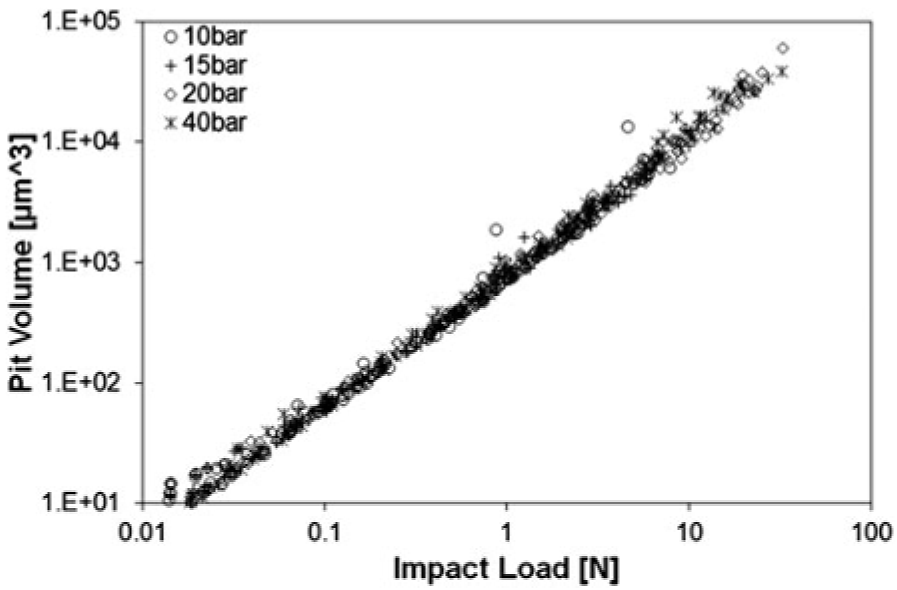

Fig. 2-8 Pit volume–impact load trends for 10,15,20,40 bar upstream pressures [63].

Distributions of the impact loads by the frequency of their occurrence is shown in Fig 2-9. The distribution consists of many impact events characterized by very low impact loads with a few events at higher impact loads.

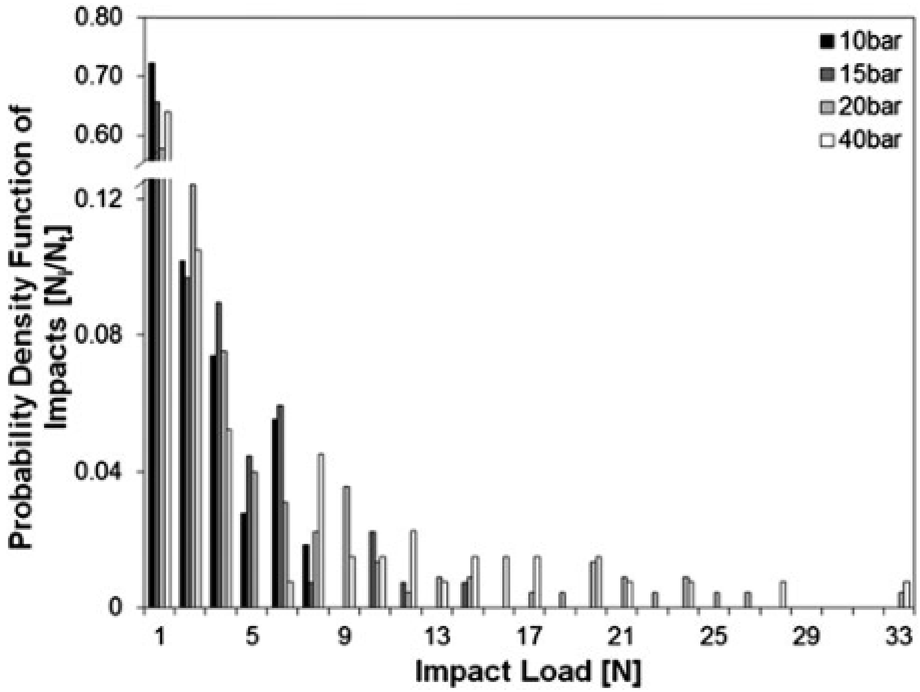

Fig. 2-9 Histogram of the number of impacts normalized by total number of impacts versus the impact load for four tested upstream pressures [63].

Marcon et al. utilized pitting tests and FEM analysis to obtain information regarding cavitation impulse events [64,65]. Sensors such as high-frequency pressure transducers, PVDF thin film sensors, and acoustic hydrophones have also been utilized for cavitation intensity measurement [66-68].

Singh et al. [66] utilized high frequency pressure transducers to measure the behavior of cavitation cloud produced by ultrasonic horns. It was found that the distribution of cavitation events follows an exponential distribution very similar to the results obtained from the pitting analysis of Carnelli et al. [63] and Marcon [64]. A schematic of the experimental setup and the distribution of the frequency of peak amplitudes is given in Fig 2-10. A similar finding of the distribution of impulse loads was reported by Soyama et al. [67].

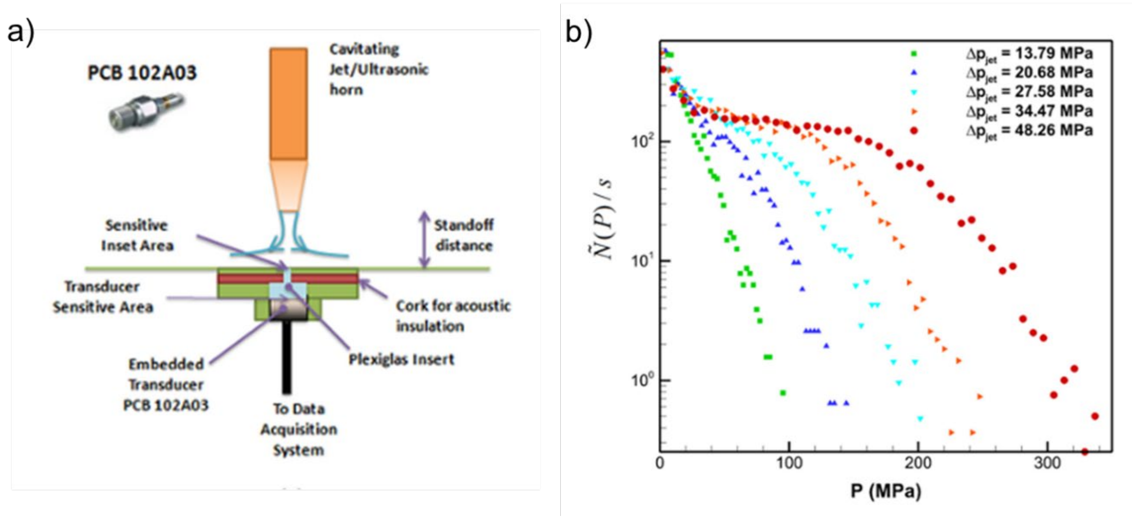

Fig. 2-10 a) Schematic of high frequency pressure transducer for impulse pressure measurements, and b) distribution of peak amplitudes for different jet pressures [66].

Hydrophones have also been used to characterize the cavitation noise – a measure of cavitation intensity – primarily for acoustic or ultrasonic cavitation [68]. The filtering of the harmonics of the cavitation source is required to remove the stable cavitation field and obtain a measure of the cavitation noise, a measure of the cavitation intensity. However, there are several drawbacks to this approach as explained by Jae Hee Song et al. [69]

2.3 Water cavitation peening

Cavitation generated through either hydrodynamic or ultrasonic means has been used to peen metallic surfaces [18,20,70-72]. Cavitation peening using hydrodynamic means can be performed via the submerged or the co-flow configuration. Schematics of both process variants are shown in Fig. 1-1b and c.

In submerged water cavitation peening, a high-pressure jet of water is injected into a stationary column of water, which generates cavitation in the low-pressure regions of vortices created by the shearing action between the high-pressure jet and the stationary column of water [19,70]. In co-flow water cavitation peening or simply co-flow cavitation peening, a high-pressure jet of water is injected into an encapsulating low-pressure water jet, which produces cavitation due to the shearing action between the high pressure and low-pressure jets [20]. Cavitation peening using ultrasonic excitation is realized by a high frequency ultrasonic horn immersed in a fluid, usually water or an aqueous solution, that produces cavitation due to a fluctuating pressure field generated by the ultrasonic excitation [72]. Peening by ultrasonic cavitation has been explored for surface modification and has been shown to introduce beneficial compressive residual stresses [72]. A schematic of ultrasonic cavitation peening is shown in Fig. 1-1a.

Soyama et al. observed the pulsating cavitation cloud produced by a high-speed submerged jet through high-speed flow visualization [73]. Subsequently, useful parameter spaces for cutting and peening were identified by observations of erosion in aluminum samples [74]. Vijay et al. utilized similar cavitating water jets in both submerged and co-flow configurations for cutting of rocks and other materials [22].

Fatigue life of aluminum alloy JIS Z2274 has been shown to increase with submerged cavitation peening [17]. The increase in high cycle fatigue life of the aluminum alloy is shown in Fig. 2-11.

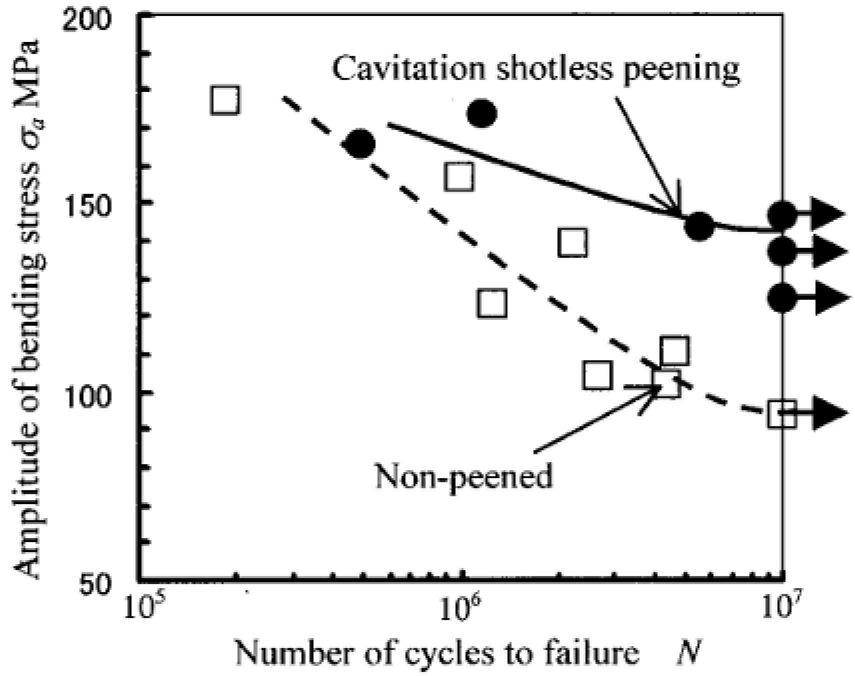

Fig. 2-11 Improvement of fatigue strength of JIS Z2274 by cavitation peening [17].

Similarly, an increase in high cycle fatigue strength has also been seen with co-flow cavitation peening [75]. For example, the increase in fatigue life of stainless steel JIS SUS316L subjected to co-flow cavitation peening is shown in Fig 2-12. In the figure, CJA refers to cavitating jet in air, referred to as co-flow cavitation peening in this thesis, and CJW refers to cavitating jet in water or submerged cavitation peening. It is noted from this study that the high cycle fatigue life improvement produced by co-flow cavitation peening may be greater than the high cycle fatigue life improvement produced by submerged cavitation peening.

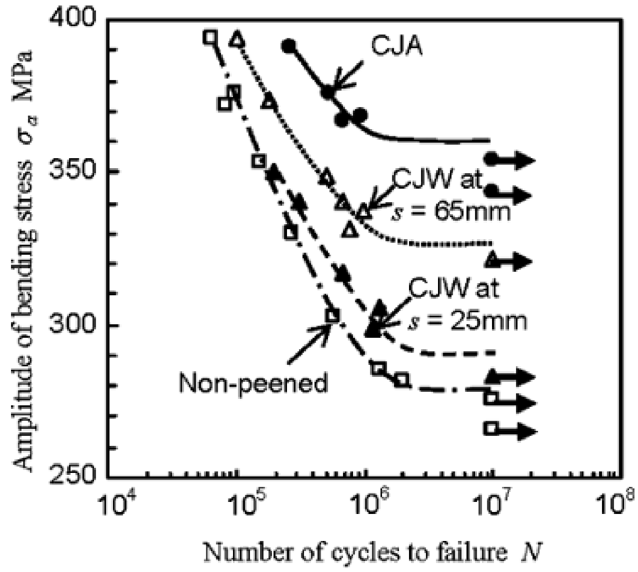

Fig. 2-12 Improvement of fatigue strength peened by CJA (Cavitating Jet in Air) and CJW (Cavitating Jet in Water) [75].

Marcon et al. compared the surface roughness produced by co-flow water cavitation peening and showed that co-flow water cavitation peening yields lower surface roughness than shot peening [76]. Also, there are advantages of co-flow cavitating jets over submerged jets such as amenability to automation and ability to process larger workpieces.

2.4 **Cavitation intensification in water cavitation peening**

Due to similarities with submerged cavitation peening, literature on submerged water jets is relevant as well. Qin et al. [77] have showed that cavitation intensity can be enhanced by aeration of the high-pressure jet. Aeration of the high-pressure jet has the potential to increase the availability of cavitation nuclei, thus increasing the incidence of cavitation. Their study showed that an increase in aeration led to a decrease in the time required to reach residual stress saturation, an increase in the peak compressive residual stress, and an increase in the depth to which compressive residual stresses are generated. Peng et al. [78] have demonstrated an increase in cavitation intensity by the addition of silica microparticles in the working fluid. The silica microparticles are believed to act as cavitation nucleation sites in addition to their role as abrasive projectiles accelerated by cavitation collapse. A critical concentration of silica particles was determined and shown to increase the cavitation intensity by ~ 90%, measured in terms of the mass loss, compared to the absence of silica particles.

While such studies have shown an enhancement of cavitation intensity, a significant change in the overall design of the system is required to introduce aeration in the high-pressure jet. There is also the potential for damage to the high-pressure pump due to introduction of abrasive silica particles.

It has been shown by Soyama et al. [79] that the nozzle design influences cavitation intensity in submerged water cavitation peening. Through the introduction of an upstream cavitator and a downstream guide pipe, the availability of cavitation nuclei, produced by bubble formation and collapse in the upstream cavitator, is increased. The guide pipe is believed to influence the cavitation cloud pulsation frequency that allows for larger cavitation clouds to form. The optimized design with an upstream cavitator and the downstream guide pipe led to a 320% increase in cavitation intensity quantified by the curvature of a duralumin strip.

Soyama [80] has also shown that cavitation intensity can be enhanced by generating pulsations in the cavitating jet through suitable shaping of the nozzle outlet geometry in submerged cavitation peening. The nozzle outlet geometry was shaped in the form of a Helmholtz resonator. An optimum Strouhal number (St) was determined and experimentally shown to increase the cavitation intensity by ~ 300%. The Strouhal number (St) is a dimensionless number quantifying the pulsation frequency of a flow [81].

Johnson et al. [82] have shown the effect of upstream organ pipe geometry on intensification of cavitation for deep sea drilling. The pressure losses in an organ pipe are small, which make them suitable for cavitation intensity enhancement without an increase in pressure requirements. Pressure oscillations in the exiting jet are amplified due to matching of the natural pressure pulsation frequency of the jet with the frequency of pressure oscillations produced in the organ pipe. As explained by Johnson et al. [82][83], there exists a critical frequency of pressure pulsations and a Strouhal number (*St*) associated with this frequency that leads to the organization of large-scale turbulent motion into cavitating vortex rings, and consequent cavitation intensification. This frequency is dependent on the length of the upstream organ pipe geometry. It has been shown that the organization of large-scale turbulent motion into cavitating vortex rings is most distinct for a *St* of 0.3 [84]. A detailed discussion of this phenomenon can be found in [81][83]. Even though their research is focused on submerged jets, it can be hypothesized that such an excitation of the inner jet flow can also increase cavitation intensity in co-flow cavitating jets. However, there is no study on the effect of upstream inner jet organ pipe nozzle geometry on cavitation intensification in co-flow cavitation peening.

From fuel injection and spray formation studies, it has been shown that nozzle taper affects cavitation inception in high pressure nozzles. The taper is defined by the slope angle or alternatively with the area reduction of the nozzle orifice measured at the entry and exit. Thus, a nozzle with a diverging, zero and converging taper have negative, zero and positive values of area reduction. Macian et al. [85] conducted computational fluid dynamics (CFD) analysis on the cavitation inception phenomenon in fuel injector nozzles at 9.5 MPa and 19.5 MPa with converging and zero taper. They found that a nozzle with zero taper is more susceptible to cavitation inception than the nozzle with converging taper. Payri et al. [86] have experimentally shown greater cavitation inception in nozzles with zero taper compared to converging taper nozzles at pressures ranging from 10-80 MPa. It is to be noted that, the coefficient of discharge (C_d), which is an indication of the energy loss in the internal flow through the nozzle, is greater in the converging taper nozzle. He et al. [87] have shown through CFD simulations the effect of nozzle orifice shape for nozzles with diverging, zero, and converging taper. They found that the diverging taper nozzle is more inclined to cavitate than the zero taper nozzle. There is little cavitation inception and growth in nozzles with converging taper. This is explained by the phenomenon of flow separation. It is shown that flow separation accompanied by a sharp drop in pressure occurs within the length of the orifice in nozzles with diverging and zero taper. The flow separation creates zones of low pressure, which result in cavitation inception and propagation. This flow separation is not observed in the case of converging taper nozzles. In co-flow water cavitation peening, the flow in the high-pressure inner jet nozzle is also subjected to pressures and velocities like studies mentioned earlier. It is, therefore, quite evident that there is internal cavitation activity that may affect the jet characteristics and cavitation generation both internal and external to the nozzle. In co-flow cavitation peening, cavitation generation can occur due to flow separation internal to the inner jet nozzle and the shearing action of the inner jet flow with the outer jet flow [64]. Thus, there are indications that nozzle taper does have an influence on cavitation inception, in internal flows of the high-speed inner jet nozzle and potentially overall cavitation intensity in the co-flow field in co-flow water cavitation peening.

One notable study of the effect of nozzle geometry in cavitation peening using a submerged jet was reported by Soyama [88]. However, the entrance to the orifice was cylindrical while the exit orifice was diverging. Since the entry was cylindrical, the coefficient of discharge (C_d) was nominally equal (~0.64-0.65) to each other for all studied nozzle configurations. Nozzles with zero and converging taper were not investigated. An optimum diverging nozzle shape that increased cavitation intensity was determined and tested on a range of materials.

There are some subtle differences in the purpose of the inner jet nozzles used for co-flow cavitation peening and hydroentangling nozzles [89]. The purpose of a hydroentangling nozzle is to impart as much kinetic energy as possible for production of non-woven fabrics, whereas the purpose of inner jet cavitation peening is to maximize cavitation generation in the co-flow flow field. However, a comprehensive study of the effect of taper in inner jet nozzles for co-flow cavitation peening is lacking.

The length of an orifice influences jet breakup and cavitation in fuel injection nozzles at pressures similar to that in co-flow cavitation peening. Several studies have shown the influence of a dimensionless geometric parameter L_o/d ratio, where L_o is the length of the orifice and d is the diameter of the orifice. A study by Shimizu et al. [90] on the effect of the parameter L_o/d on jet breakup concluded that there exists a critical L_o/d ratio where the jet breakup length is minimized. Tamaki et al. [91] showed the effect of hydraulic flip and flow reattachment on the internal cavitation behavior, turbulence, and velocity profiles. At sufficiently high pressures exceeding ~0.3-0.4 MPa, detachment of the inner jet from the inner jet orifice walls occurs and an air pocket is formed in the space between the detached inner jet and the wall, which is known as hydraulic flip. This results in a jet with a smooth surface, which leads to delayed jet breakup. As the L_o/d ratio increases, reattachment of the inner jet occurs along the length of the wall and promotes cavitation collapse within the nozzle. However, at very high L_o/d ratios, the flow transforms into a fully developed rectangular (plug flow or constant) velocity profile flow which again increases jet breakup length [92]. Thus, the two competing mechanisms of hydraulic flip and flow reattachment are known to influence cavitation behavior in high pressure fuel injection nozzles. Further elucidation of the effect of inner jet nozzle orifice length on cavitation generation in co-flow cavitation peening is required for a better understanding of co-flow cavitation peening nozzle design.

Lastly, the use of water-soluble polyethylene oxide, which is a drag reducing polymer to reduce cavitation induced damage in metal surfaces has been studied [93]. The observed reduction is attributed primarily to the reduced intensity of the reentrant jet generated by the collapse of a cavitation bubble [94]. However, there is some evidence in the literature that the addition of water-soluble polymers to cavitating liquids can also enhance surface damage under certain conditions [23-25]. Specifically, the addition of water-soluble polymers such as polyethylene oxide (PEO) and polyacrylamide has been shown to increase the cavitation intensity and the resulting cavitation damage in metals. Ashworth et al. [23] showed through mass loss experiments that enhanced cavitation intensity is observed with 1000 particles per million by weight (wppm) of high molecular weight polyacrylamide solution in water. In the same study, an investigation of the role of viscosity on cavitation intensity enhancement was also undertaken. It was found that increased viscosity alone cannot explain the observed increase in cavitation intensity. It was reasoned that increased viscosity reduces the growth rate of air cavities and thereby reduces the shockwave intensity. Shima et al. [24] also reported similar trends in cavitation intensity with 100-1000 wppm of commercial high molecular weight polyethylene oxide (DuPont™ PolyOx) in water. An interesting observation of their work is that exposing the solid metal surface to all tested polymer solutions for short durations exhibited higher cavitation intensities characterized by greater mass loss. However, at longer durations the cumulative mass loss for the 500 wppm and 1000 wppm PolyOx solutions was reduced. These results suggest that an increase in cavitation intensity may be possible depending on the polymer concentration and duration of sonication. An increase in localized cavitation erosion in the vicinity of areas with small radius of curvature such as a hole edge was also demonstrated by Nanjo et al. for a 1000 wppm of PolyOx based water solution [25]. However, Brujan et al. have reported contradictory findings for the effect of polyacrylamide in water [95]. In contrast to the results of Ashworth et al. [23] and Shima et al. [24], Brujan et al. reported a reduction in mass loss of pure aluminum over 80 minutes of exposure when using aqueous polymer solutions with polyacrylamide concentrations of 10, 25, 100, 250, and 1000 wppm. However, as observed in most of the earlier studies, the effect of the polymer additive on cavitation intensity is most distinct for a short duration only. The study by Brujan et al. [95] considers a longer duration response that includes the effects of polymer degradation, which is known to reduce cavitation intensity Thus, polymer degradation may explain the contradictory findings. Surface tension is also known to decrease with increasing concentration of PEO water soluble polymer with molecular weight of 8000 [96]. Cavitation erosion rates are also known to be negatively influenced with a decrease in surface tension of the fluids, indicating a possible link between the concentration of polymers and cavitation inception as well [97].

In summary, it is evident from prior work that the effects of upstream inner jet organ pipe nozzles, inner jet nozzle orifice taper and inner jet nozzle orifice length have not been investigated and can enhance cavitation intensity due to the inner jet phenomenon. Also, aqueous polymer solutions can potentially enhance cavitation intensity depending on the polymer type, its concentration, and the duration of sonication. However, prior studies were motivated by the desire to reduce cavitation damage through polymer addition and are limited in their quantification of the effect of water-soluble polymer additives on cavitation to mass loss measurements only. Based on the need for increased cavitation intensity in ultrasonic cavitation peening and the potential of polymer additives for enhancing cavitation intensity, a more detailed quantitative assessment of the effects of such polymer additives is needed.

2.5 Summary

Some key findings of the literature survey are as follows:

1. There is no work on the effect of upstream organ pipe geometry in co-flow cavitation peening for intensification of cavitation.
2. A comprehensive study of the effect of inner jet nozzle orifice taper in co-flow cavitation peening is lacking.
3. No work has been carried out on the effect of inner jet nozzle orifice length in co-flow water cavitation peening.
4. The effects of addition of polymer additives on ultrasonic cavitation peening have not been investigated.

In light of the above findings, this thesis focuses on addressing these limitations as described in the following chapters.

CHAPTER 3. ENHANCING CAVITATION INTENSITY IN CO-FLOW WATER CAVITATION PEENING WITH ORGAN PIPE NOZZLES

3.1 Overview

Co-flow water cavitating jets induce compressive residual stress through cavitation impacts produced by the collapse of the cavitation cloud. Co-flow water cavitation peening causes minimal surface alteration compared to conventional processes such as shot peening, which is a major advantage. However, enhancement of cavitation intensity for co-flow water cavitation peening nozzles is required for practical applications requiring greater process capability. Scaling of co-flow cavitation peening nozzles to achieve greater cavitation intensity requires higher flow rates, thus requiring pumps of higher capacities. In contrast, organ pipe geometry nozzles can enhance cavitation intensity without significant increase in pump capacity and have been used in deep sea drilling applications.

The objective of this work is to study the effects of organ pipe inner jet nozzle geometry on co-flow water cavitation intensity and peening performance relative to a standard (unexcited) inner jet nozzle geometry through experiments on aluminum alloy Al 7075-T651. Nozzle performance is characterized via extended mass loss and strip curvature tests, high-speed visualization of the cavitation cloud, analysis of impulse pressures, and through-thickness residual stress measurements.

3.2 Experimental method

3.2.1 Experimental setup

Co-flow water cavitation peening was carried out in an experimental facility utilizing the co-flow nozzle geometry and system design shown schematically in Fig. 3-1. The system is designed in such a way that the standoff distance, which is defined as the perpendicular distance between the nozzle and the workpiece, can be adjusted. The inner high-speed jet is driven by a plunger pump rated at 34 MPa and 2.8×10^{-4} m^3/s while the outer jet is driven by a centrifugal pump capable of delivering 3.8×10^{-3} m^3/s at a pressure of 392 kPa. The overall nozzle dimensions, given in Table 3-1, are selected based on prior literature [20,98]. Detailed information of system design and flow homogenization methods can be found in [99].

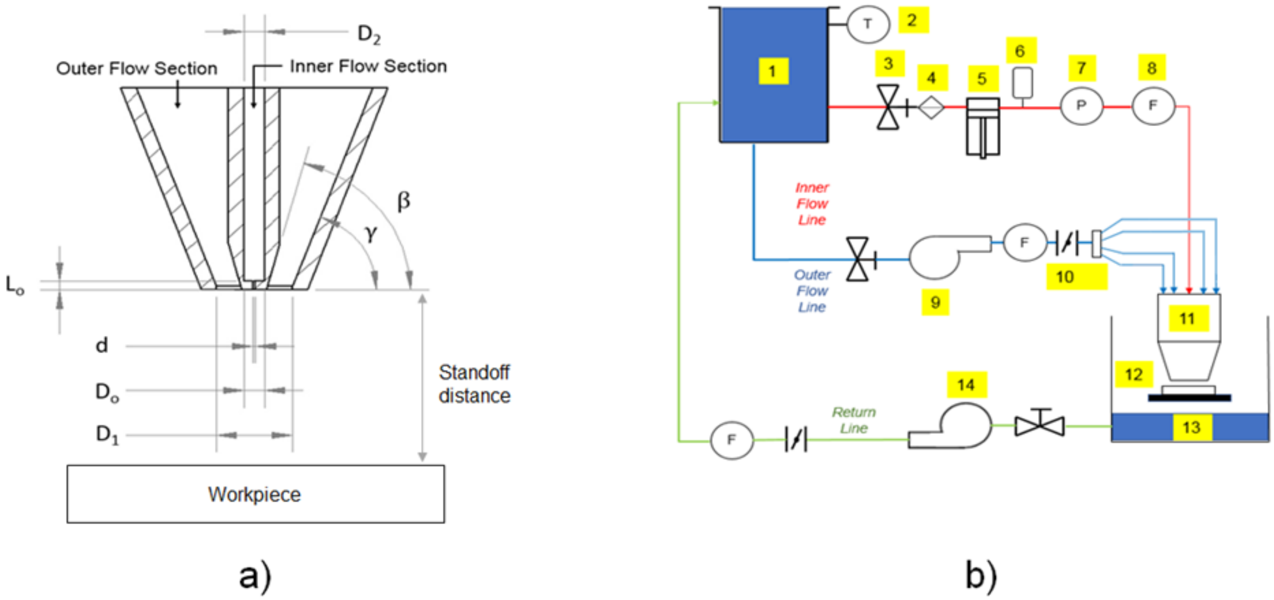

Fig. 3-1 a) Co-flow water cavitation peening nozzle geometry, b) system schematic indicating (1) reservoir tank (1), temperature indicator (2), valve (3), filter (4), high pressure plunger pump (5), pulsation dampener (6), pressure gauge (7), flow meter (8), centrifugal pump (9), butterfly valve (10), co-flow nozzle (11), test enclosure (12), test sample (13), and drain pump (14).

Table 3-1 Major dimensions of co-flow nozzle.

d	0.85 mm
D_o	12.8 mm
D_1	24 mm
D_2	8 x d
L_o	2 mm
β	75°
γ	70°

3.2.2 *Experiment design*

The unexcited inner jet nozzle geometry, which consists of a long straight bore of 6.4 mm diameter, is shown in Fig. 3-2a. The organ pipes shown in Fig. 3-2b are cylinder shaped chambers of varying length L with two area contractions defined by $\left(\frac{Ds}{D}\right)^2$ and $\left(\frac{D}{d}\right)^2$ at the entry and exit, respectively.

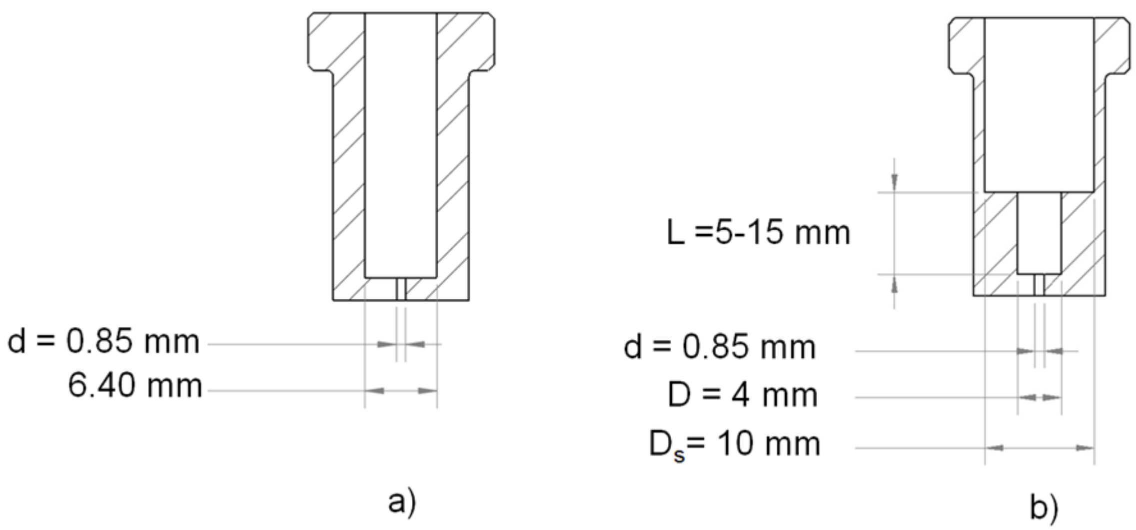

Fig. 3-2 Schematic of a) unexcited inner jet nozzle, b) organ pipe inner jet nozzle.

In contrast to the unexcited inner jet nozzle geometry, organ pipes work on the principle of passive excitation. In theory, the pressure oscillations occurring at the nozzle exit are intensified by reflection of these pressure fluctuations from the upstream organ pipe contractions, which is termed self-resonance. The first mode of resonance will occur if a standing wave of wavelength $4L$ is formed in the resonating organ pipe with large area contraction at both ends. Hence, the pulsating frequency of an organ pipe with large area contractions at both ends is given by,

$$f = \frac{c}{4L} \tag{1}$$

where, f is the pulsating frequency associated with the organ pipe, c is the speed of sound and L is the length of the organ pipe. The Strouhal number (*St*) is defined as,

$$St = \frac{fd}{V} \tag{2}$$

where, *d* is the inner jet orifice diameter, and *V* is the inner jet velocity. The velocity *V* is calculated as,

$$V = \frac{Q}{A_o} \tag{3}$$

where *Q* is the volumetric flow rate measured by an inline inner jet flow meter, as shown in Fig. 3-1, and A_o is the cross-sectional area of the inner jet nozzle orifice.

Combining Eqs. 1 and 2, we get the length of organ pipe as,

$$\frac{L}{d} = \frac{K_n}{(M)(St)} \tag{4}$$

where *M* is the Mach number of the inner jet, and K_n is the mode parameter given by Eqs. 5 and 6 [81]

$$K_n \simeq \frac{2n-1}{4} \text{ for } \left(\frac{Ds}{D}\right)^2 \text{ and } \left(\frac{D}{d}\right)^2 >> 1 \tag{5}$$

$$K_n \simeq \frac{n}{2} \text{ for } \left(\frac{Ds}{D}\right)^2 >>1 \text{ and } \left(\frac{D}{d}\right)^2 \simeq 1 \tag{6}$$

where *n* is the mode number. For the current nozzle design dimensions shown in Fig. 3-2, the mode parameter is 0.25.

Table 3-2 Strouhal numbers and corresponding organ pipe lengths investigated.

Strouhal Number (*St*)	Pulsating Frequency *f* (kHz)	Length *L* (mm)
0.14	25	15
0.28	50	7.5
0.42	75	5

3.2.3 Extended mass loss tests

Cavitation intensity can be evaluated by the mass loss produced by exposing the material to the cavitating flow past the incubation period [99, 100]. In order to evaluate the cavitation intensity as a function of the inner jet nozzle geometry, extended mass loss tests for 30 minutes each were conducted on Al 7075-T651 over a range of standoff distances. The nominal composition of the Aluminum 7075-T651 samples is given in Table 3-3.

Table 3-3 7075-T651 alloy composition by weight percentage.

Alloying element	Percentage by weight (wt.%)
Zinc	5.1-6.1%
Magnesium	2.1-2.9%
Copper	1.2-2.0%
Silicon	0.40%
Iron	0.50%
Manganese	0.30%
Titanium	0.20%
Chromium	0.18-0.28%
Aluminum	Remaining
Other:	0.05% (max)

The standoff distance was normalized by the diameter d of the inner jet orifice in accordance with prior work and is termed normalized standoff distance (*nSOD*) [99]. The water temperature was maintained at 303 ± 3 K for the duration of each test. The velocity of the inner flow was kept at 150 ± 3 m/s while the pressure was maintained at 26 ± 0.34 MPa. The outer jet velocity was maintained at 11 ± 0.2 m/s since it was observed from previous work that the optimum outer velocity is approximately constant [99]. The reported velocities were determined from continuity of fluid flow and inline flow meters. The co-flow cavitating jet was allowed to impinge on the sample to create a typical annular erosion pattern seen in Fig 3-3. Three repetitions were performed at each *nSOD* for each nozzle to ensure repeatability. Mass loss was measured using an analytical scale with 0.1 mg resolution and 0.3 mg repeatability.

Fig. 3-3 Erosion pattern created after 30 minutes by the co-flow water cavitating jet on Al 7075-T651.

3.2.4 Strip curvature tests

Strip curvature tests were performed using the optimum organ pipe geometry and the unexcited nozzle geometry at the optimum normalized standoff distance identified from the extended mass loss tests. The strip curvature measurements provide an indirect but rapid measure of peening performance. It is known that the compressive residual stress produced by peening a long strip of metal changes its curvature, which can be analyzed by classical beam theory [101]. Hence, a greater change in curvature translates to improved peening performance. Aluminum 7075-T651 strips of dimensions 19 mm x 76 mm x 6.35 mm were peened at a scan speed of 480 mm/min and a pitch of 1 mm, with the plan view of the strip shown in Fig. 3-4. Each strip was subjected to six full passes and the corresponding exposure times, which are dependent on the cavitating jet areas (A_c), were calculated using the procedure described in [99]. The cavitating jet area (A_c) is a function of the normalized standoff distance and nozzle design, if other operating conditions are kept constant. Even though the exposure times for each nozzle and standoff distance are different, the processing time (t_p) was the same at 18 min since the strips were subjected to an equal number of passes.

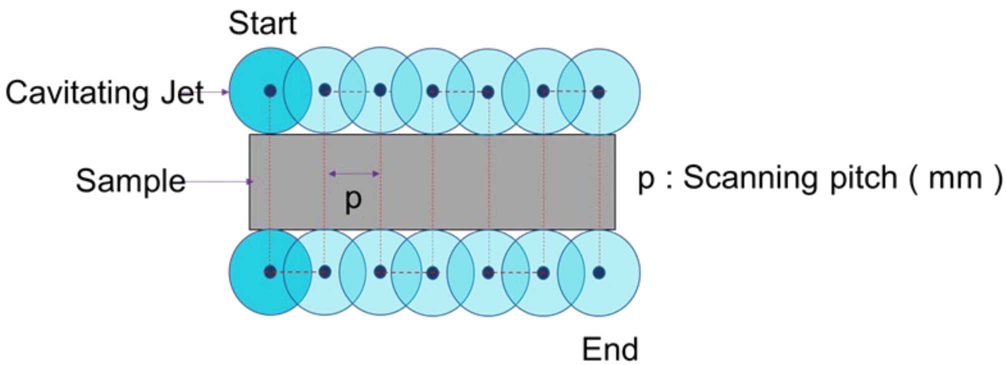

Fig. 3-4 Plan view of scanning pattern used in strip curvature tests.

In order to measure the change in strip curvature, the curvature before and after peening were evaluated using a scanning Coordinate Measuring Machine (Brown and Sharpe), as shown in Fig. 3-5.

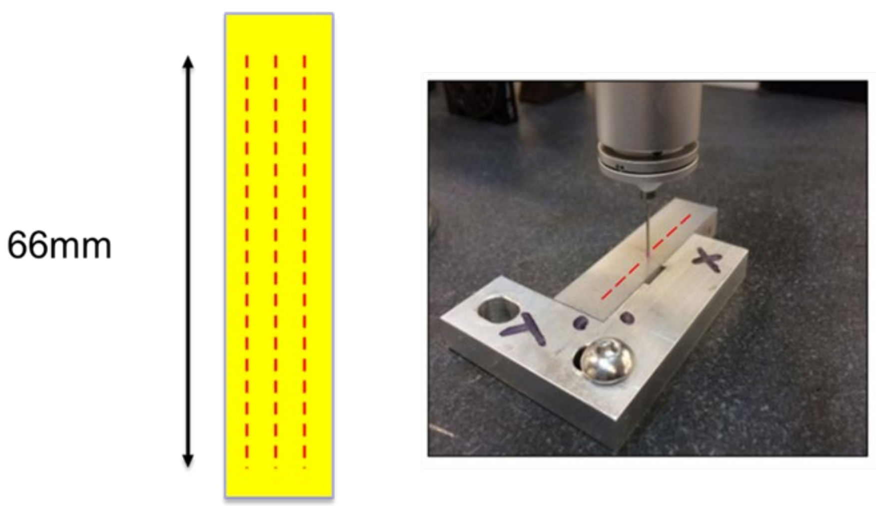

Fig. 3-5 Strip curvature evaluation using CMM.

3.2.5 *High-speed flow visualization*

High speed videography of the cavitating co-flows was conducted at 16,000 frame per second (fps) using a Phantom™ VEO 410L camera with a resolution of 640 x 480 and a Nikon 50 mm f1.8 lens. The setup was arranged as shown in schematically in Fig. 3-6. The experimental procedure used here is similar to that reported by Marcon et al. [99].

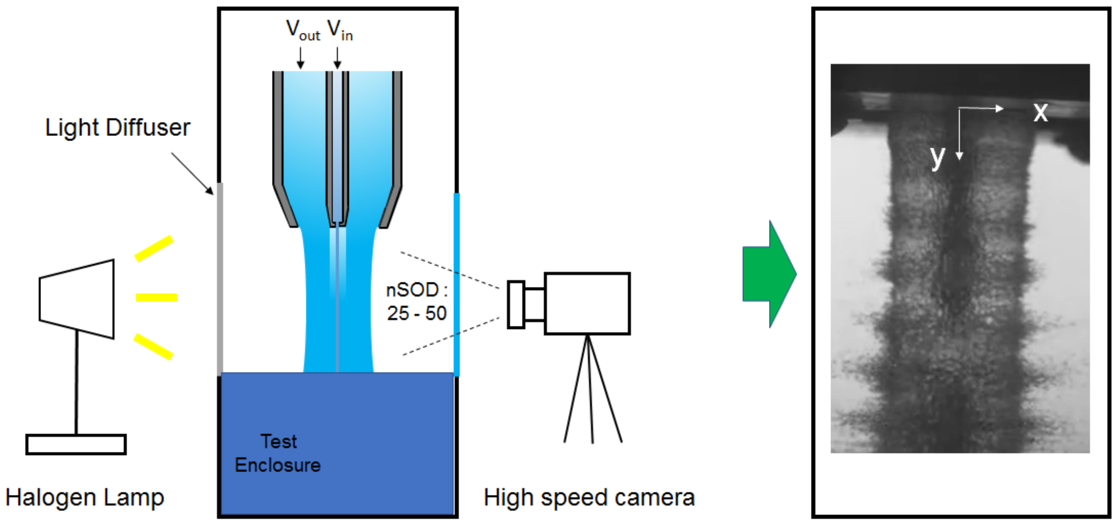

Fig. 3-6 Schematic of high-speed videography.

Since the cavitation cloud is thought to be an agglomeration of cavitation bubbles in the vapor phase, they are opaque to incident light and show up as dark colored areas in the field of view, whereas the surrounding outer jet is transparent and appears bright. A representative sample of 4000 frames corresponding to a duration of 0.25 s is obtained. A region of interest of 0.7*D* in width and 1.75*D* in length is cropped from each image. In order to extract parameters related to cloud behavior in the range of *nSOD* values of 25 to 50, an image processing algorithm similar to that described in [99] was applied. Specifically, the average maximum cloud widths at *nSOD* values ranging from 25 to 50 were obtained. Power spectral density (PSD) analysis of cloud width variation reveals the cloud shedding frequency, which is defined as the dominant frequency in the PSD plots. It should be noted that the cavitating jet was videographed without a solid wall or specimen in the path of the cavitating jet.

3.2.6 Impulse pressure measurements

Impulse pressure measurements were made using a dynamic pressure sensor (PCB™ W113B22) with a pressure range of 34 MPa, rise time of 1 µs, diaphragm diameter of 5.5 mm and a resonant frequency of 500kHz, which allowed for high frequency measurements. The data was sampled at 1 MHz using a PC based NI™ data acquisition system. In order to protect the diaphragm and associated piezoelectric elements from damage, the pressure transducer was installed as shown schematically in Fig. 3-7.

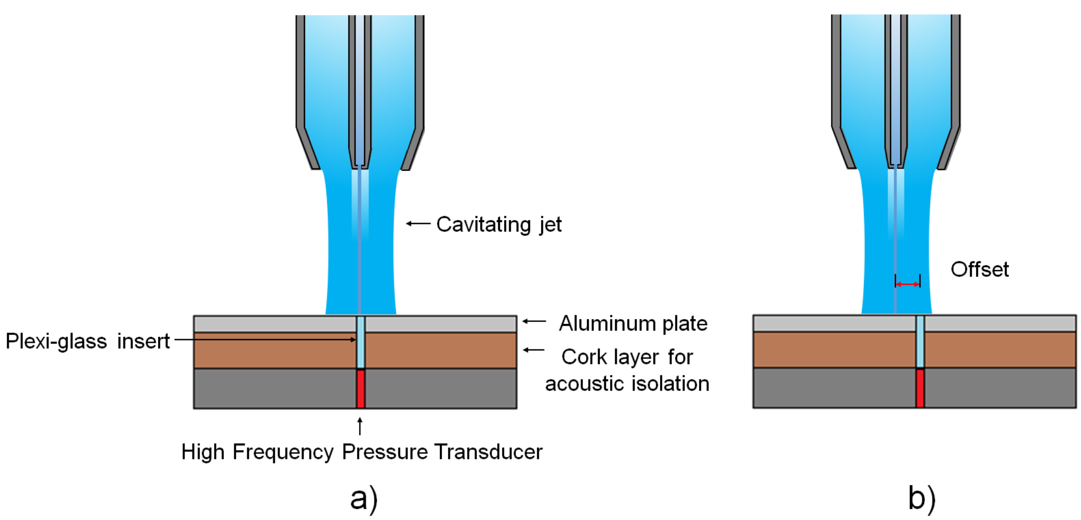

Fig. 3-7 Impulse pressure measurement at a) center of cavitating jet, b) with translation from cavitating jet.

As seen in Fig. 3-7a, a plexiglass insert protects the sensitive area of the pressure sensor diaphragm from the cavitating flow while providing an acoustic path to the sensor. In order to ensure acoustic isolation, the plexiglass insert was surrounded by a layer of cork. An aluminum plate, flush with the plexiglass insert, covered the cork layer to protect it from the cavitating jet. This setup alters the calibration constant of the pressure sensor, which needs to be accounted for during impulse pressure data acquisition. Recalibration of the pressure transducer to obtain the new calibration constant was performed by modal impact hammer testing, which was conducted by impacting the plexiglass insert, which is acoustically connected to the pressure sensitive region of the pressure transducer and recording the resulting response from the pressure transducer. The frequency response of the transducer obtained by applying Welch's method was essentially flat, translating to a constant multiplying factor of 7.858 MPa/V across all frequencies, which is considered the new calibration constant. The use of pressure fluctuations, measured with a high frequency pressure transducer produced due to an impinging jet, is a well-known technique for cavitation intensity measurement in both ultrasonic and hydrodynamic cavitation [66, 102].

Care was taken to initially align the cavitating jet with the center of the pressure diaphragm. In order to measure the impulse pressure fluctuations across the entire cavitating jet area A_c the cavitating jet was translated intermittently by 2 mm at a time to measure the impulsive pressure fluctuations as a function of the radial distance from the center, as shown in Fig. 3-7b.

3.2.7 Residual stress measurements

X-ray diffraction based residual stress measurements using Cr-Kα radiation and (311) lattice planes of Al-7075-T651 were made on samples processed by the unexcited and the optimum organ pipe inner jet nozzles using the two-angle $\sin^2 \psi$ technique in accordance with SAE HS 784 [103]. To facilitate through-thickness residual stress measurement, material was electrochemically removed to minimize alteration of the subsurface residual stress. To account for residual stress relaxation caused by electrochemical material removal and the influence of penetration of radiation employed, correction of the results was done according to the procedures outlined in [104]. The residual stress measurements were made at Lambda Technologies (Cincinnati, OH).

3.3 Results and discussion

The mass loss results for the inner jet organ pipe and the unexcited nozzle geometries as a function of the normalized standoff distance and the Strouhal number *(St)* are shown in Fig. 3-8.

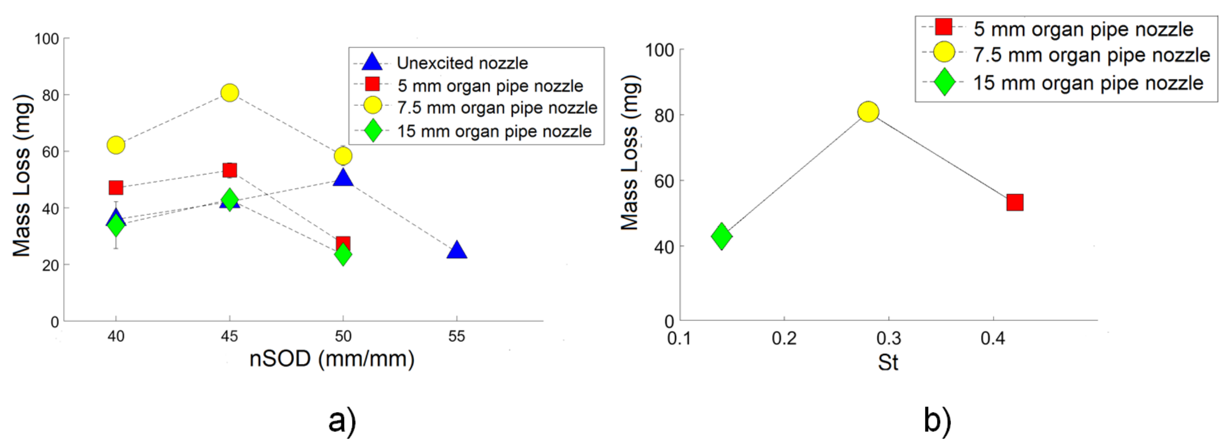

Fig. 3-8 Mass loss as a function of nSOD for organ pipe nozzle, b) maximum mass loss as a function of Strouhal number (*St*).

It can be seen from the Fig. 3-8 that the cavitating jet produced by the inner jet organ pipe nozzle with organ pipe length *L* of 7.5 mm (*St* = 0.28) generated a maximum mass loss of 80.63 mg at a *nSOD* of 45, whereas the unexcited inner jet nozzle generated a maximum mass loss of 50 mg at a *nSOD* of 50. This translates to an increase in mass loss of 61% over the unexcited inner jet nozzle. Interestingly, the optimum *nSOD* for all tested organ pipe nozzle geometries was 45, whereas it is 50 for the unexcited nozzle. The physical reason for this difference remains undetermined. The increased mass loss is confirmation of the increased cavitation intensity induced by self-resonance in the organ pipe. In contrast, the mass losses generated by the organ pipe inner jet nozzles with *St* of 0.42 and 0.14 are comparable to mass loss generated by the unexcited inner jet nozzle. Based on these results, the 7.5 mm organ pipe inner jet nozzle corresponding to *St* of 0.28 is identified as the optimum organ pipe inner jet nozzle geometry. Interestingly, the optimum Strouhal number identified here is close to the optimum value proposed by Crow and Champagne [84]. The error bars in the figure correspond to 95% confidence intervals.

To further evaluate the effect of increased cavitation intensity on peening performance, strip curvature tests were carried out on the peened Al 7075-T651 samples. The exposure times for the cavitating jet produced by the unexcited and optimum organ pipe inner jet nozzles were 348.9 s and 288.3 s, respectively. The difference in exposure times is due to differences in cavitating jet areas A_c produced by the two nozzles.

The changes in strip curvatures produced by the optimum inner jet organ pipe and the unexcited inner jet nozzles are shown in Fig. 3-9. Due to increased cavitation intensity, the change in strip curvature for the optimum organ pipe inner jet nozzle is 66% higher than for the unexcited inner jet nozzle. The error bars at the peaks of the profiles in Fig. 3-9 correspond to 95% confidence intervals.

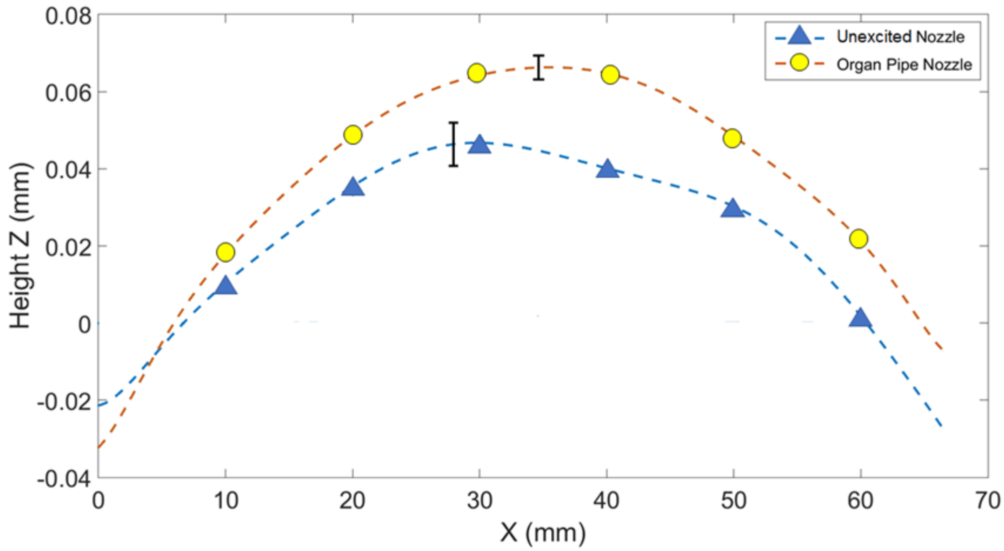

Fig. 3-9 Net strip curvature results for the two nozzles.

High-speed video analyses of the cavitating flows produced by the optimum organ pipe nozzle and the unexcited nozzle were carried out to obtain evidence of cavitation intensification using the organ pipe nozzle geometry. A sequence of eight images sampled at 8 kHz, corresponding to a time duration of 0.001 s is shown for the unexcited and the optimum organ pipe inner jet nozzles in Fig. 3-10a and 3-10b, respectively. The images reveal the periodic formation and shedding of the cavitation cloud in co-flow cavitation peening. The disruption of the outer flow as the flow exits the nozzle is also visible. It is conjectured that this disruption is due to acceleration of the outer flow by the inner flow, which reduces the overall cross-sectional area of the cavitating jet and leads to eventual jet breakup. The video images were analyzed using image processing techniques described in [64] to compute the average maximum cloud width variation produced by the two nozzles. The cloud width data was used to compute the corresponding power spectral densities (PSD).

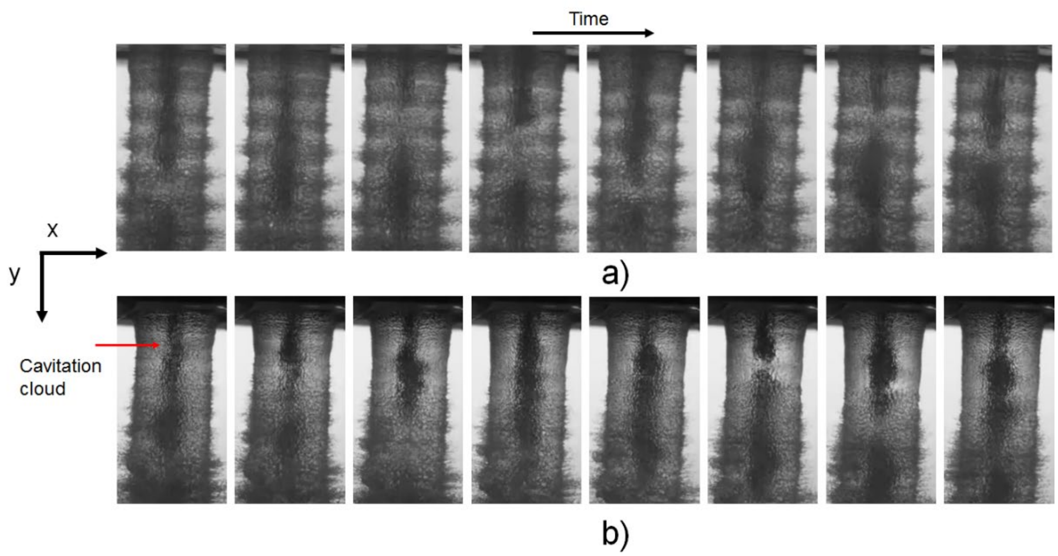

Fig. 3-10 Sequence of high-speed images corresponding to a time duration of 0.001 s of the co-flow cavitating jets produced by the a) unexcited inner jet nozzle, b) optimum organ pipe inner jet nozzle.

The power spectral densities of the average maximum cloud width variation produced by the unexcited and optimum organ pipe nozzles at *nSOD* values of 50 and 45, respectively, are shown in Fig. 3-11. Note that the mass loss at these *nSOD* values is greatest for the respective nozzles.

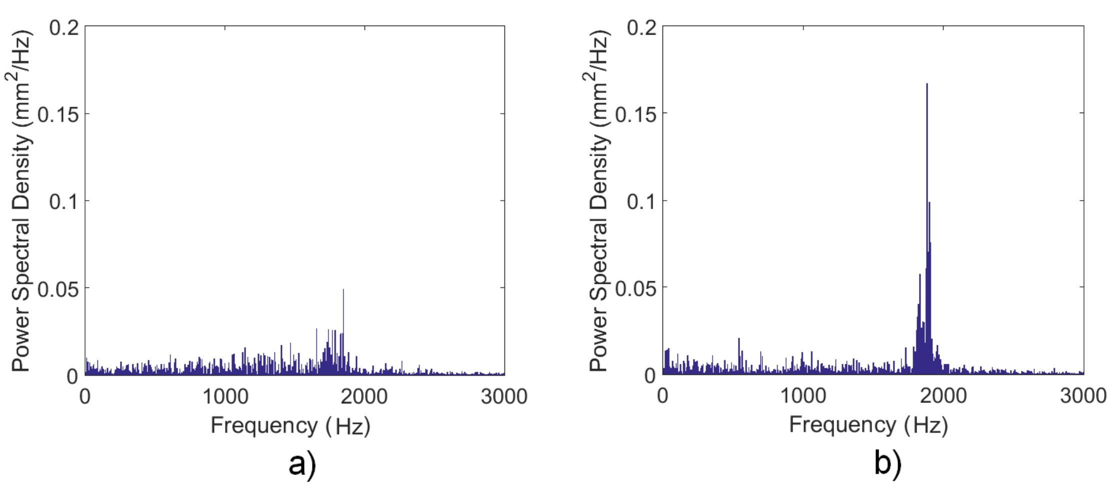

Fig. 3-11 PSD of average maximum cloud width variation for a) unexcited inner jet nozzle at *nSOD* 50 and b) optimum organ pipe nozzle at *nSOD* 45.

The dominant frequencies of the two PSD spectra correspond to the respective cavitation cloud shedding frequencies. The cloud shedding frequency of the unexcited inner jet nozzle at *nSOD* of 50 is 1656 Hz while it is 1884 Hz at *nSOD* of 45 for the optimum organ pipe nozzle. Thus, the shedding frequency of the optimum organ pipe inner jet nozzle is greater than the shedding frequency of the unexcited inner jet nozzle. In addition, it can be clearly seen that the power at the cloud shedding frequency for the optimum organ pipe nozzle is greater than the power at the corresponding frequency for the unexcited nozzle. These results can be attributed to the greater structure and intensity in the cavitation cloud emanating from the optimum organ pipe nozzle. The shedding frequencies found in this study are in good agreement with values in the range of ~ 2kHz previously reported in the literature [99, 105]. In order to characterize the total power associated with cloud width variation, ten sets of 400 images each were created from the original 4000 images available for both nozzle designs and their PSDs were computed. The total power, defined by the area under the PSD curves, for each of these ten sets of images for the two nozzle geometries was averaged and are presented in Fig. 3-12. The error bars in the figure correspond to 95% confidence intervals.

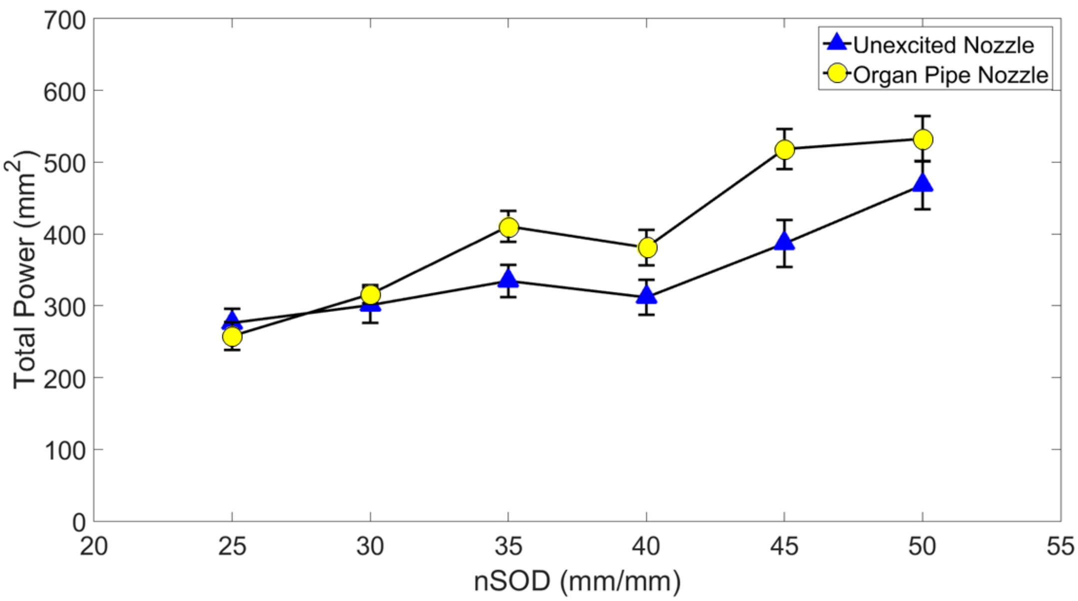

Fig. 3-12 Total power of average maximum cloud width variation over a range of *nSOD* for a) unexcited inner jet nozzle, b) optimum organ pipe inner jet nozzle.

The power of the PSD, which is an indication of the overall strength of the cavitation cloud, shows a monotonically increasing trend with increasing *nSOD*. It can be seen that the power of the optimum organ pipe inner jet nozzle geometry is consistently higher than the corresponding power of the flow generated by the unexcited inner jet nozzle geometry, with the exception of *nSOD* of 25. This is attributed to the cloud formation being in a nascent stage at such low stand-off distances.

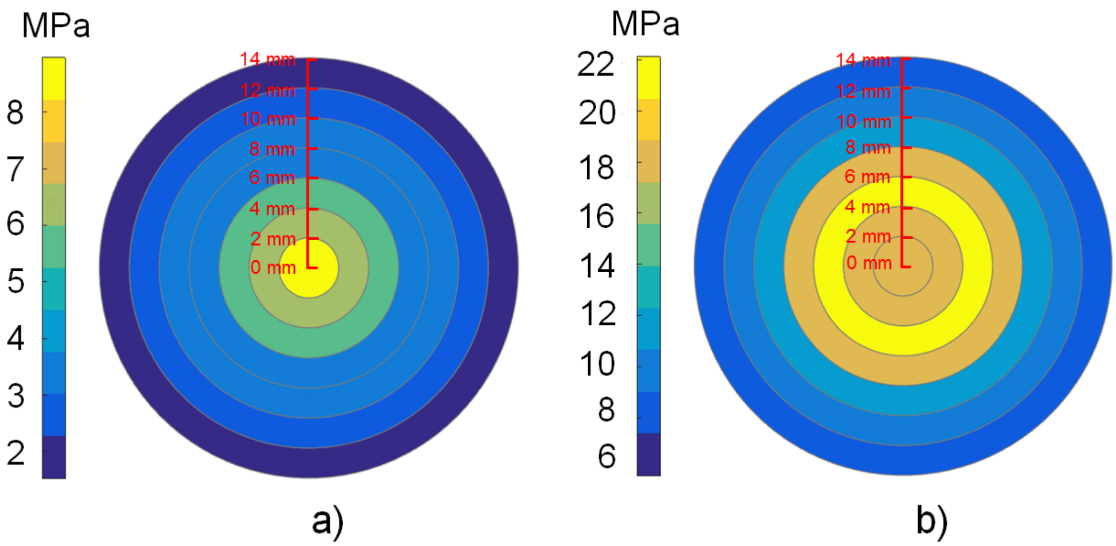

Fig. 3-13 Radial distribution of maximum pressure fluctuation of a) unexcited inner jet nozzle at *nSOD* of 50, b) optimum organ pipe inner jet nozzle at *nSOD* of 45.

Contours of the maximum impulse pressure fluctuations observed in the unexcited and the optimum organ pipe inner jet nozzles as a function of the radial distance from the center of the cavitation area at their respective optimum *nSOD* values of 50 and 45 are shown in Fig. 3-13. It can be seen in Fig. 3-13 that the maximum pressure fluctuations produced by the optimum organ pipe inner jet nozzle are greater than the maximum pressure fluctuations produced by the unexcited inner jet nozzle. The plots show that the maximum pressure fluctuations occur 2 mm away from the center for the unexcited inner jet nozzle and 6 mm away from center for the optimum organ pipe inner jet nozzle. This is consistent with the erosion patterns observed in the mass loss tests where the most aggressive erosion takes places in the outer ring region of the cavitation area.

In order to gain insight into the frequency distribution of the cavitation events occurring at the optimum *nSOD*, approximately equal number of cavitation events were extracted from the impulse pressure measurements at the center of the cavitating jets for both nozzles. In this context, it is assumed that peaks with a minimum threshold of 0 MPa in the time history of the impulse pressure correspond to individual cavitation events.

The pressure amplitudes were binned to obtain a frequency distribution of cavitation events, as shown in Fig. 3-14. The overall distribution of cavitation events for the unexcited nozzle is seen in Fig. 3-14a. The corresponding number of events with amplitudes above 2 MPa and 7 MPa are seen in Fig. 3-14b and 3-14c, respectively.

Similarly, the overall distribution of cavitation events for the optimum organ pipe nozzle is seen in Fig. 3-14d. The number of events with amplitudes above 2 MPa and 7 MPa for the organ pipe nozzle are seen in Fig 3-14e and 3-14f, respectively.

The frequency of high intensity cavitation events (defined as cavitation events with pressure amplitudes greater than 7 MPa) was 4 Hz for the unexcited nozzle and 74 Hz for the optimum organ pipe nozzle. Thus, the frequency of strong cavitation events in the cavitating jet produced by the organ pipe nozzle can explain the increased mass loss and the increased peening intensity observed.

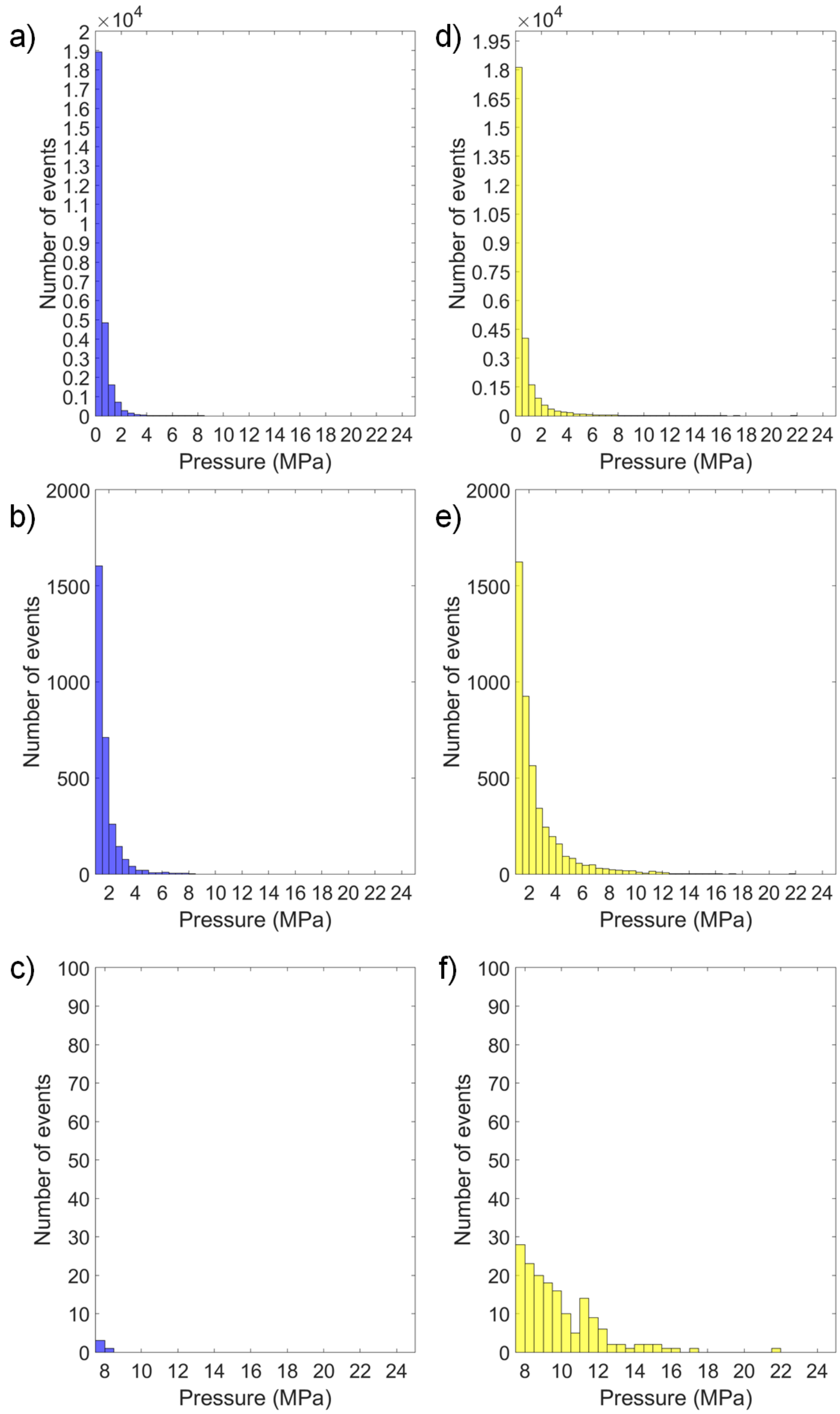

Fig. 3-14 Distribution of cavitation events binned by pressure amplitude for the a) unexcited nozzle, b) unexcited nozzle with amplitudes greater than 2 MPa, c) unexcited nozzle with amplitudes greater than 7 MPa, d) optimum organ pipe nozzle, e) optimum organ pipe nozzle with amplitudes greater than 2 MPa, and f) optimum organ pipe nozzle with amplitudes greater than 7 MPa.

It is known that organ pipe nozzles produce more intense pressure fluctuations at exit due to matching of the natural frequency of pressure fluctuations of the exiting jet with the frequency of pressure fluctuations in the upstream organ pipe section of the nozzle. This excitation leads to organization of the incoherent cavitation structures between the co-flows into large scale coherent vortical cavitation structures [82]. The pulsations, characterized by the Strouhal number (St), are imparted by the organ pipe nozzle to the exiting jet and in turn to the greater pressure fluctuation observed at the workpiece surface, seen in Fig. 3-13. It is noted by Deng et al. [102] that a higher-pressure fluctuation amplitude is an indication of resonance in the upstream organ pipe nozzle. In addition, enhanced coherence of the cavitation cloud at the shedding frequency, which is characterized by the greater intensity seen in Fig. 3-11 and Fig. 3-12, are further evidence of the improved performance of the organ pipe nozzles with respect to the unexcited nozzle. Since the organ pipe nozzles were designed to achieve the first mode of resonance, the nominal Strouhal number for formation of coherent vortical structures of the flow is 0.3, as determined by Crow and Champagne in their air jet experiments [84]. The reader is referred to the work of Crow and Champagne for a detailed explanation of the mechanisms underlying the formation of coherent vortical structures in air jets. However, the present work provides qualitative evidence of the resonance and structuring mechanism as well as quantitative evidence in the form of mass loss, strip curvatures, high speed videography, and impulse pressure measurements.

The value of 0.28 for the Strouhal number St, which depends on the length of the resonating chamber of the organ pipe nozzle, is therefore an indication of optimum nozzle geometry. The Strouhal number for the unexcited nozzle, calculated using the formula for large area reductions at both ends of the nozzle seen in Fig. 3-2a, is found to be 0.09. Flow excitation through pulsations corresponding to such a low Strouhal number is not expected to enhance the cavitation intensity since it is far from the experimentally determined optimum value of 0.28. Hence, the unexcited inner jet nozzle is distinct from the organ pipe inner jet nozzle.

It should be noted that the Strouhal number is a dimensionless number specific to oscillating flows such as those produced by organ pipe nozzles. While a universal dimensionless parameter that describes the effect of all nozzle geometry variables (not just the organ pipe length) is desirable, such a dimensionless parameter, however, is difficult to devise as it needs to account for a multitude of complex geometries and physical phenomena. Consequently, the present paper is limited to the Strouhal number to characterize the influence of organ pipe nozzle geometry (length of organ pipe section of the inner nozzle) on the frequency of pulsations that serve to amplify cavitation intensity.

Lastly, residual stress profiles of strips peened using the unexcited inner jet nozzle and the optimum organ pipe inner jet nozzle were evaluated by X-ray diffraction (XRD) and are shown in Fig. 3-15. The residual stress profiles for the two nozzles overlap up to a depth of approximately 50 μm. However, beyond this depth, the compressive residual stress produced by the optimum organ pipe inner jet nozzle is higher. It is important to note that increased cavitation intensity can cause some erosion of the treated surface, which can cause relaxation of the residual stress near the surface, as pointed out by Soyama and Saka [106]. Also shown for comparison are the residual stress profiles generated in Al 7075-T651 by laser shock peening (LSP) with power intensity of 2 GW/cm^2 [11] and the residual stress profiles obtained by shot peening (SP) [107]. The maximum compressive residual stresses generated by LSP and SP are less than the maximum compressive residual stress produced by the optimum organ pipe nozzle, which shows the enhanced capability of the co-flow water cavitation peening process.

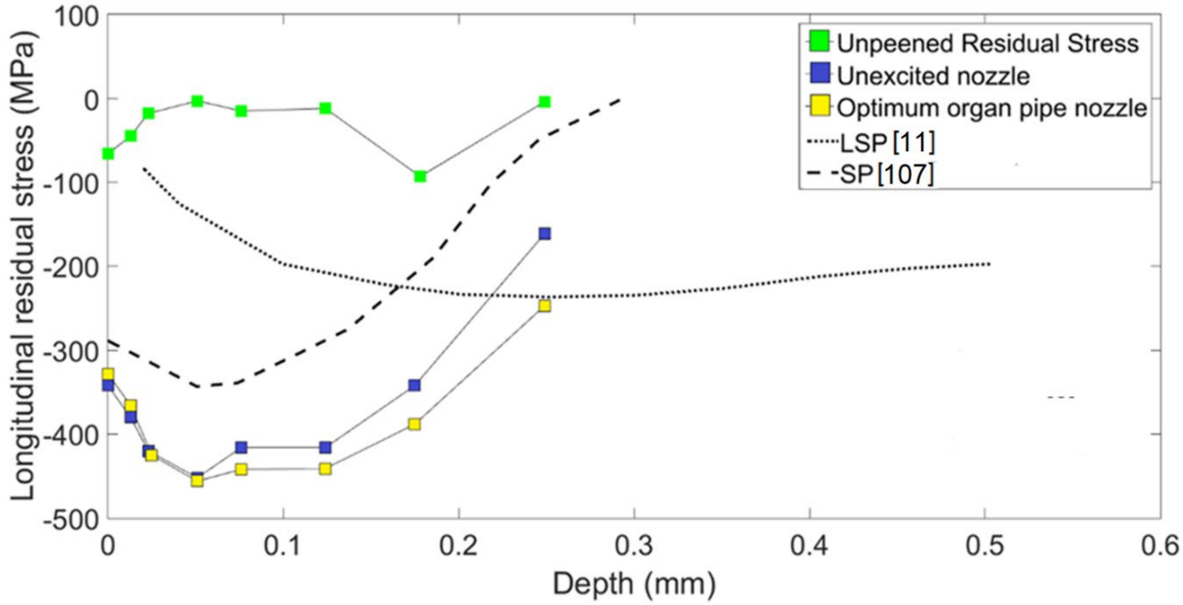

Fig. 3-15 Residual stress distribution as function of depth below surface. Data for LSP [11] and SP [107] are taken from literature and presented for comparison only.

3.4 Summary

The chapter presented an experimental investigation of the possible enhancement of cavitation intensity in co-flow water cavitation peening of aluminum 7075-T651 alloy by utilizing an organ pipe inner nozzle. Organ pipes of different lengths corresponding to different Strouhal Numbers (*St*) were designed and used in extended mass loss and peening experiments, and the results were compared with those obtained for a standard unexcited nozzle. The main conclusions of the chapter are as follows:

1. The optimum Strouhal Number for the inner jet, which leads to enhancement of cavitation intensity in co-flow cavitation peening, was found to be 0.28, a number that is close to the optimum value proposed by Crow and Champagne [84] for highly turbulent air jets.

2. The optimum organ pipe inner nozzle yielded a 61% increase in the mass loss and a 66% increase in strip curvature relative to the unexcited nozzle, indicating enhancement in cavitation intensity.

3. High speed videography and impulse pressure measurements provided valuable insights into the cavitation cloud characteristics for the unexcited and optimum organ pipe nozzles. Power spectral density analyses of the processed image data showed that the power associated with the optimum organ pipe nozzle is greater than the power associated with the unexcited nozzle. Analysis of impulse pressure measurements produced by cloud collapse events revealed that the enhanced intensity of the cavitating jets produced by the optimum organ pipe inner nozzle is due to the higher frequency of strong cavitation events.

4. Compressive residual stress generated by the optimum organ pipe nozzle is larger in magnitude at depths higher than 0.05 mm compared to the residual stress induced by the unexcited nozzle.

CHAPTER 4. EFFECT OF NOZZLE ORIFICE TAPER ON CAVITATION INTENSITY IN CO-FLOW WATER CAVITATION PEENING

4.1 Overview

Co-flow cavitation peening is a surface treatment process used to generate beneficial compressive residual stresses in a metallic surface through shock waves produced during the collapse of a cavitation cloud. The major advantage of co-flow water cavitation peening for aluminum alloys is the minimal surface roughening due to the small size of cavitation bubbles (~100 μm) and also estimated from the size of cavitation impact pits seen in aluminum alloys [17, 108]. To utilize co-flow water cavitation peening, optimal design of the nozzle is critical. The taper is defined by the slope angle or alternatively with the area reduction of the inner jet nozzle orifice measured at the entry and exit of the inner jet flow. Optimization of nozzle geometry in co-flow cavitation peening, and cavitation peening in general, requires that the effect of inner jet nozzle orifice taper be understood. In this study, the effect of the inner jet nozzle orifice taper in co-flow cavitation peening is investigated. Specifically, the effects of nozzle orifice geometries with diverging, zero, and converging taper are evaluated through extended mass loss, impulse pressure, and strip curvature measurements. Further, computational fluid dynamics simulations are utilized to understand the inner jet nozzle flow to explain the experimental results.

4.2 Experimental method

4.2.1 Experiment design

Three inner jet nozzle variants with varying degrees of nozzle orifice tapers were designed and fabricated to study the effect of taper on cavitation intensity. The taper is defined by the slope angle or alternatively with the area reduction of the inner jet nozzle orifice measured at the entry and exit of the inner jet flow. The designed inner jet nozzles with diverging, zero, and converging tapers are shown in Fig. 4-1. The nozzles with diverging, zero, and converging taper have negative, zero and positive nominal values of area reduction, respectively which translates to nominal internal half-taper or slope angles of -0.88°, 0° and 0.88° respectively. The entry and exit dimensions of each nozzle replication are listed in Table 4-1. Nozzle orifices were fabricated using an Accutex™ Wire Electrical Discharge Machine (WEDM). To ensure repeatability and to account for manufacturing variation, three replications of each nozzle variant were fabricated and tested.

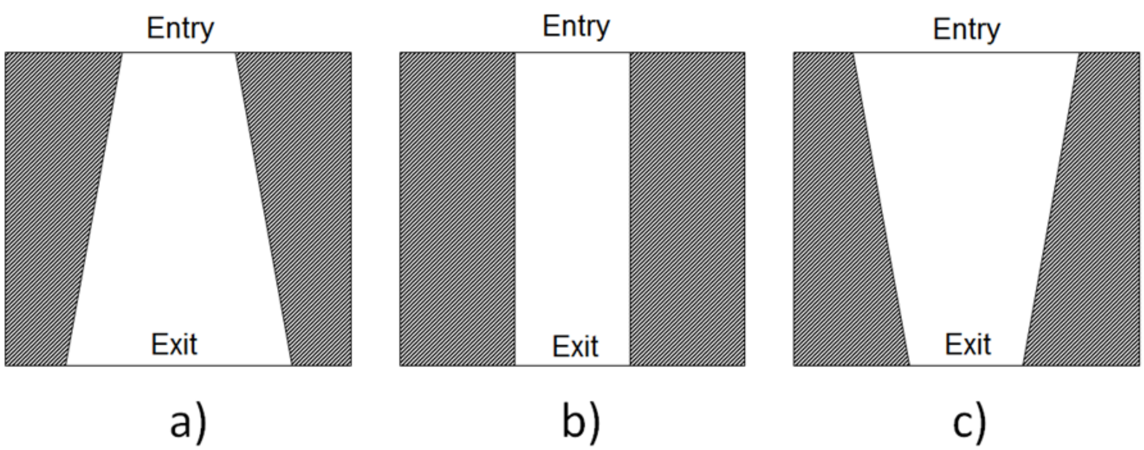

Fig. 4-1 Schematics of the inner jet nozzle taper designs a) diverging taper, b) zero taper, c) converging taper.

Table 4-1 Actual dimensions of fabricated nozzles with varying tapers.

	Entry diameter D_1 (μm)	Exit diameter D_2 (μm)	Area reduction $\left(\frac{D_1^2-D_2^2}{D_1^2}\right)x100$ %
Diverging taper 1	853	911	-14.06 %
Diverging taper-2	856	912	-13.51 %
Diverging taper-3	859	915	-13.46 %
Zero taper-1	854	842	2.79 %
Zero taper-2	860	851	2.08 %
Zero taper-3	856	855	0.23 %
Converging taper-1	915	843	15.11 %
Converging taper-2	917	843	15.48 %
Converging taper-3	912	846	13.94 %

4.2.2 Extended mass loss tests

Extended mass loss tests at various standoff distances were carried out by allowing the co-flow cavitating jet to impinge on an Al 7075-T651 specimen for a duration of 30 min. Mass loss is an indication of the cavitation intensity and is part of standard ASTM test procedure in addition to being favored by leading researchers of cavitation peening [19,100].The mass loss of the specimen due to erosion caused by exposure to the cavitating jet was measured in an analytical scale with 0.1 mg resolution and 0.3 mg repeatability. Three repetitions were performed at each standoff distance. The standoff distance is normalized by the nominal minimum inner jet nozzle diameter and is termed the normalized standoff distance (*nSOD*). The nominal composition of the Aluminum 7075-T651 samples is given in Table 4-2.

Table 4-2 7075-T651 alloy composition by weight percentage.

Alloying element	Percentage by weight (wt.%)
Zinc	5.1-6.1%
Magnesium	2.1-2.9%
Copper	1.2-2.0%
Silicon	0.40%
Iron	0.50%
Manganese	0.30%
Titanium	0.20%
Chromium	0.18-0.28%
Aluminum	Remaining
Other:	0.05% (max)

Water temperature, which is known to be an important factor in cavitation, was kept in the range of 303 ± 3 K [109]. Pressure of the inner jet during testing was maintained at 26 ± 0.5 MPa. An outer jet velocity of 11 m/s, which corresponds to the optimum velocity determined in [99], was maintained during all tests. The coefficient of discharge (C_d) was calculated using the measured flow rates and the theoretical flow rates, which can be calculated using Bernoulli's formula given in Eq. (1) [81],

$$C_d = \frac{Q}{A_o}\sqrt{\frac{\rho}{2P}} \tag{1}$$

where Q, A_o, ρ and P are the actual volume flow rate, orifice cross sectional area, density, and gage pressure of water, respectively. The cross-sectional area is taken to be the smaller of the entry and exit cross-sectional areas, as it is the area that causes the most energy loss

4.2.3 Strip curvature tests

While mass loss is indicative of the increase in cavitation intensity due to nozzle design changes, it does not convey a measure of the residual stresses. It is known from classical beam theory that introduction of compressive residual stresses in a long thin strip of a plastically deformed material changes the curvature of the strip [101]. Hence, exposure to a co-flow cavitating water jet of greater intensity results in a larger increase in arc height of the peened metal strips. Aluminum 7075-T651 strips of dimensions of 76 mm x 19 mm x 6.35 mm were raster scanned by the cavitating jet with a pitch of 1 mm and a scan speed of 480 mm/min. The strips were subjected to six peening passes with a processing time (t_p) of 18 minutes for each strip. Plan view of the scanning pattern used on the strips is shown in Fig. 4-2. Measurement of strip arc profile before and after peening was done using a scanning Coordinate Measuring Machine (CMM) with a probe tip size of 1.5 mm. Peening was carried out using the optimum operating conditions identified from the extended mass loss experiments. Since the residual stress of an Aluminum 7075-T651 sample can be assumed to be near zero, any change in arc height is reflective of introduction of compressive residual stresses and is a technique widely used by researchers in peening and peen forming research [110] [111].

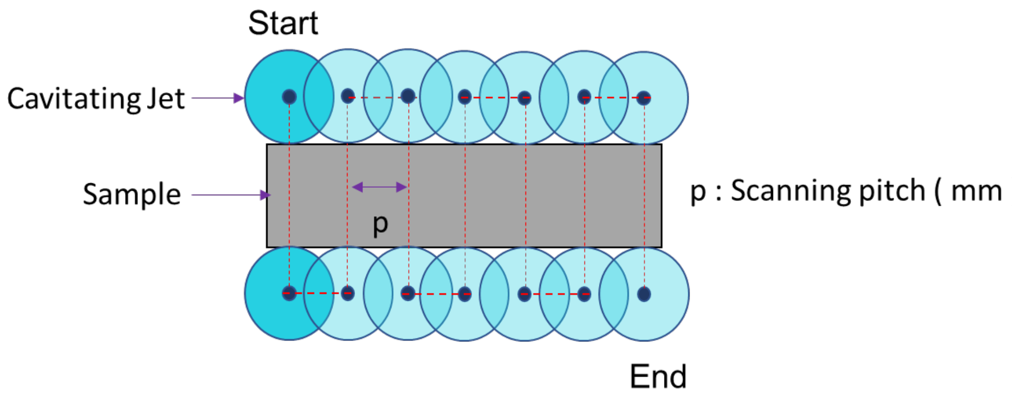

Fig. 4-2 Plan view of scanning pattern used on the aluminum 7075-T651 strip.

4.2.4 Impulse pressure measurements

To obtain a measure of impulse pressure and frequency of cavitation cloud collapse events, a high frequency pressure transducer (PCB™ W113B22) protected by a plexiglass covering was used. The plexiglass covering was mounted flush with the surface of the pressure transducer assembly, described earlier, and aligned with the co-flow cavitating jet as seen in Fig. 4-3. Since the area of the pressure sensitive transducer is small compared to the size of the cavitation cloud, the pressure transducer was translated 6 mm sequentially to obtain a radial distribution of impulse pressures about the nozzle axis, as seen in Fig 4-3b. The detailed methodology and rationale for such measurements can be found in [66,102,112].

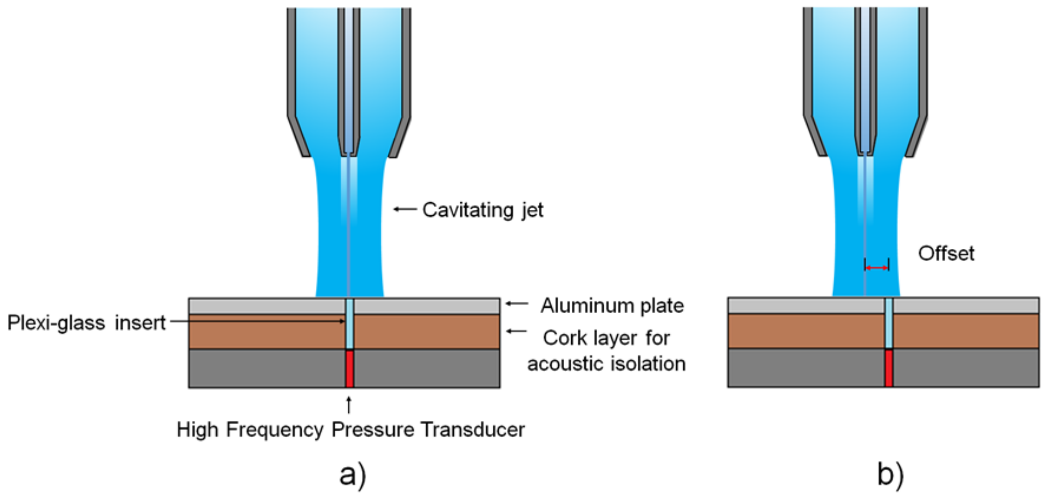

Fig. 4-3 Schematic of impulse pressure measurement using high frequency pressure transducer at a) center of cavitation erosion pattern, and b) as a function of radial distance.

4.3 Numerical methods

Computational fluid dynamics models for the fluid flow inside the inner jet nozzle were performed using steady state single phase Reynolds Averaged Navier Stokes (RANS) models in ANSYS™ Fluent. It is thought that the single phase model can resolve the velocity in the inner jet nozzles and may enable a qualitative interpretation of the behavior of the different nozzles. This was partly due to computational resources and time constraints. The relevant continuity and momentum equations for the axisymmetric condition are as follows [113]:

$$\frac{\partial \rho}{\partial t} + \frac{\partial \rho u_x}{\partial x} + \frac{\partial \rho u_r}{\partial r} + \frac{\rho u_r}{r} = 0 \tag{2}$$

where x and r are the axial and radial co-ordinates, ρ is the density of the fluid and u_x, u_r are the velocity components in the axial and the radial direction, respectively.

The axial momentum equation is given by

$$\frac{\partial \rho u_x}{\partial t}+\frac{1}{r}\frac{\partial (r\rho u_x u_x)}{\partial x}+\frac{1}{r}\frac{\partial (r\rho u_r u_x)}{\partial r} \tag{3}$$

$$=-\frac{\partial p}{\partial x}+\frac{1}{r}\frac{\partial [r\mu(2(\frac{\partial u_x}{\partial x}-\frac{2}{3}(\nabla.\boldsymbol{u}))]}{\partial x}+\frac{1}{r}\frac{\partial\left[r\mu\left(\frac{\partial u_x}{\partial r}+\frac{\partial u_r}{\partial x}\right)\right]}{\partial r}+F_x$$

The radial momentum equation is given by

$$\frac{\partial \rho u_r}{\partial t}+\frac{1}{r}\frac{\partial (r\rho u_x u_r)}{\partial x}+\frac{1}{r}\frac{\partial (r\rho u_r u_r)}{\partial r} \tag{4}$$

$$=-\frac{\partial p}{\partial r}+\frac{1}{r}\frac{\partial [r\mu(2(\frac{\partial u_r}{\partial r}-\frac{2}{3}(\nabla.\boldsymbol{u}))]}{\partial r}+\frac{1}{r}\frac{\partial\left[r\mu\left(\frac{\partial u_r}{\partial x}+\frac{\partial u_x}{\partial r}\right)\right]}{\partial x}-2\mu\frac{u_r}{r^2}$$

$$+\frac{2}{3}\frac{\mu}{r}(\nabla.\boldsymbol{u})+\frac{\rho v_z^2}{r}+F_r$$

where, $\boldsymbol{u}$ is the velocity vector in axisymmetric co-ordinates, p is the static pressure, μ is the molecular viscosity, F_x and F_r are the body force components in the axial and radial direction and u_z is the azimuthal velocity (what the ANSYS Theory Guide [113] refers to as the swirl velocity for axisymmetric simulations). It is to be noted here that the swirl velocity component u_z is zero in the axisymmetric simulations without swirl (similar to the present case) in ANSYS™ Fluent and which leads to underestimation of the Turbulent Kinetic Energy (TKE). It is to be noted that ANSYS defines the co-ordinates differently from a conventional cylindrical co-ordinate system.

Axisymmetric single phase models in the form of the RNG $k-\epsilon$ turbulence model with enhanced wall functions was used to model the internal flow distribution in the inner jet nozzles with different tapers [114,115]. The RNG $k-\epsilon$ turbulence model with enhanced wall functions was chosen for its ability to efficiently model near wall flow with a coarse mesh in the inner jet nozzle internal flow, even though significant mesh refinement was performed near the wall and the corner radius at the nozzle inlet [115]. Details of the mesh can be found in Appendix A2. Mesh convergence was achieved with progressive mesh refinement till differences in the area averaged velocity magnitude values at the inner jet nozzle exit were less than 0.5 % for the steady state simulations. A $k - \omega$ model in contrast requires sophisticated fine meshing approaching y^+ values of 1. Detailed explanation of y^+ and enhanced wall treatment can be found in [115]. Default values for turbulence intensity and turbulent viscosity ratio were used and can be found in Appendix A2. It is expected that the mesh quality can be improved significantly to account for all the turbulent kinetic energy near the wall. However, despite its shortcomings and due to the use of wall functions, a model with maximum y^+ values of 28 near the wall (as in the present case) may allow qualitative comparisons of the nozzles. A pressure based SIMPLE solver, which delinks the density from the pressure during solution, was used [113]. The density was assumed to be constant in these simulations. Contours of the velocity were used to analyze the resulting cavitation behavior and dynamics. A schematic of the axisymmetric flow domain modeled with appropriate boundary conditions is shown in Fig. 4-4. The wall is modeled as a no-slip stationary wall as defined by ANSYS [113]. The axis of symmetry is considered the centerline of the geometry along which the flow domain is assumed to be symmetric [113]. The outlet is modeled as a pressure outlet with 0 MPa gauge pressure.

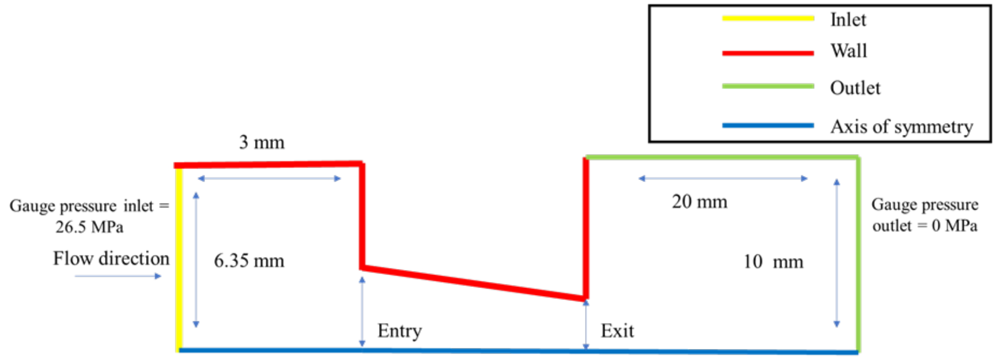

Fig. 4-4 Schematic of CFD flow domain of the inner jet flow in inner jet nozzles with varying taper.

4.4 Results and discussion

The maximum mass loss produced by a nozzle, which is an indicator of its cavitation intensity, is plotted as a function of the nominal area reduction in Fig. 4-5.

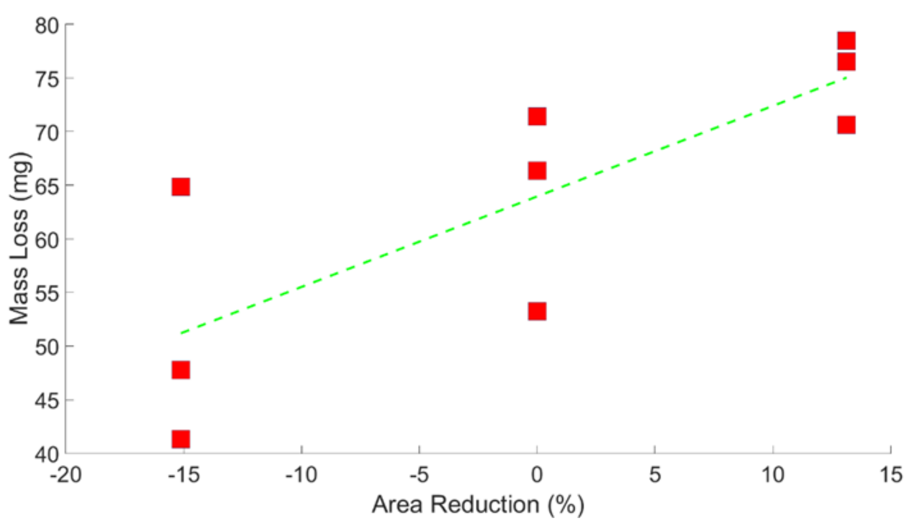

Fig. 4-5 Maximum Mass Loss versus Area Reduction for all nozzle replications.

As can be seen, there is a clear trend in the maximum mass loss with change in taper expressed as percentage area reduction. A linear regression model ($y = \beta_o + \beta_1 x$) was fit to the data as shown in Table 4-3.

Table 4-3 Linear Regression Model of Maximum Mass Loss vs. Area reduction (%).

	Estimate	Standard Error (SE)	p-value
Intercept	63.953	2.838	8.578e-08
Area Reduction (%)	0.844	0.245	0.010

The Pearson correlation coefficient, which describes the statistical correlation between the area reduction (%) and the maximum mass loss, is 0.7928. This indicates a strong positive correlation between the area reduction (%) and the maximum mass loss. However, there is significant variability in the maximum mass loss values for the diverging and zero taper nozzles. It is to be noted from Table 4-1 that the tapers defined by the area reductions vary slightly, which may contribute to some of the variability between replications of each nozzle variant. It can also be seen in Fig. 4-5 that the nozzle with converging taper is the most aggressive and produces the greatest mass loss.

A consolidated extended mass loss test plot showing the mean mass loss at all normalized standoff distances is shown in Fig. 4-6. The error bars seen in the figure are 95% confidence intervals.

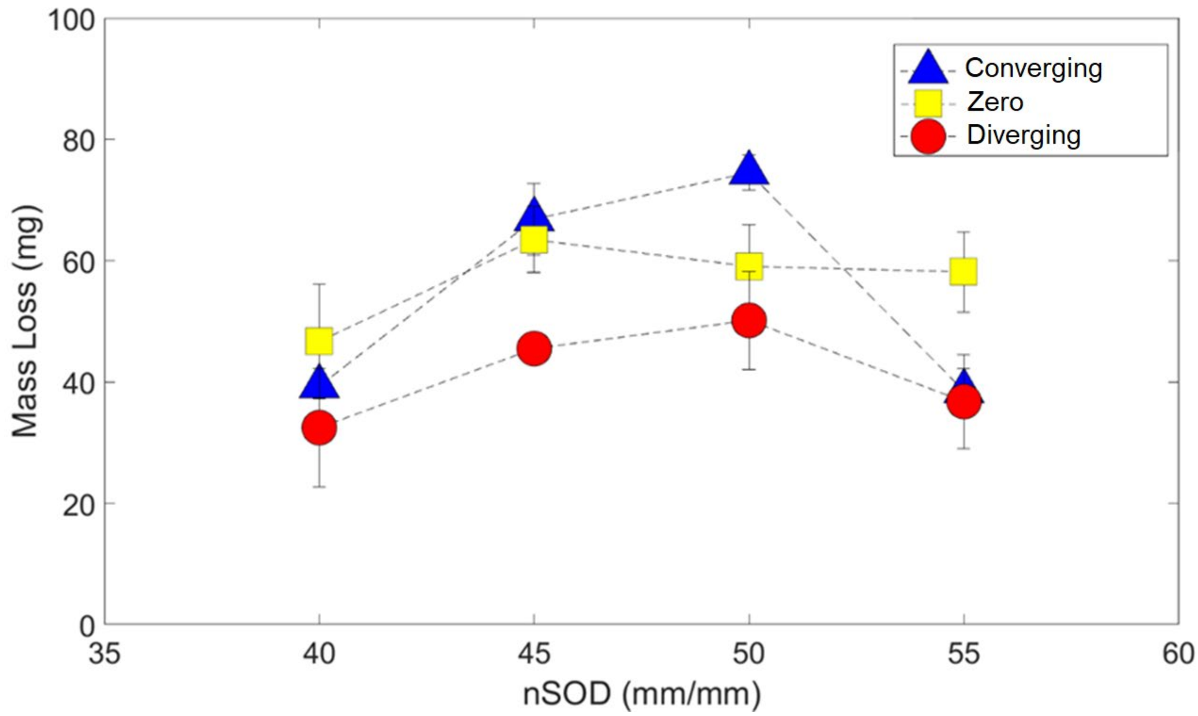

Fig. 4-6 Average mass loss results over a range of *nSOD* for nozzles of varying taper.

It can be clearly seen that the nozzle with converging taper produces the greatest mass loss among all nozzle variants, followed by the nozzle with zero taper. The average maximum mass loss produced by the converging taper nozzle is greater by 18% and 46%, respectively, than the mass loss produced by the zero and diverging taper nozzles. However, it can be seen that the zero taper nozzle exhibits less variation in mass loss across different *nSOD* values compared to the converging taper nozzle. This may prove useful for better process control in conditions where greater consistency in cavitation intensity is desired, such as during robotic arm assisted peening using co-flow cavitating jets. The coefficients of discharge (C_d) were also calculated for all nozzles and are listed in Table 4-4.

Table 4-4 Coefficient of discharge (C_d) for nozzles with varying taper.

	Diverging	Zero	Converging
C_d	0.64±0.008	0.65±0.006	0.74±0.008

It can be seen from Table 4-4 that the nozzle with converging taper has the highest value of C_d. This indicates that the energy losses inside the converging taper nozzle are less than the zero and diverging taper nozzles. Thus, the velocity difference between the inner jet and outer jet in the co-flow field for the converging taper nozzle is also greater than the velocity difference between the zero and diverging taper nozzles. The increased velocity difference may be responsible for the enhanced cavitation due to the shearing action of the co-axial flows.

Next, strip curvature measurements with the most aggressive replication of each nozzle variant at their respective optimum *nSOD* values (given in Appendix A1) were carried out to evaluate the effect of greater cavitation intensity on the compressive residual stresses produced in the material, seen in Fig. 4-7.

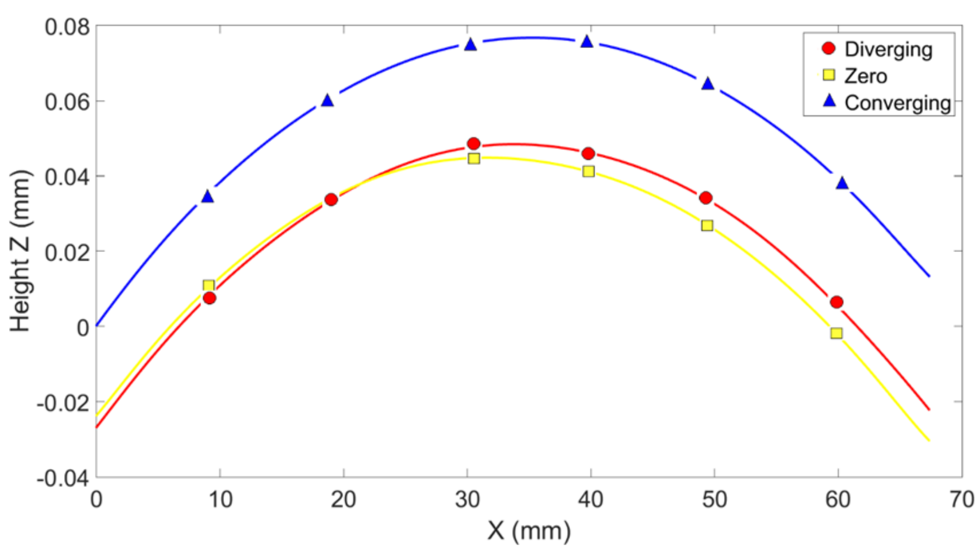

Fig. 4-7 Strip curvature profiles obtained with nozzles of varying taper at their respective optimum *nSOD* values.

As can be clearly seen in Fig. 4-7, the arc height of the strip peened by the converging taper nozzle is the greatest followed by the nozzles with zero and diverging taper. The arc height generated by peening with the nozzle with converging taper is higher by 59% than the arc height generated by the nozzle with diverging taper.

This validates the results of the mass loss tests. As further validation, impulse pressure measurements were carried out on the most aggressive replication of all the nozzle variants at their respective optimum *nSOD* values. The cavitation intensity plots of the pressure fluctuation as a function of the radial distance measured from the center of the flow are shown in Fig. 4-8.

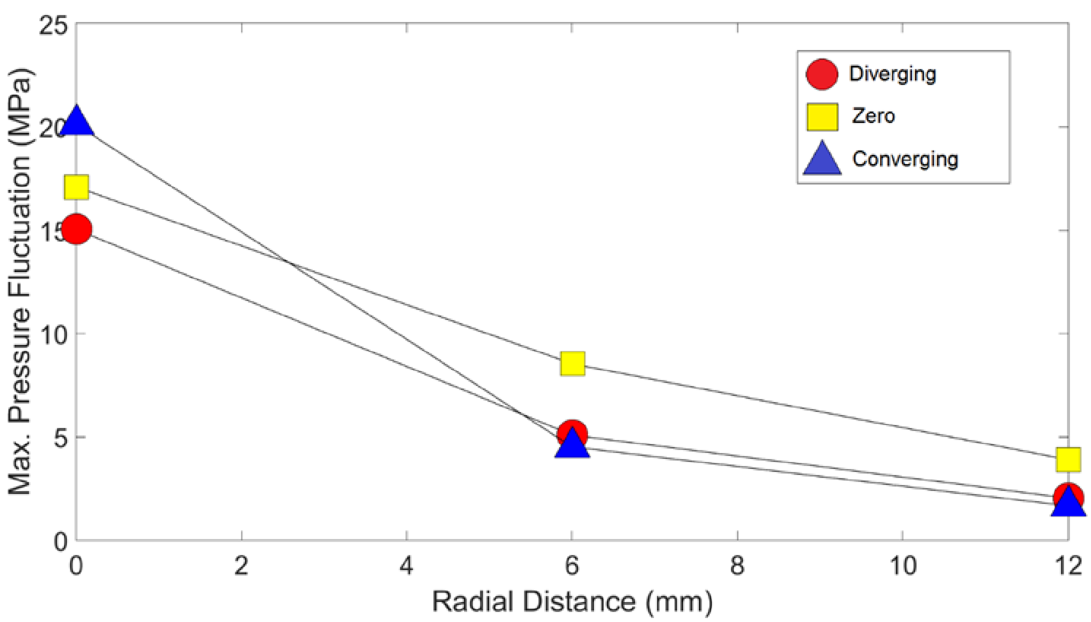

Fig. 4-8 Maximum pressure fluctuations in radial direction.

The cavitation intensity recorded by the pressure transducer is greatest at the center of the cavitating jet for all the nozzle variants. It can also be seen that the maximum pressure fluctuation, which is an indication of cavitation intensity, is greatest for the converging taper nozzle, followed by the nozzles with zero and diverging taper, respectively. However, the maximum pressure fluctuations at other radial distances are greater for the zero taper nozzle followed by the nozzles with diverging and converging taper.

From the time history signal of each nozzle variant, an approximately equal number of cavitation events were obtained by setting a threshold of 0 MPa, which were binned according to their amplitudes to obtain the frequency distributions shown in Fig. 4-9. The frequency distribution of cavitation events produced by the converging taper nozzle exhibits a longer tail, seen in the insets in Fig. 4-9, than the frequency distributions for the diverging and zero taper nozzles, indicating a larger occurrence of higher intensity events.

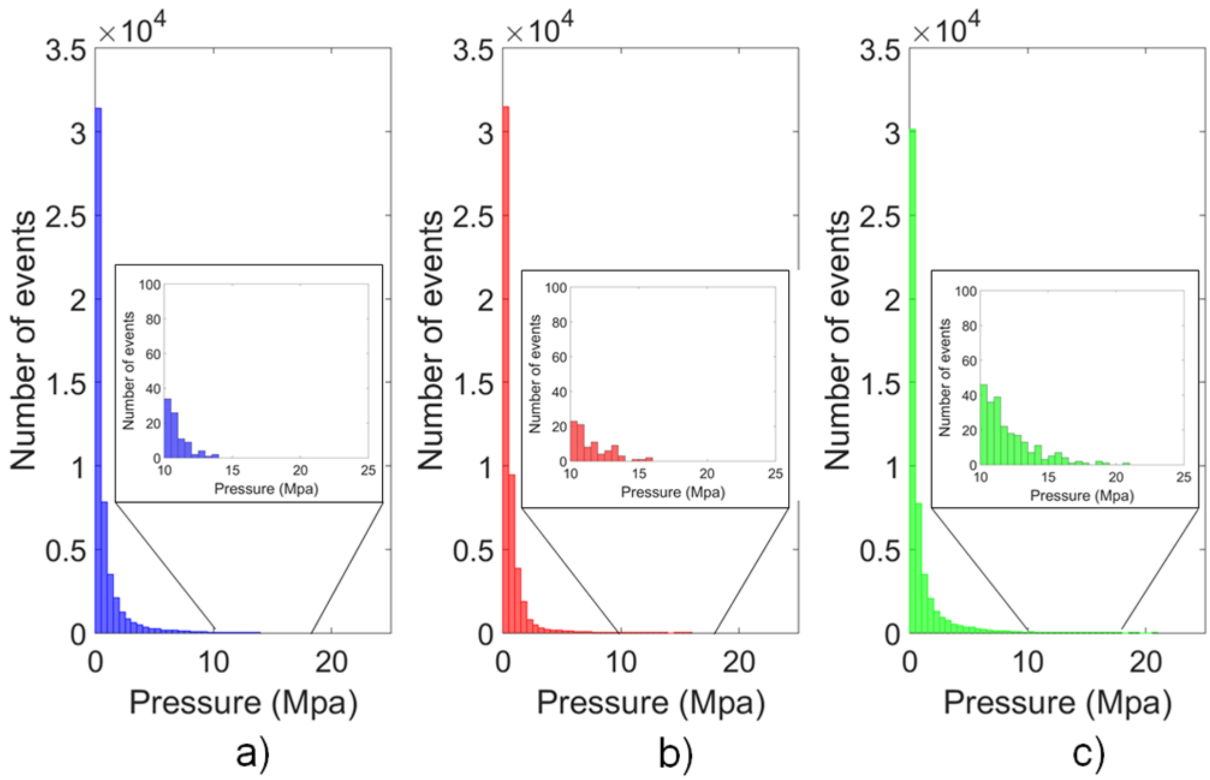

Fig. 4-9 Frequency distribution of cavitation events obtained for nozzles with a) diverging taper, b) zero taper, and c) converging taper.

It can be seen from Fig. 4-9 that the frequency of high intensity cavitation events (defined here as cavitation events with pressure amplitudes greater than 12 MPa) is 3.5 Hz, 26 Hz, and 33.8

Hz for the nozzles with diverging, zero and converging taper, respectively. Thus, the impulse pressure measurements provide further proof of the enhanced cavitation intensity of the nozzle with converging taper compared to the nozzles with zero and diverging taper.

The greater coefficient of discharge seen with nozzles of converging taper potentially leads to greater exit velocities and greater shear in the co-flow field, which results in greater cavitation intensity. The RANS simulation of the inner jet nozzle flow in nozzles with varying taper sheds light on this potential behavior of the converging taper nozzle, which is discussed next.

Specifically, the RANS single phase flow simulations for the diverging, zero, and converging taper nozzles yield the following volume flow rates computed from the axial velocity components at the outlet of the orifices: 1.062×10^{-4}, 1.040×10^{-4}, 1.115×10^{-4} m^3/s, respectively. Trend wise, the simulations show that the converging taper nozzle generates greater flow rates than the diverging and zero taper nozzles by ~5 % and ~7 %, respectively, which are significant since the variability in the area averaged velocity with reducing mesh size was found to be less than 0.5 %. However, these flow rates are higher by ~ 15 to 30 % compared to those observed experimentally, which range from 0.832×10^{-4} to 0.940×10^{-4} m^3/s going from diverging taper nozzles to converging taper nozzles. The single phase model clearly overpredicts the flow rates since it does not account for flow occlusion that occurs due to cavitation within the nozzle. This shortcoming of such single phase models solved using the SIMPLE scheme can be addressed with appropriate multi-phase simulations. Interestingly, the flow rate is higher for the diverging taper nozzle than the zero taper nozzle. This is because the nozzle orifice exit area is greatest for the diverging taper nozzle compared to the zero and converging taper nozzles.

The velocity magnitude variation in the radial direction from the axis of symmetry at the nozzle exit is plotted in Fig 4-10. It can be observed that the velocity magnitude variation is quite significant along the radial direction. The area averaged velocity values at the nozzle exit for the nozzle variants are given in Table 4-5. The converging taper nozzle has greater absolute velocity approaching the wall at higher radial distances compared to the zero and diverging taper nozzles. This leads to increased flow rates, which is reflected in the computed values mentioned earlier.

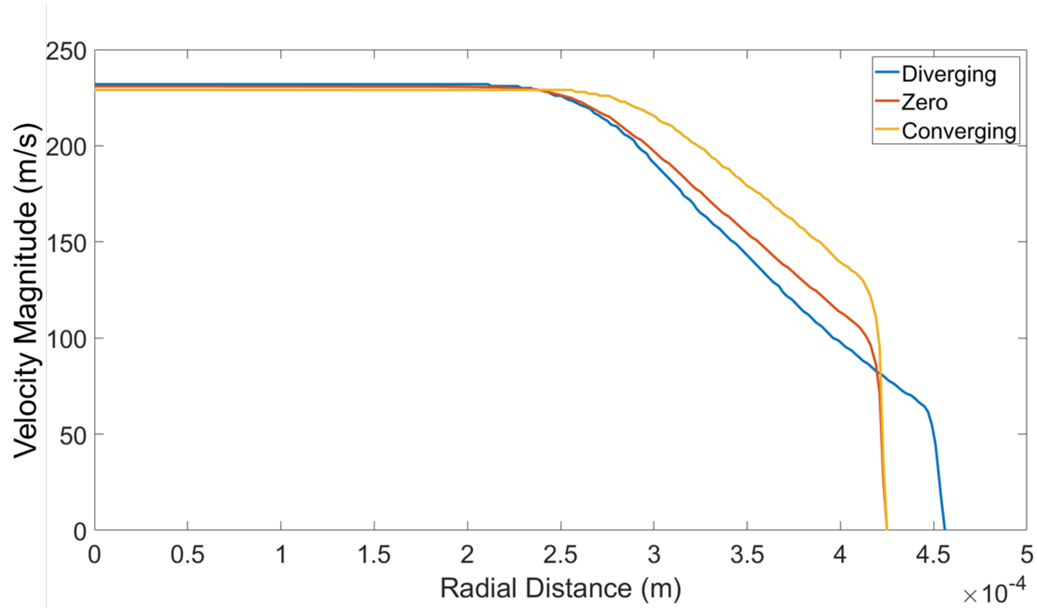

Fig. 4-10 Velocity magnitude variation with radial distance at nozzle exit for nozzles with varying taper.

The speed of sound in water at atmospheric temperature is 1500 m/s, which indicates that the Mach number in the nozzle is ~0.2 [81]. Compressibility effects start becoming significant as the Mach number approaches 1, thus validating the current approach with incompressible flow assumptions [113].

Table 4-5 Area averaged velocity magnitude for nozzle variants with varying taper.

Nozzle variant	Area Averaged Velocity at exit (m/s)
Diverging taper	162.69
Zero taper	183.38
Converging taper	196.97

These simulations confirm a higher area averaged exit velocity for the converging taper nozzle compared to the zero taper and diverging taper nozzles, which indicates greater potential for shear cavitation in the co-flow field with an inner jet nozzle orifice with converging taper compared to the diverging and zero taper nozzles.

In order to gain insight into the phenomenon of flow separation and its effect on the internal flow in nozzles with varying taper, absolute velocity contour maps are shown for the three different nozzle variants in Fig 4-11. A region of low velocity is seen close to the wall and is resolved further using velocity vector maps and appropriate conclusions are made with the information from these maps.

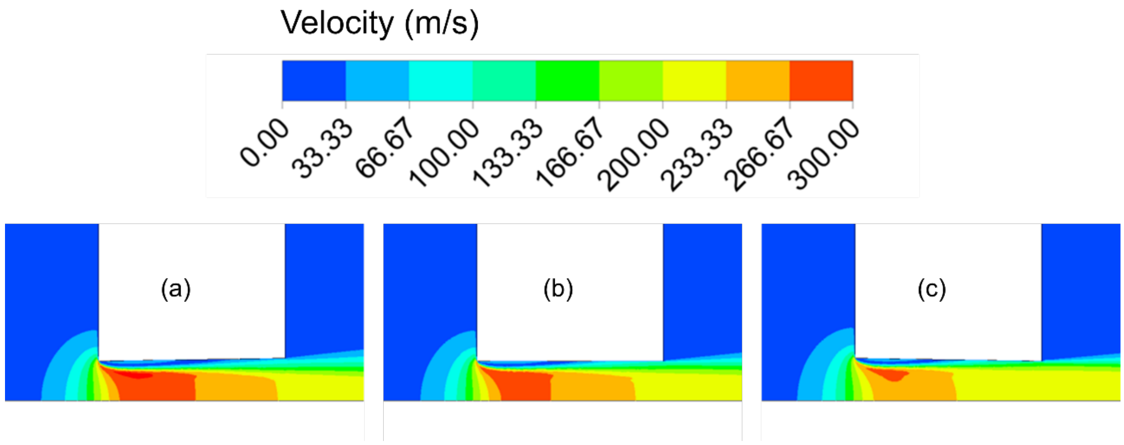

Fig. 4-11 Absolute velocity contour maps for nozzles of a) diverging, b) zero. and c) converging taper.

The corresponding velocity vector maps are depicted in Fig 4-12. It can be seen from the vector maps that there exists a region of flow separation and reversed flow close to the inlet of the nozzle, which can be verified visually in the magnified view of the vector map of the diverging taper nozzle shown in Fig. 4-12d.

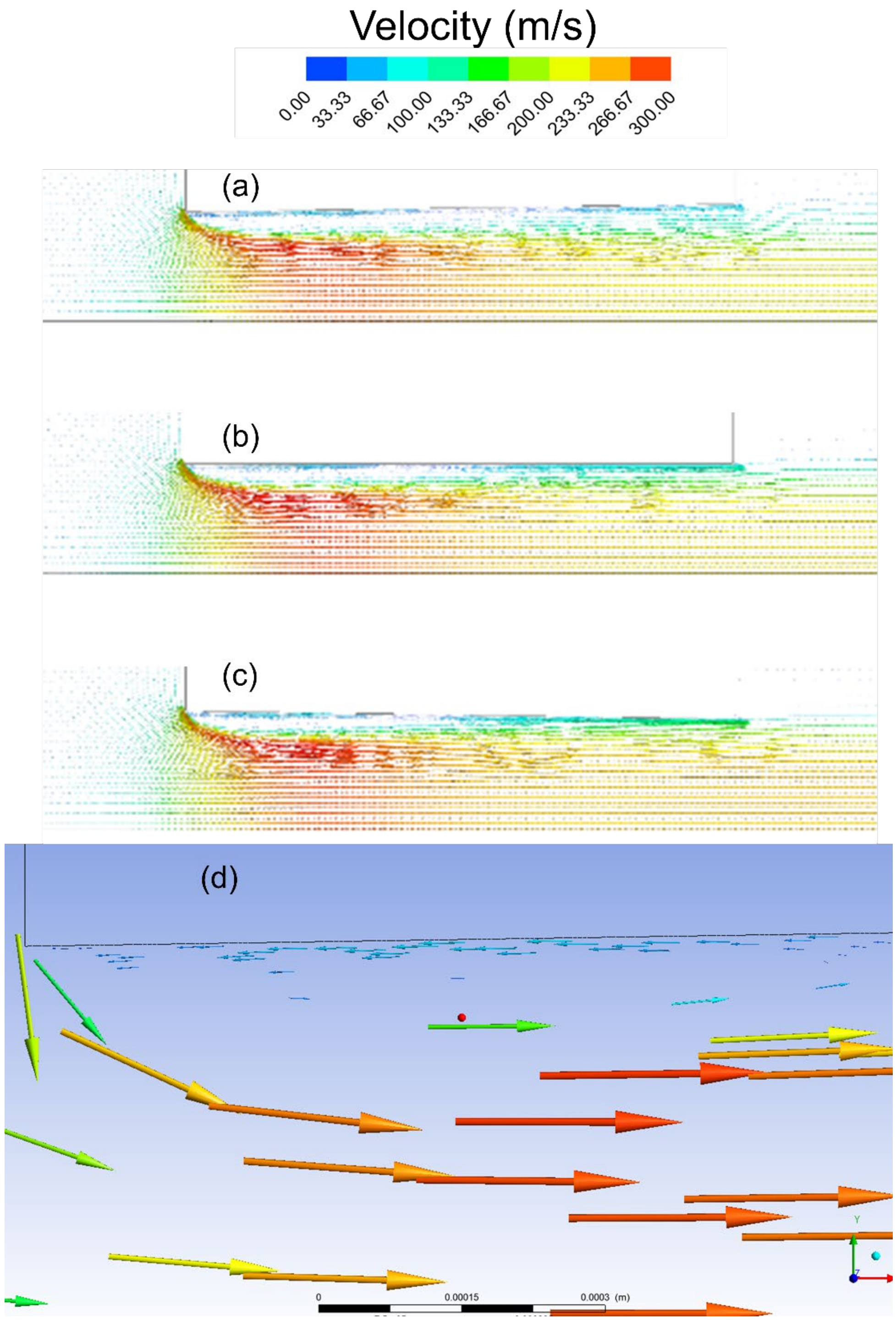

Fig. 4-12 Absolute velocity vector maps for nozzles of a) diverging, b) zero, and c) converging taper, and d) a close-up view of the flow separation zone near the inlet to the diverging nozzle.

An integral length scale to quantify the effect of flow separation in the internal flow of the nozzle is computed from the axial component of velocity. An integral length scale at any cross section perpendicular to the axis of symmetry in this case is defined as the radial distance from the axis of symmetry that contains 90 % of the total volume flow rate across that cross-section. This length scale is correlated to the length scale of the overall flow and is affected by the flow separation upstream of the nozzle exit. The greater the value of this integral length scale, the smaller is the magnitude of the flow separation, which has been shown by He et al. [87] to influence the coefficient of discharge, albeit for much lower pressures. The integral length scale is computed 0.3 mm upstream of the nozzle exit for the nozzles with varying taper and are listed in Table 4-6. However, this parameter does not show the effect of flow separation. This length scale can be non-dimensionalized by the radius of the orifice at the same axial location to understand the range of flow separation. The non-dimensional integral length scale for the converging taper nozzle is found to be ~ 5 % greater compared to the diverging taper nozzle. This indicates greater flow separation in the nozzle with diverging taper. However, a more rigorous investigation with significantly refined meshing at the wall and the corner radius at the nozzle inlet is required to fully understand flow separation in these nozzles.

Table 4-6 Value of integral length scales.

Nozzle variant	Value of integral length scale (m)	Non-dimensional integral length scale
Diverging taper	3.92×10^{-4}	0.867
Zero taper	3.82×10^{-4}	0.898
Converging taper	3.92×10^{-4}	0.907

4.5 Summary

This chapter presented an experimental and numerical study of the effect of inner jet nozzle orifice taper on cavitation intensity in co-flow water cavitation peening of aluminum 7075-T651 alloy. Nozzles of converging, zero and diverging taper were tested using extended mass loss and peening experiments. The main conclusions of the study are as follows:

1. The mass loss tests on Al 7075-T651 show that the nozzle with converging taper generates the greatest cavitation intensity. The mass loss produced by the converging taper nozzle is greater than the mass loss produced by the nozzles with zero and diverging taper by 18% and 46%, respectively. Thus, there exists a strong trend in the cavitation intensity with area reduction or alternatively taper, as shown through a simple linear regression model.
2. The strip curvature tests on Al 7075-T651 confirm the enhanced cavitation intensity of the nozzle with converging taper. The arc height produced by the nozzle with converging taper was greater than the arc height produced by the nozzles with zero and diverging taper by 65% and 59%, respectively.
3. The impulse pressure measurements show that the frequency and magnitude of high intensity cavitation events is greater in the case of the nozzle with converging taper, which can explain the enhanced cavitation intensity.
4. Results from extended mass loss, strip curvature and impulse pressure measurements indicate the higher inner jet exit velocity may be responsible for the greater cavitation intensity produced by the converging taper nozzle.
5. The steady state RANS CFD simulations of the internal flow in the inner jet nozzles show that the area averaged exit velocities are the greatest for the nozzle variant with converging

taper, which is likely responsible for greater shear in the co-flow field leading to greater cavitation intensity.

CHAPTER 5. EFFECT OF INNER JET NOZZLE ORIFICE LENGTH ON CAVITATION INTENSITY IN CO-FLOW WATER CAVITATION PEENING

5.1 Overview

The utility of co-flow water cavitation peening in surface treatment of aluminum alloys has been demonstrated through various studies. Compressive residual stresses, which enhance fatigue and fretting wear life, are developed in metallic surfaces treated with co-flow water cavitation peening due to inhomogeneous surface plastic deformation. However, for application in industry where processing time reduction and application to a wider range of materials is critical, there is a need to increase cavitation intensity in co-flow water cavitation peening, which requires detailed understanding of nozzle designs to obtain an optimum nozzle configuration. A significant nozzle design parameter that has not been investigated yet is the inner jet nozzle orifice length characterized with the non-dimensional ratio L_o/d. which is known to affect cavitation generation internal to the inner jet. In this study, extended mass loss and strip curvature experiments are employed to demonstrate the effect of the inner jet nozzle orifice length on cavitation intensity in co-flow water cavitation peening.

5.2 Experimental method

5.2.1 Experimental facility

The major dimensions of the nozzle assembly utilized for this study are listed in Table 5-1.

Table 5-1 Major dimensions of the co-flow nozzle.

d	0.95 mm
D_1	24 mm
D_2	6.8 mm
L_o	0.95 – 9.5 mm
β	75°
γ	70°

5.2.2 Experiment design

Analogous to previous studies on the effect of nozzle orifice length on atomization and jet breakup length, the nozzle orifice length (L_o) is non- dimensionalized by division with the diameter of the inner jet nozzle, d, yielding the ratio L_o/d. Keeping nozzle fabrication considerations in mind and the previous studies on atomization, four L_o/d ratios were selected by varying the inner jet nozzle orifice length as shown in Table 5-2.

Table 5-2 Inner jet nozzle design variants.

L_o	L_o/d
0.95 mm	1
1.9 mm	2
4.75 mm	5
9.5 mm	10

A schematic of the inner jet nozzles with varying $L_o\ /d$ ratios is shown in Fig 5-1. The nozzles were manufactured in an Accutex^{TM} Wire Electrical Discharge Machine (WEDM).

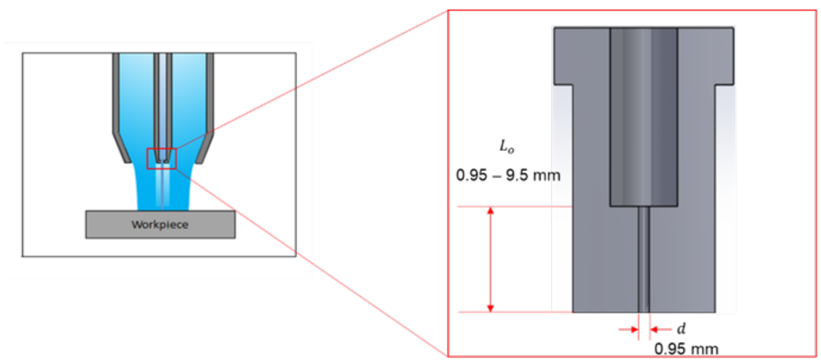

Fig. 5-1 Schematic of inner jet nozzles with varying L_o/d.

5.2.3 Extended mass loss tests

Although, mass loss is not desirable during peening, it is widely used as a measure of cavitation intensity [99]. Extended mass loss tests for 30 min on Al 7075-T651 (nominal composition as before) specimens were performed using the four nozzles at a pressure of 26±0.5 MPa giving an average inner jet nozzle exit velocity of 150 m/s for all nozzles. The outer jet velocity was fixed at 11 m/s for all inner jet nozzle variants consistent with the findings of previous studies wherein the optimum outer jet velocity was determined [99]. Water temperature was maintained at 303±3 K for the duration of the test since water temperature is known to influence cavitation [109]. The mass loss produced by the inner jet nozzle designs was measured as a function of standoff distance by an analytical scale with 0.1 mg resolution and 0.3 mg repeatability. The standoff distance was normalized by the inner jet nozzle diameter and is termed the normalized standoff distance (*nSOD*). Three repetitions of mass loss testing at each standoff distance were carried out.

5.2.4 Strip curvature test

From classical beam theory of elasticity, it is known that the introduction of residual stresses due to peening results in change in curvature of a long thin strip of plastically deformed material [101]. To obtain a measure of the residual stress produced in the aluminum samples, strip curvature tests were carried out by scanning 76 mm x 19 mm x 6.35 mm strips of Al 7075-T651 with a pitch of 1 mm and scan speed of 480 mm/min at the optimum standoff distance determined in the mass loss tests previously described. The strips were peened through six passes resulting in a total processing time (t_p) of 18 min for each strip. A plan view schematic of the peening pattern employed in each pass can be seen in Fig. 5-2. Measurement of the strip arc profile was made with a scanning Coordinate Measuring Machine (CMM) using a probe tip diameter of 1.5 mm.

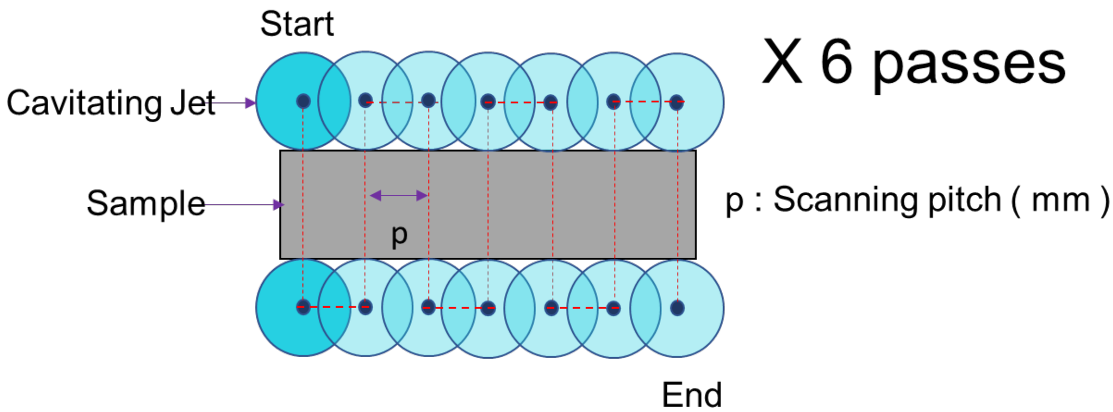

Fig. 5-2 Plan view schematic of the scanning pattern for strips peened at the optimum standoff distance for nozzles with varying L_o/d ratios.

5.3 Results and discussion

The results of the extended mass loss tests performed on Al 7075-T651 at various *nSOD* values are shown in Fig. 5-3a. It can be seen that the nozzle with a L_o/d ratio of 2 generates the greatest mass loss at *nSOD* of 45 compared to the other nozzles. The optimum *nSOD* values for the nozzles with L_o/d ratios of 1,5 and 10 are 40,45 and 50 respectively. A plot of the average maximum mass loss produced by each nozzle is shown in Fig. 5-3b. It is seen that the mass loss produced by the nozzle with L_o/d ratio of 2 is higher than the mass loss produced by the other L_o/d ratios. The inner jet nozzle with an L_o/d ratio of 2 was shown to generate 34 %, 71 % and 72 % greater cavitation intensity, measured via mass loss as compared to the other inner jet nozzles with L_o/d ratios of 1, 5 and 10 respectively. The error bars represent 95% confidence intervals.

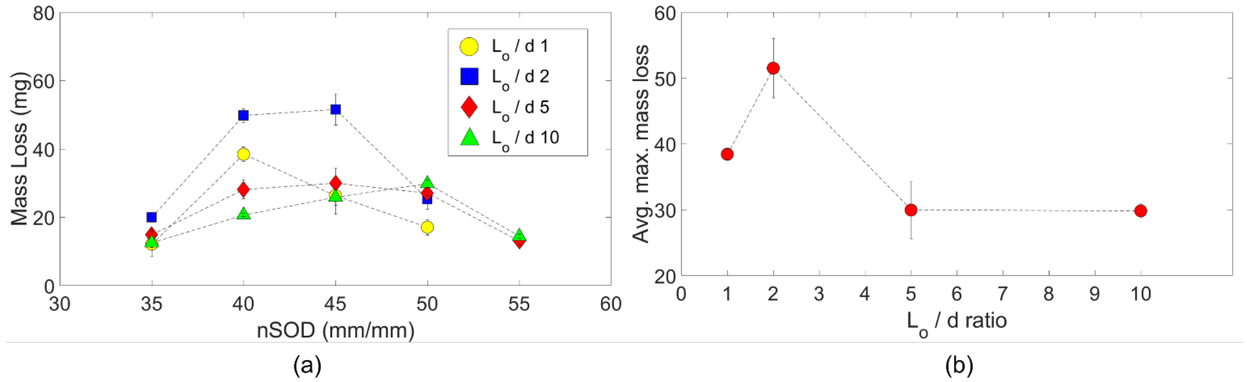

Fig. 5-3 Mass loss variation with *nSOD*, b) average maximum mass loss variation with L_o/d ratio.

Thus, it is seen that the inner jet nozzle orifice length influences the cavitation intensity due to inner jet internal flow phenomena such as flow separation and reattachment. The mass loss trends seen in Fig. 5-3a are also evident in the peening results as seen from the strip curvature results shown in Fig. 5-4. Note that the strip curvature tests were conducted at the respective optimum *nSOD* values for each nozzle variant. The error bars represent 95% confidence intervals.

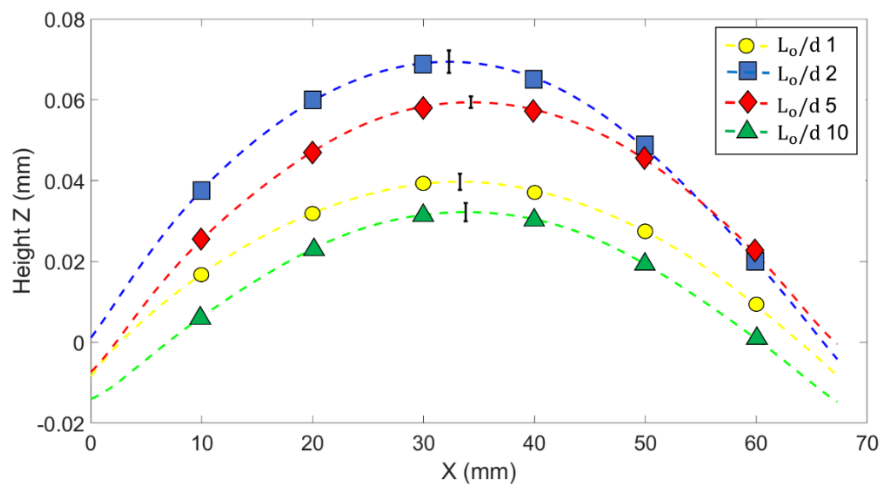

Fig. 5-4 Strip curvatures produced by nozzles with varying L_o/d ratios.

It can be seen the peak height of the average strip curvature produced by the nozzle with L_o/d of 2 is the greatest followed by L_o/d of 5, 1 and 10. The strip curvature tests were conducted at the *nSOD* at which each nozzle variant produced the greatest mass loss. The peak height of the strips is an indication of the peak residual stress generated in the workpiece surface layers. This confirms the enhanced cavitation intensity of the nozzle with L_o/d ratio of 2 translates equally well to its peening ability. Interestingly, the maximum peak height of strip curvature produced with nozzle with L_o/d of 5 is greater than the arc height produced with L_o/d of 1 indicating the need for impulse pressure measurements to understand cavitation cloud behavior in the nozzles with varying nozzle orifice length.

5.4 Summary

An experimental investigation of the effect of inner jet nozzle orifice length, characterized by the L_o/d ratio, was conducted using extended mass loss and strip curvature experiments. The following conclusions can be drawn from this chapter on the effect of L_o/d ratio on cavitation intensity in co-flow cavitation peening.

1. The mass loss produced by the L_o/d ratio of 2 is greater than the mass loss produced by nozzles with L_o/d ratios of 1, 5 and 10 indicating the enhanced cavitation intensity of the inner jet nozzle with L_o/d ratio of 2. This indicates the role of the inner jet nozzle orifice length on cavitation intensity in co-flow cavitation peening.
2. Strip curvature measurements confirm the enhanced cavitation intensity of the inner nozzle with L_o/d ratio of 2. The peak heights of the strip curvatures produced with the other inner jet nozzles are lower than the peak strip arc height seen with the inner jet nozzle L_o/d ratio of 2.

CHAPTER 6. ENHANCING CAVITATION INTENSITY IN ULTRASONIC SURFACE MODIFICATION THROUGH POLYMER ADDITIVES: APPLICATION TO PEENING

6.1 Overview

Cavitation peening is a surface treatment technique that manifests in several configurations. One such configuration utilizes an ultrasonic horn to produce an oscillating pressure field, which in turn produces a cavitation cloud. The cavitation cloud collapses on the metal surface it is directed at and generates plastic deformation and pitting of the surface. Such surface deformation and modification can generate beneficial surface compressive residual stresses. As a result, this process can be used to treat small metal surface areas for enhancement of their fatigue or wear resistance. However, there is a practical need for treating the engineered surfaces of a wide range of metals in a time efficient manner, which can be achieved by enhancing the cavitation intensity. In this study, a range of concentrations of a polymer additive (polyethylene oxide) in water are tested and their effect on cavitation intensity quantified. Extended mass loss tests are first conducted on a relatively soft Aluminum alloy (1100-O) to determine a polymer concentration that enhances cavitation intensity. High speed videography of different polymer concentrations reveals a significant difference in the behavior of the cavitation clouds produced in water versus in the aqueous polymer solution. A PVDF sensor is used to characterize the cavitation intensity. Ultrasonic peening experiments on a structural aluminum alloy (Al 7075-T651) with water and with an aqueous polymer solution of a specific concentration are conducted to show greater surface roughening, which is an indication of enhanced plastic deformation, and therefore demonstrate potential for more efficient peening with aqueous polymer solution.

6.2 Experimental method

6.2.1 Experimental facility

A 12.7 mm diameter ultrasonic horn with flat tips immersed in water or polymer solution and powered by a sonifier (Branson SFX 550) was used to generate cavitation in this study. A schematic of the ultrasonic horn immersed in a liquid is shown in Fig. 6-1.

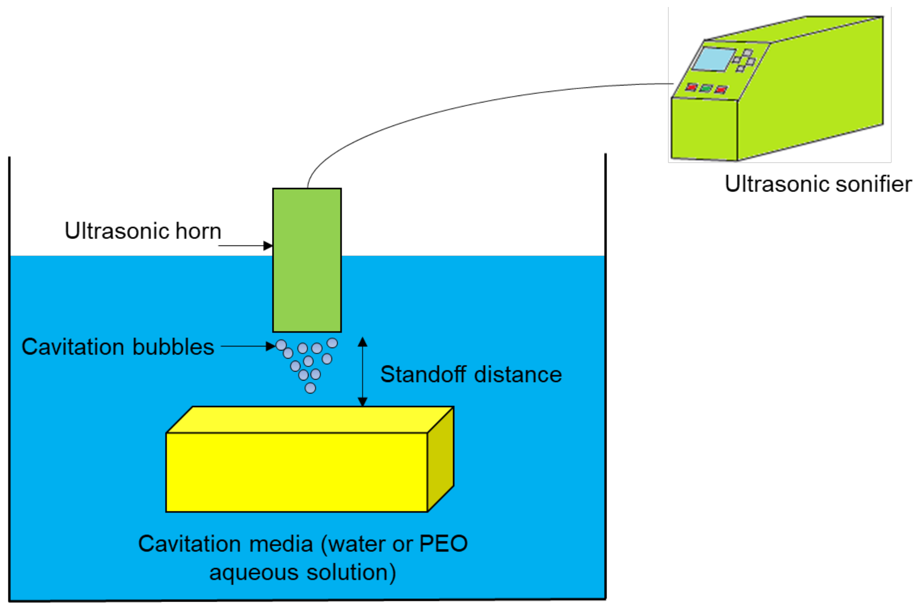

Fig. 6-1 Schematic of experimental setup with ultrasonic horn and sonifier.

6.2.2 Experiment design

A range of aqueous polymer solutions with varying concentrations of water-soluble polyethylene oxide (PEO) of molecular weight of 8000, henceforth referred to as aqueous PEO solutions, were used in the experiments. The experimental process parameters and their values are listed in Table 6-1.

Table 6-1 Experimental parameters.

Working mode of sonifier	Continuous
Frequency	20 kHz
Amplitude	84 µm
Standoff distance	2 mm, 5 mm, and 8 mm
Cavitation media	Polyethylene Oxide (mol. wt. 8000) solutions in tap water
Concentration	1000, 4000, 8000 and 16000 wppm used for mass loss and PVDF characterization of cavitation 500, 1000, 2000, 4000, 8000 and 16000 wppm used for for high-speed videography of cavitation
Workpiece materials	Aluminum (Al) 1100-O for mass loss experiments and Al 7075-T651 for peening experiments
Temperature of solutions	25±3 ˚C

6.2.3 Extended mass loss tests

Extended mass loss tests of 30 min duration each were conducted with water only, and with aqueous PEO solutions with concentrations of 1000 wppm, 4000 wppm, 8000 wppm, and 16000 wppm. The cavitation clouds produced in these tests were made to impinge on 20.3 mm x 20.3 mm x 3.1 mm Al 1100-O samples located at standoff distances of 2 mm, 5 mm and 8 mm from the horn tip. Extended mass loss tests on Al 1100-O were conducted to identify a PEO concentration in water and standoff distance that increased cavitation intensity. Al 1100-O and other soft aluminum alloys are typically used to perform mass loss tests since such values are then readily comparable [88]. To discount the effects of polymer solution degradation due to breakage of polymer chains and due to increase in temperature during sonication, the aqueous PEO solution was replaced after 10 minutes. The mass loss of workpiece samples was measured using a weighing scale with 0.1 mg resolution and 0.3 mg repeatability.

6.2.4 High-speed imaging

High-speed imaging of the cavitating clouds was performed at 58457 frames per second (fps) using a high-speed video camera (Phantom VEO 410L) with resolution of 256 × 256 pixels and a Nikon 50 mm f1.8 lens. A representative set of 30000 images was collected from the region below the horn and analyzed. An image processing algorithm for delineating the shape of the cloud, like that reported in [64] and [99], was used. The widths of cavitation clouds were determined from these images. A schematic of the high-speed videography setup is shown in Fig. 6-2.

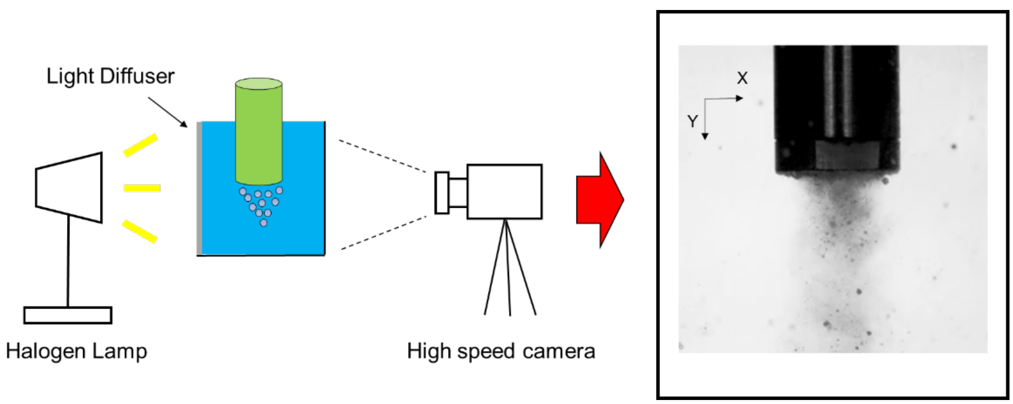

Fig. 6-2 Schematic of high-speed videography.

6.2.5 Cavitation intensity measurements

Cavitation intensity measurements of the cavitation cloud at a specific (2 mm) standoff distance were carried out using a polyvinylidene fluoride (PVDF) sensor (TE^{TM} 223-1318-ND) with a pressure sensitive area of 885 mm^2, placed between hardened 420 stainless steel plates.

Calibration of the sensor was carried out using the ball drop method [116]. The PVDF sensor measurements were band pass filtered using a Krohn-HiteTM 3202 (R) analog band pass Butterworth filter operating between 20 kHz and 500 kHz and a digital NI data acquisition device sampling at 1 MHz (Fig. 6-3). A peak in the time history of the PVDF signal is taken as a cavitation impact event as in the work of Singh et al. [66]. The number of events in the measured PVDF signal for water and for the aqueous PEO solutions were binned and compared. As is well known, for plastic deformation and subsequent erosion to occur, impacts of a certain threshold must occur. Hence, the number of events above a defined threshold are compared to distinguish between the cavitation intensities of water and the different aqueous PEO solutions.

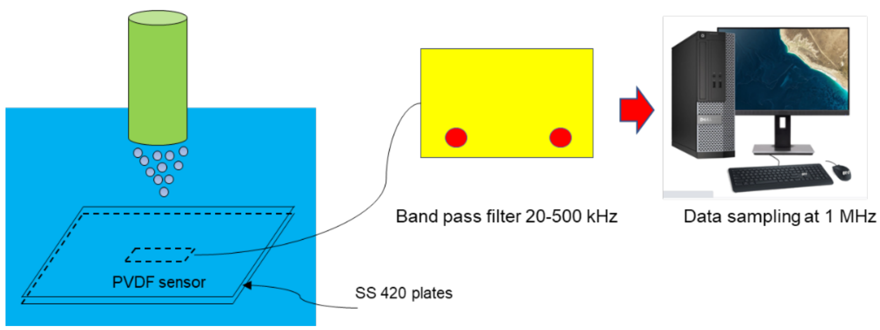

Fig. 6-3 Schematic of PVDF cavitation intensity measurements.

Peening of Aluminum 7075-T651, a structural aluminum alloy of engineering significance in the aerospace industry, was carried out on a 25.4 mm x 6.3 mm x 3.1 mm sample at a standoff distance of 2 mm and a scan speed of 48 mm/min for a total of 28 passes with 100% coverage in each pass for a total exposure time of 336 s. Surface roughness measurements and optical micrographs for visual comparison of the erosion pattern and analysis of pitting produced with water and aqueous PEO solutions were acquired using a white light optical surface profiler (Zygo ZeGage) and a digital optical microscope (Leica DVM6), respectively.

6.3 Results and discussion

The extended mass loss results for Al 1100-O exposed to ultrasonic cavitation with water only and with different aqueous PEO solutions is shown in Fig. 6-4a. The error bars shown correspond to 95 % confidence intervals. It can be seen that at a standoff distance of 2 mm the mass loss produced by the 1000 wppm PEO solution is significantly greater than the mass loss produced by water and the other PEO concentrations. As compared to water only, the mass loss produced by the 1000 wppm PEO solution is greater by 69 %. The 1000 wppm and 16000 wppm aqueous PEO solutions also produced greater mass loss than just water at a standoff distance of 5 mm. These results indicate that aqueous PEO solutions of certain concentrations, especially 1000 wppm, have the potential to enhance cavitation intensity and effect greater surface modification that could be beneficial for peening applications.

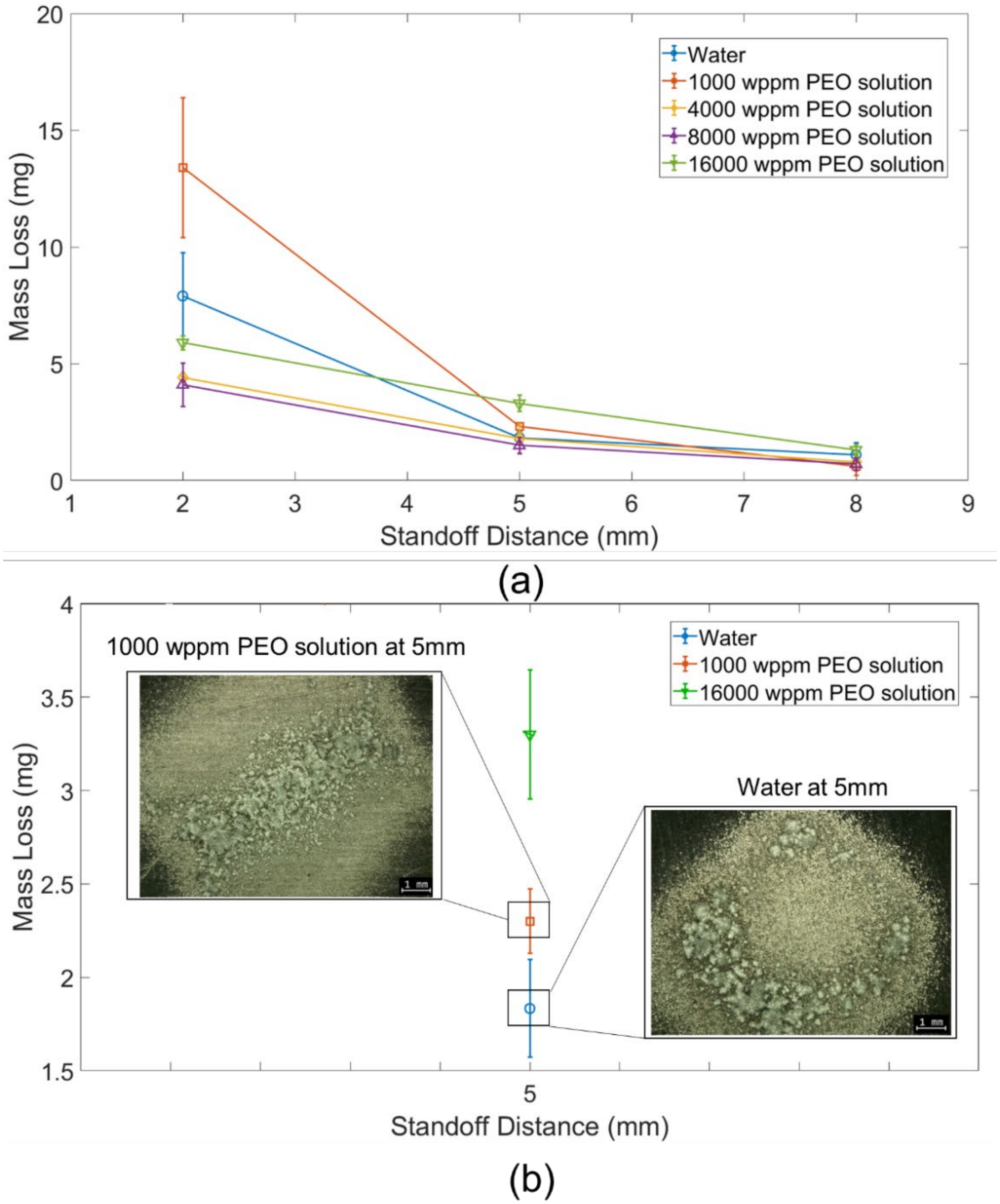

Fig. 6-4 Extended mass loss versus standoff distance and b) extended mass loss at 5 mm standoff distance for water, 1000, and 16000 wppm aqueous PEO solutions.

The extended mass loss results for water, 1000 wppm, and 16000 wppm aqueous PEO solutions at a standoff distance of 5 mm are shown in Fig. 6-4b. Representative optical micrographs of the erosion patterns obtained at 5 mm standoff distance for the 1000 wppm aqueous PEO solution and water only are also shown in Fig. 6-4b and clearly illustrate the differences in cavitation cloud induced workpiece damage characteristics for the two cases. It is observed that the erosion pattern generated by the water cavitation cloud is more diffuse and circular than the erosion pattern produced by the 1000 wppm aqueous PEO solution, which is more intense in the center and corresponds more closely to the shape of the rectangular horn tip. This result also suggests that the aqueous PEO solution is able to sustain the cavitation cloud at longer distances from the horn tip since the cavitation cloud formed in water produces a diffused and approximately circular erosion pattern. In contrast, the erosion pattern seen with the 1000 wppm aqueous PEO solution retains the rectangular shape of the horn tip. It is known that the shape of the horn tip controls cavitation cloud shape and determines the cavitation intensity variation as the distance from the horn tip increases [117]. Hence, an erosion pattern that retains the rectangular shape of the horn tip indicates sustenance of the cavitation cloud over longer distances.

High-speed video images for water and aqueous PEO solutions of different concentrations were also analyzed to confirm this hypothesis and representative still images extracted from the videos are shown in Fig. 6-5a-g for water, 500, 1000, 2000, 4000, 8000, and 16000 wppm aqueous PEO solutions, respectively. It can be seen from the still images in Figs. 6-5b-g that, in general, the cavitation cloud (dark region below the horn tip) is more intense for all aqueous PEO solutions compared to the cloud formed in water only (Fig. 6-5a).

The average maximum cloud widths, which is a measure of the cloud size and shown to be correlated with cavitation intensity, are determined from the still images at standoff distances of 2, 5, and 8 mm for water and the different PEO solutions and plotted in Fig. 6-5h [64]. The average maximum cloud width is obtained from ten (10) measurements of maximum cloud widths corresponding to ten (10) images from the larger set described earlier. The error bars shown correspond to 95% confidence intervals.

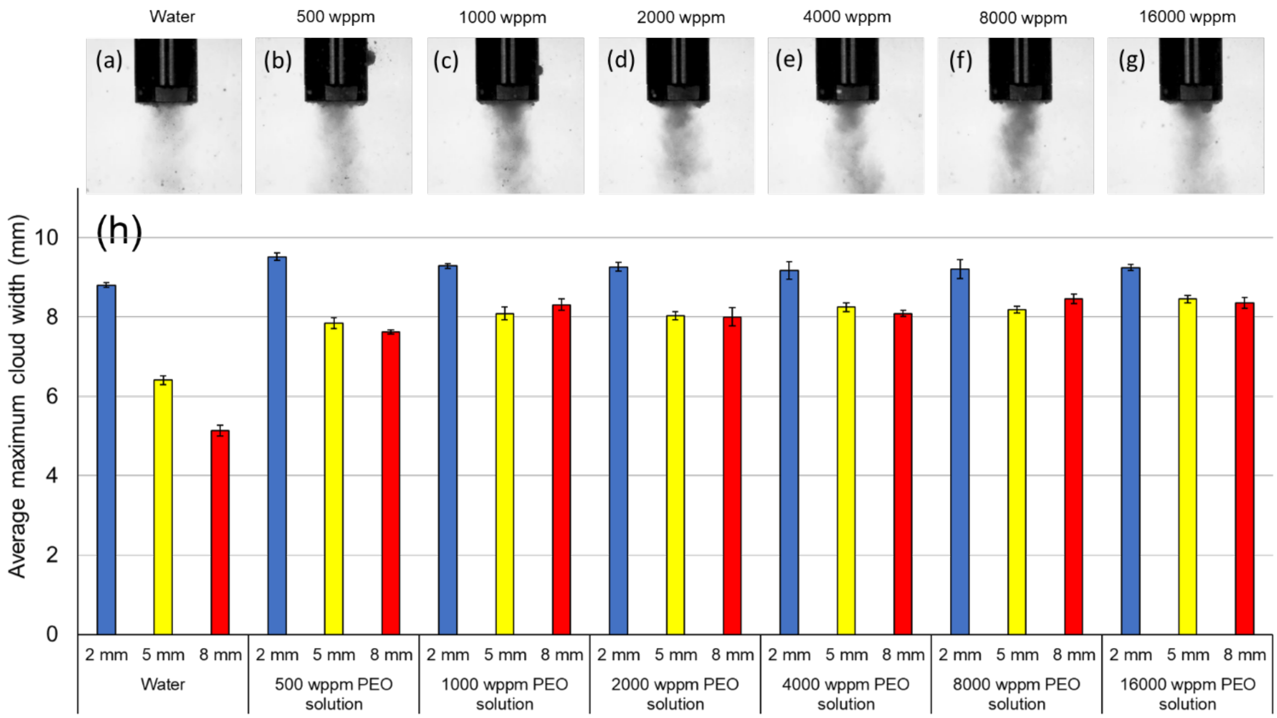

Fig. 6-5 Still images extracted from the high-speed videos for a) water and aqueous PEO solutions with concentrations of b) 500 wppm, c) 1000 wppm, d) 2000 wppm, e) 4000 wppm, f) 8000 wppm, g) 16000 wppm, and h) average maximum cloud widths for water and the PEO solutions at standoff distances of 2, 5 and 8 mm.

It can be seen from the figure that for all aqueous PEO solutions, the average maximum cloud widths are greater than for water alone, irrespective of the standoff distance, thus indicating an increase in cavitation intensity with polymer addition to water. In particular, the differences between the cloud widths for water and the PEO solutions are greater at larger standoff distances. This confirms the hypothesis that the cavitation clouds produced in the PEO solutions are sustained over longer distances thus explaining the differences in the erosion patterns seen in Fig. 6-4b.

It is well known that cavitation phenomenon benefits from the presence of heterogenous sites for nucleation [118]. Molecular dynamics studies have shown that the presence of nano particles in the fluid has the potential to promote cavitation by decreasing the free energy of critical bubbles [119]. This is in line with the high-speed imaging evidence presented in this chapter that shows greater cavitation activity with the aqueous PEO solutions. Therefore, it is likely that the greater average maximum cloud widths seen in the PEO solutions are a result of the PEO molecular chains in the solution serving as nucleation sites for cavitation inception. Surface tension is also known to decrease with increasing concentration of PEO water soluble polymer of molecular weight of 8000 [96]. Cavitation erosion rates are also known to be negatively influenced by a decrease in the surface tension of the fluids, indicating a possible link between the concentration of polymers and cavitation inception [97].

It is hypothesized that the increased cavitation inception in PEO aqueous solution seen with the greater average maximum cloud widths, the mass loss should also exhibit a monotonic increase with PEO concentration. However, this is not evident in the mass loss results seen earlier in Fig. 6-4a. The drop in surface tension with increasing PEO concentration offers a possible explanation for this phenomenon. It is speculated that the increase in cavitation inception and decrease in surface tension as the PEO concentration increase act as counter-mechanisms to each other. This may explain why certain PEO aqueous solutions generated greater mass loss compared to pure water. Thus, although the specific enhancement of cavitation intensity in this case may be attributed to the enhanced cavitation inception and reduced surface tension, this explanation requires further investigation. Also, the cloud width is an incomplete measure of cloud volume and intensity, which is difficult to measure. Furthermore, it is known that for higher polymer concentrations the rate of mass loss decreases with exposure time due to polymer degradation caused by sonication [23]. Therefore, while the cloud width measure does correlate with increased cavitation in aqueous PEO solutions compared to water alone, it does not correlate completely with the mass loss trends seen in Fig. 6-4a, which shows that cavitation intensity at a standoff distance of 2 mm is strongest in the 1000 wppm aqueous PEO solution. It is also worth noting that the high-speed videography was carried out with aqueous PEO solutions that were not subject to any prior sonication, i.e, they were fresh PEO solutions. The effects of degradation on PEO solutions have to be studied with a test that takes into account a longer duration and effects of sonication. Therefore, an alternate measure of cavitation cloud characteristics as a function of polymer concentration that better correlates with its effect on the workpiece surface (hence mass loss) is necessary.

Since mass loss from the workpiece surface occurs over time due to the cumulative effect of impacts at the workpiece surface generated by cavitation cloud collapse events, PVDF sensor-based cavitation impact measurements were carried out at a standoff distance of 2 mm. To study the time evolution of cavitation intensity as a function of time and to account for possible degradation of the aqueous PEO solution, the signal was captured at 30 s intervals between successive measurements for a total duration of 600 s (10 min). This duration corresponds to the time for which the polymer solution was subjected to sonication during the mass loss tests and therefore should account for any polymer degradation that occurred during the mass loss tests over a 10 min period. Based on a threshold sensitivity study, a threshold of 6.5 kN was used to delineate the high intensity impact events responsible for surface modification. A plot of the time evolution of the cumulative number of impact events (over a 5 s period) exceeding the 6.5 kN threshold is shown in Fig. 6-6. It can be seen that the cumulative number of impact events for the 1000 wppm aqueous PEO solution for than the other polymer concentrations and for water alone. However, it is also noted that the 4000, 8000, and 16000 wppm PEO solutions are also characterized by a greater cumulative number of high intensity events compared to water alone, which is in contrast to the trends in mass loss for these concentrations relative to water alone. It is worth noting that the mass loss data in Fig. 6-4a corresponds to cavitation cloud collapse events that directly impact the Al 1100-O sample, which has a smaller surface area compared to the size of the PVDF sensor. Consequently, the PVDF sensor registers cloud collapse events over a much larger surface area resulting in cumulative number of impact events for the 4000, 8000, and 16000 wppm PEO solutions that are greater than for water alone.

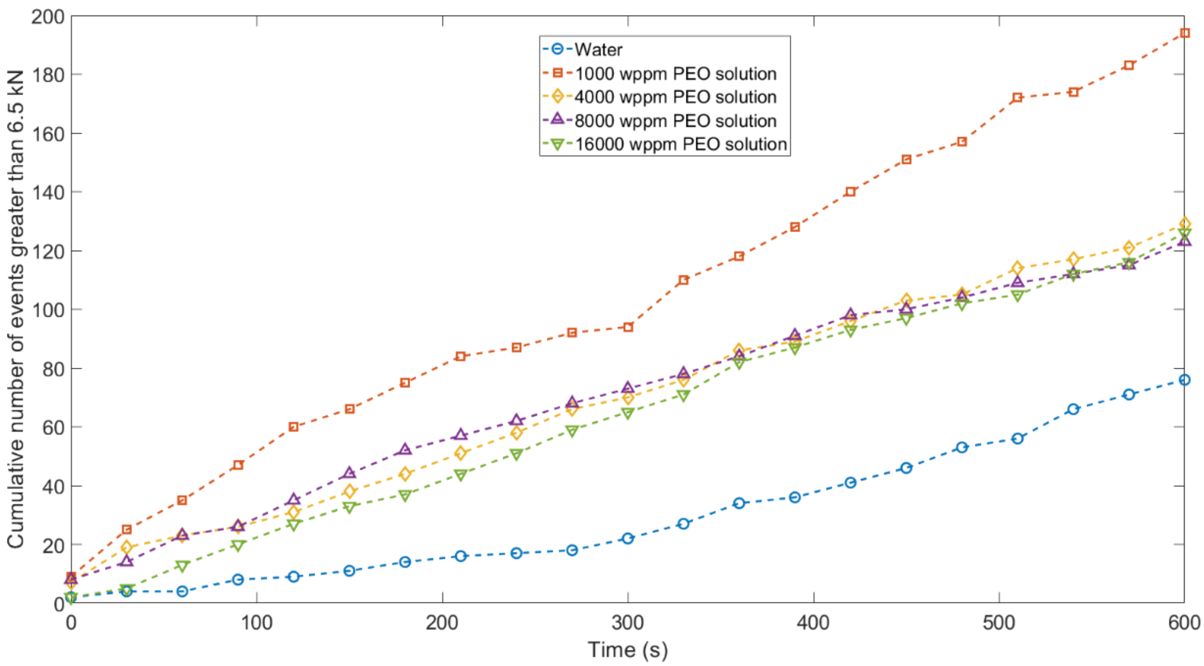

Fig. 6-6 Cumulative number of cavitation impact events (> 6.5 kN) in water and aqueous PEO solution.

In addition to analyzing the time evolution of cavitation impact events, the effects of ultrasonic cavitation surface treatment with water and with the 1000 wppm PEO solution on the arithmetic areal average surface roughness (S_a) of Al 7075-T651 samples were evaluated and are shown in Fig. 6-7a. The error bars shown correspond to 95 % confidence intervals. Optical micrographs at 100x magnification showing the pit morphologies obtained with water and the 1000 wppm aqueous PEO solution after processing for 240 s are shown in Fig. 6-7b and Fig. 6-7c, respectively. It is seen that the surface roughness is generally higher for the 1000 wppm aqueous PEO solution than for water, thus indicating greater surface plastic deformation (characterized by pitting) due to more intense cavitation impact events.

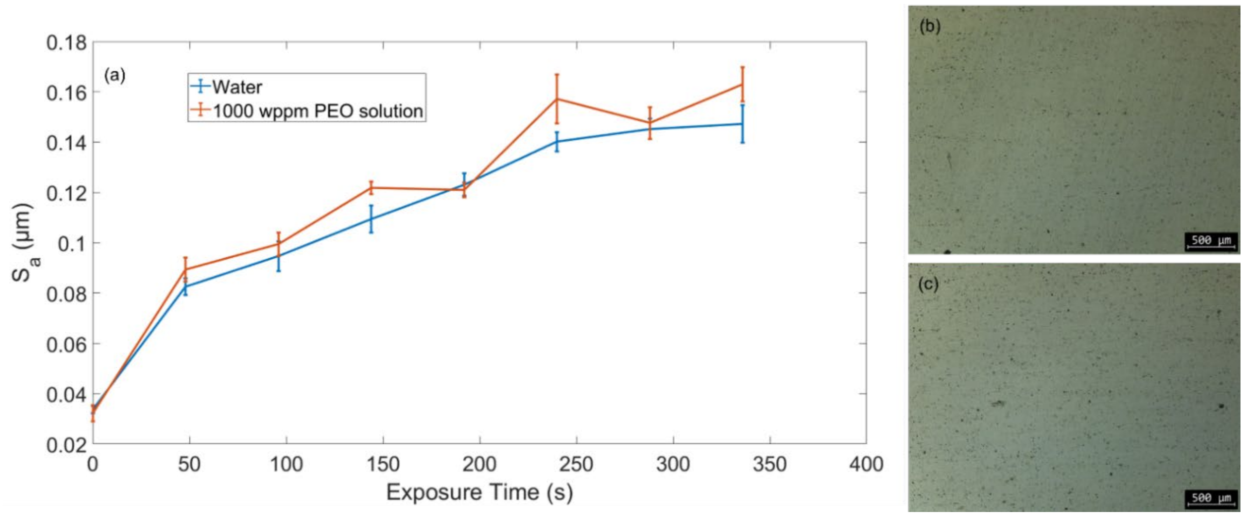

Fig. 6-7 Evolution of the arithmetic area average surface roughness (Sa) of ultrasonic cavitation treated Al 7075-T651 surface, and optical micrographs of the same surfaces processed for 240 s with b) water, and c) 1000 wppm aqueous PEO solution illustrating surface pitting due to cavitation impacts (black spots).

Through a pitting analysis of the surfaces obtained after exposing Al 7075-T651 samples to ultrasonic cavitation treatment for 240 s with water and 1000 wppm PEO solution, it was found that the areal coverage of pitting produced by the 1000 wppm PEO solution was ~ 27% more than in the surface produced by water alone. This indicates that greater surface plastic deformation is produced by the 1000 wppm aqueous PEO solution compared to water alone. The high-speed imaging and PVDF results indicate increased cavitation activity, which is confirmed by the higher areal coverage of plastically deformed pits obtained with the 1000 wppm aqueous PEO solution.

6.4 Summary

This chapter reported on the results of an experimental investigation of the effects of water-soluble PEO added to water on cavitation intensity characterized by mass loss, high speed imaging, and

PVDF sensing of cavitation cloud collapse events. It was shown that it is possible to enhance cavitation intensity in ultrasonic cavitation surface treatment by adding PEO of a specific concentration to water. The following are the key findings of the study:

1. A 1000 wppm PEO solution yields the greatest mass loss, and therefore cavitation intensity, in Al 1100-O at a standoff distance of 2 mm from the horn tip. This result confirms the existence of an aqueous PEO solution concentration at which cavitation activity is enhanced beyond the cavitation produced in water.
2. The cavitation cloud size, measured in terms of the average maximum cloud width, is larger with aqueous PEO solutions than with water, indicating that cavitation is enhanced by the addition of PEO to water. However, the cloud width trends do not completely explain the mass loss trends. The role of reduced surface tension in PEO aqueous solutions requires further investigation.
3. PVDF measurements show that the cumulative number of cavitation impact events are the greatest for the 1000 wppm PEO solution, thus confirming the mass loss trends.
4. The 1000 wppm PEO solution produces higher surface roughness than water during ultrasonic cavitation surface treatment of Al 7075-T651, thus confirming enhanced cavitation intensity. Analysis of surface pitting of the workpiece shows that the 1000 wppm PEO solution produces ~27 % greater areal surface pitting than water alone.

CHAPTER 7. FUTURE WORK AND CONCLUSIONS

This chapter summarizes the main conclusions of the thesis and recommends future areas of research for further investigation.

7.1 Main Conclusions

7.1.1 Effect of upstream organ pipe inner jet nozzle geometry on cavitation intensity in co-flow water cavitation peening

The chapter presented an experimental investigation of the possible enhancement of cavitation intensity in co-flow water cavitation peening of aluminum 7075-T651 alloy by utilizing an organ pipe inner nozzle. Organ pipes of different lengths corresponding to different Strouhal Numbers (*St*) were designed and used in extended mass loss and peening experiments, and the results were compared with those obtained for a standard unexcited nozzle. The main conclusions of the chapter are as follows:

1. The optimum Strouhal Number for the inner jet, which leads to enhancement of cavitation intensity in co-flow cavitation peening, was found to be 0.28, a number that is close to the optimum value proposed by Crow and Champagne [84] for highly turbulent air jets.
2. The optimum organ pipe inner nozzle yielded a 61% increase in the mass loss and a 66% increase in strip curvature relative to the unexcited nozzle, indicating enhancement in cavitation intensity.
3. High speed videography and impulse pressure measurements provided valuable insights into the cavitation cloud characteristics for the unexcited and optimum organ pipe nozzles. Power spectral density analyses of the processed image data showed that the power associated

with the optimum organ pipe nozzle is greater than the power associated with the unexcited nozzle. Analysis of impulse pressure measurements produced by cloud collapse events revealed that the enhanced intensity of the cavitating jets produced by the optimum organ pipe inner nozzle is due to the higher frequency of strong cavitation events.

4. Compressive residual stress generated by the optimum organ pipe nozzle is larger in magnitude at depths higher than 0.05 mm compared to the residual stress induced by the unexcited nozzle.

7.1.2 Effect of inner jet nozzle orifice taper on cavitation intensity in co-flow water cavitation peening

This chapter presented an experimental and numerical study of the effect of inner jet nozzle orifice taper on cavitation intensity in co-flow water cavitation peening of aluminum 7075-T651 alloy. Nozzles of converging, zero and diverging taper were tested using extended mass loss and peening experiments. The main conclusions of the study are as follows:

1. The mass loss tests on Al 7075-T651 show that the nozzle with converging taper generates the greatest cavitation intensity. The mass loss produced by the converging taper nozzle is greater than the mass loss produced by the nozzles with zero and diverging taper by 18% and 46%, respectively. Thus, there exists a strong trend in the cavitation intensity with area reduction or alternatively taper, as shown through a simple linear regression model.
2. The strip curvature tests on Al 7075-T651 confirm the enhanced cavitation intensity of the nozzle with converging taper. The arc height produced by the nozzle with converging taper was greater than the arc height produced by the nozzles with zero and diverging taper by 65% and 59%, respectively.

3. The impulse pressure measurements show that the frequency and magnitude of high intensity cavitation events is greater in the case of the nozzle with converging taper, which can explain the enhanced cavitation intensity.
4. Results from extended mass loss, strip curvature and impulse pressure measurements indicate the higher inner jet exit velocity may be responsible for the greater cavitation intensity produced by the converging taper nozzle.
5. The steady state RANS CFD simulations of the internal flow in the inner jet nozzles show that the area averaged exit velocities are the greatest for the nozzle variant with converging taper, which is likely responsible for greater shear in the co-flow field leading to greater cavitation intensity.

7.1.3 Effect of inner jet nozzle orifice length on cavitation intensity in co-flow water peening

An experimental of the effect of inner jet nozzle orifice length, characterized by the L_o/d ratio, was conducted using extended mass loss and strip curvature experiments. The following conclusions can be drawn from this study on the effect of L_o/d ratio on cavitation intensity in co-flow cavitation peening.

1. The mass loss produced by the L_o/d ratio of 2 is greater than the mass loss produced by nozzles with L_o/d ratios of 1, 5 and 10 indicating the enhanced cavitation intensity of the inner jet nozzle with L_o/d ratio of 2. This indicates the role of the inner jet nozzle orifice length on cavitation intensity in co-flow cavitation peening.
2. Strip curvature measurements confirm the enhanced cavitation intensity of the inner nozzle with L_o/d ratio of 2. The peak heights of the strip curvatures produced with the other inner

jet nozzles are lower than the peak strip arc height seen with the inner jet nozzle L_o/d ratio of 2.

7.1.4 *Effect of polyethylene oxide additives on cavitation intensity in ultrasonic peening*

This chapter reported on the results of an experimental investigation of the effects of water-soluble PEO added to water on cavitation intensity characterized by mass loss, high speed imaging, and PVDF sensing of cavitation cloud collapse events. It was shown that it is possible to enhance cavitation intensity in ultrasonic cavitation surface treatment by adding PEO of a specific concentration to water. The following are the key findings of the study:

1. A 1000 wppm PEO solution yields the greatest mass loss, and therefore cavitation intensity, in Al 1100-O at a standoff distance of 2 mm from the horn tip. This result confirms the existence of an aqueous PEO solution concentration at which cavitation activity is enhanced beyond the cavitation produced in water.
2. The cavitation cloud size, measured in terms of the average maximum cloud width, is larger with aqueous PEO solutions than with water, indicating that cavitation is enhanced by the addition of PEO to water. However, the cloud width trends do not completely explain the mass loss trends. The role of reduced surface tension in PEO aqueous solutions requires further investigation.
3. PVDF measurements show that the cumulative number of cavitation impact events are the greatest for the 1000 wppm PEO solution, thus confirming the mass loss trends.
4. The 1000 wppm PEO solution produces higher surface roughness than water during ultrasonic cavitation surface treatment of Al 7075-T651, thus confirming enhanced

cavitation intensity. Analysis of surface pitting of the workpiece shows that the 1000 wppm PEO solution produces ~27 % greater areal surface pitting than water alone.

7.2 Recommendations for Future Work

Some areas for future research are outlined below:

1. Further investigations of the effects of nozzle geometry, specifically the role of inner jet nozzle outlet geometry in co-flow water cavitation peening.

   The outlet shape of the inner jet nozzle may influence the cloud shedding parameters and the jet width, as shown by Soyama in submerged cavitation peening [79]. The inner jet width (the spread of the jet) and turbulent kinetic energy in the co-flow field are likely to be influenced by the outlet geometry of the inner jet nozzle in co-flow cavitation peening, which could potentially be engineered to achieve desirable cavitation intensity and cloud shedding parameters. An experimental and numerical investigation should be carried out to address this potential.

2. Multiphase-RANS and Large Eddy Simulation (LES) based Computational Fluid Dynamics (CFD) modeling of co-flow cavitation peening for the prediction of cloud parameters and faster evaluation of nozzle designs.

   Multi-phase RANS and LES and models may offer a mechanistic insight into the turbulent phenomenon of interest, which can lead to better process modeling and faster evaluation of the effect of co-flow nozzle designs on the cloud shedding frequency and other cloud parameters. Specifically, the effects of the inner jet nozzle design on cavitation cloud parameters can be better understood, thereby augmenting the experimental efforts. The

RANS and LES simulations should help direct process designers to the appropriate design spaces before significant experimental effort is undertaken.

3. A coupled Finite Element-CFD model for predicting residual stresses.

   A coupled Finite Element-CFD model for the prediction of the residual stresses generated by multiple cavitation bubble impacts may be realized with the coupling of the LES models with appropriate finite element analysis models employing suitable constitutive relations for the prediction of residual stresses. The models can give insights into the peening exposure time required and the cavitation intensity of the co-flow jets.

4. Evaluation of end effector robot assemblies for robotic co-flow water cavitation peening.

   The current state of the process utilizes a gantry system for scanning motions of the co-flow nozzle assembly that results in peening with 3 degrees of freedom. Hence the angular orientation of the co-flow nozzle with respect to the work piece surface is fixed. A robotic arm assembly capable of motion with more degrees of freedom with the co-flow jet as the end effector may prove to be useful for peening of large structural assemblies with curved surfaces. The feasibility of such a technique may be tested with experimentation at different inclinations of the co-flow nozzle assembly with respect to the testing surface for a preliminary analysis.

APPENDIX A1. MASS LOSS RESULTS

Mass Loss Data for the Unexcited and Organ Pipe Nozzles

Unexcited nozzle mass loss data

nSOD	Mass Loss (mg)	Standard Deviation (mg)	Number of Samples
40	35.93	1.15	3
45	42.16	0.68	3
50	50.00	1.45	3
55	24.36	0.85	3

5 mm organ pipe nozzle mass loss (Strouhal Number (*St*): 0.42)

nSOD	Mass Loss (mg)	Standard Deviation (mg)	Number of Samples
40	47.06	1.06	3
45	53.23	2.34	3
50	27.4	0.52	3

7.5 mm organ pipe nozzle mass loss data (Strouhal Number (*St*): 0.28)

nSOD	Mass Loss (mg)	Standard Deviation (mg)	Number of Samples
40	62.16	1.88	3
45	80.63	1.78	3
50	58.4	3.03	3

15 mm organ pipe nozzle mass loss data (Strouhal Number (*St*): 0.14)

nSOD	Mass Loss (mg)	Standard Deviation (mg)	Number of Samples
40	33.9	7.15	3
45	42.93	2.34	3
50	23.53	0.77	3

Maximum Mass Loss Data for Inner Jet Nozzles with Varying Taper

Converging taper nozzle mass loss data

Nozzle	nSOD	Mass Loss (mg)	Standard Deviation (mg)	Number of Samples
Converging taper-1	50	74.40	3.29	3
Converging taper-2	50	70.63	3.03	3
Converging taper-3	50	78.46	3.66	3

Zero taper nozzle mass loss data

Nozzle	nSOD	Mass Loss (mg)	Standard Deviation (mg)	Number of Samples
Zero taper-1	45	53.26	2.11	3
Zero taper-2	45	66.33	1.40	3
Zero taper-3	50	71.43	0.75	3

Diverging taper nozzle mass loss data

Nozzle	nSOD	Mass Loss (mg)	Standard Deviation (mg)	Number of Samples
Diverging taper-1	50	47.76	1.90	3
Diverging taper-2	50	64.86	1.46	3
Diverging taper-3	45	41.30	3.12	3

Mass Loss Data for Inner Jet Nozzles with Varying L_o/d Ratios

Mass loss data for L_o/d ratio of 1

nSOD	Mass Loss (mg)	Standard Deviation (mg)	Number of Samples
35	12.13	0.75	3
40	38.43	1.87	3
45	26.33	4.72	3
50	17.1	1.99	3

Mass loss data for L_o/d ratio of 2

nSOD	Mass Loss (mg)	Standard Deviation (mg)	Number of Samples
35	20.00	1.30	3
40	49.76	1.74	3
45	51.5	3.96	3
50	25.26	2.51	3

Mass loss data for L_o/d ratio of 5

nSOD	Mass Loss (mg)	Standard Deviation	Number of Samples
35	14.90	0.87	3
40	28.16	2.41	3
45	29.96	3.78	3
50	27.06	2.51	3

Mass loss data for L_o/d ratio of 10

nSOD	Mass Loss (mg)	Standard Deviation (mg)	Number of Samples
35	12.53	0.87	3
40	20.70	0.43	3
45	25.86	2.02	3
50	29.83	0.89	3

Mass Loss Data for Water and PEO Aqueous Solutions

Water

Standoff Distance (mm)	Mass Loss (mg)	Standard Deviation (mg)	Number of Samples
2	7.9	1.9	4
5	1.83	0.23	3
8	1.1	0.5	3

1000 wppm PEO aqueous solution

Standoff Distance (mm)	Mass Loss (mg)	Standard Deviation (mg)	Number of Samples
2	13.4	2.7	3
5	2.3	0.20	3
8	0.6	0.3	3

16000 wppm PEO aqueous solution

Standoff Distance (mm)	Mass Loss (mg)	Standard Deviation (mg)	Number of Samples
2	5.9	0.3	3
5	3.3	0.30	3
8	1.3	0.2	3

APPENDIX A2. CFD MODELING DETAILS

Details of Turbulence Model

Turbulence model	RNG-k-ε
Wall Functions	Enhanced wall functions
Turbulence intensity	5 % (default)
Turbulent viscosity ratio	10 (default)
C_{μ}	0.0845 (default)
$C_{\varepsilon 1}$	1.42 (default)
$C_{\varepsilon 2}$	1.68 (default)

Mesh Description

Meshing was done using the ANSYS^{TM} Meshing tool. The size of elements (quadrilateral linear order) for the converged mesh close to wall was ~2 µm. The size of elements far away from the nozzle wall was ~10 µm. The mesh can be seen in Fig A2-1. The element size parameter for the overall mesh was 20 µm. The refinement parameter applied to the wall of the nozzle orifice was 3. The edge sizing parameter along the wall was 10 µm. These parameters allow for reproducibility of the mesh. The mesh used for computation had ~500000 elements.

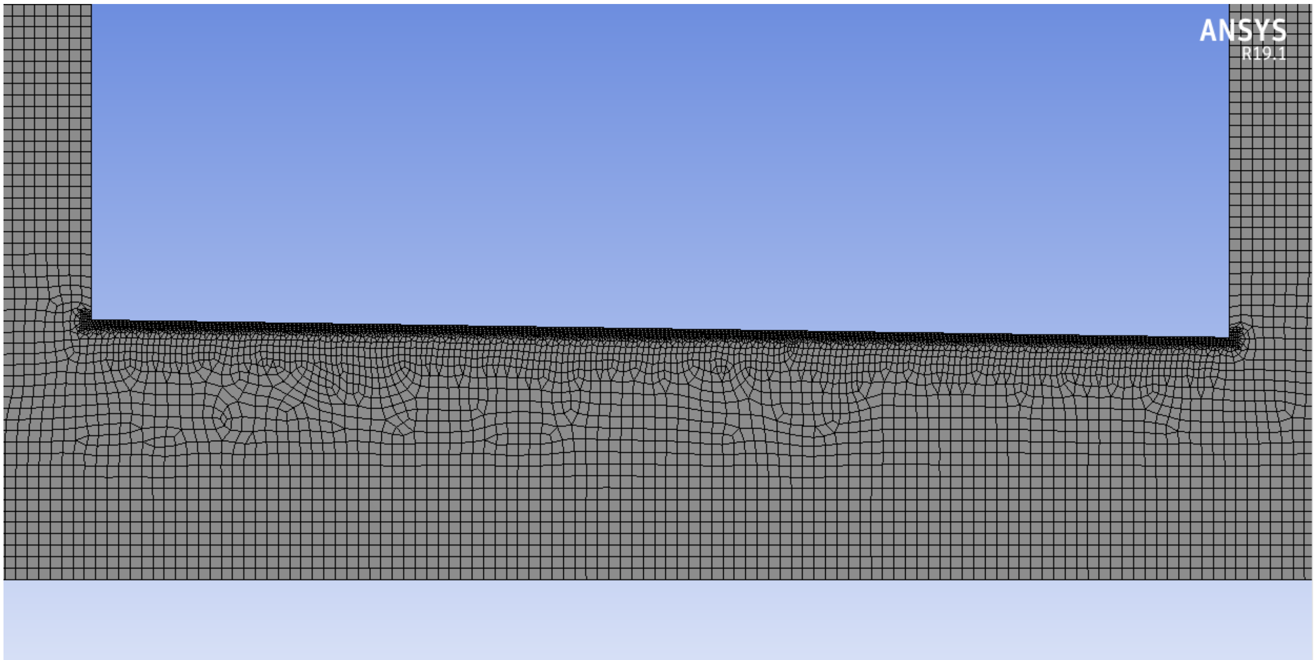

Fig. A2-1 Example of mesh used for simulation.

Mesh Settings

Pictures from the ANSYS Meshing tool are shown to aid reproducibility.

Table A2-1 Overall mesh parameters

Object Name	*Mesh*
State	Solved
Display	
Display Style	Body Color
Defaults	
Physics Preference	CFD
Solver Preference	Fluent
Element Order	Linear
Element Size	2.e-005 m
Export Format	Standard
Export Preview Surface Mesh	No
Sizing	
Use Adaptive Sizing	No
Growth Rate	Default (1.2)
Mesh Defeaturing	Yes
Defeature Size	Default (1.e-007 m)
Capture Curvature	Yes
Curvature Min Size	Default (2.e-007 m)
Curvature Normal Angle	Default (18.0°)
Capture Proximity	No

Bounding Box Diagonal	2.6926e-002 m
Average Surface Area	2.1993e-004 m²
Minimum Edge Length	2.0002e-003 m
Quality	
Check Mesh Quality	Yes, Errors
Target Skewness	Default (0.900000)
Smoothing	Medium
Mesh Metric	Orthogonal Quality
Min	0.44203
Max	1.
Average	0.99957
Standard Deviation	6.0793e-003
Inflation	
Use Automatic Inflation	None
Inflation Option	Smooth Transition
Transition Ratio	0.272
Maximum Layers	2
Growth Rate	1.2
Inflation Algorithm	Pre
View Advanced Options	No
Assembly Meshing	
Method	None
Advanced	
Number of CPUs for Parallel Part Meshing	Program Controlled
Straight Sided Elements	
Rigid Body Behavior	Dimensionally Reduced
Triangle Surface Mesher	Program Controlled
Topology Checking	Yes
Use Sheet Thickness for Pinch	No
Pinch Tolerance	Default (1.8e-007 m)
Generate Pinch on Refresh	No
Sheet Loop Removal	No
Statistics	
Nodes	556832
Elements	554461

Definition of Edges

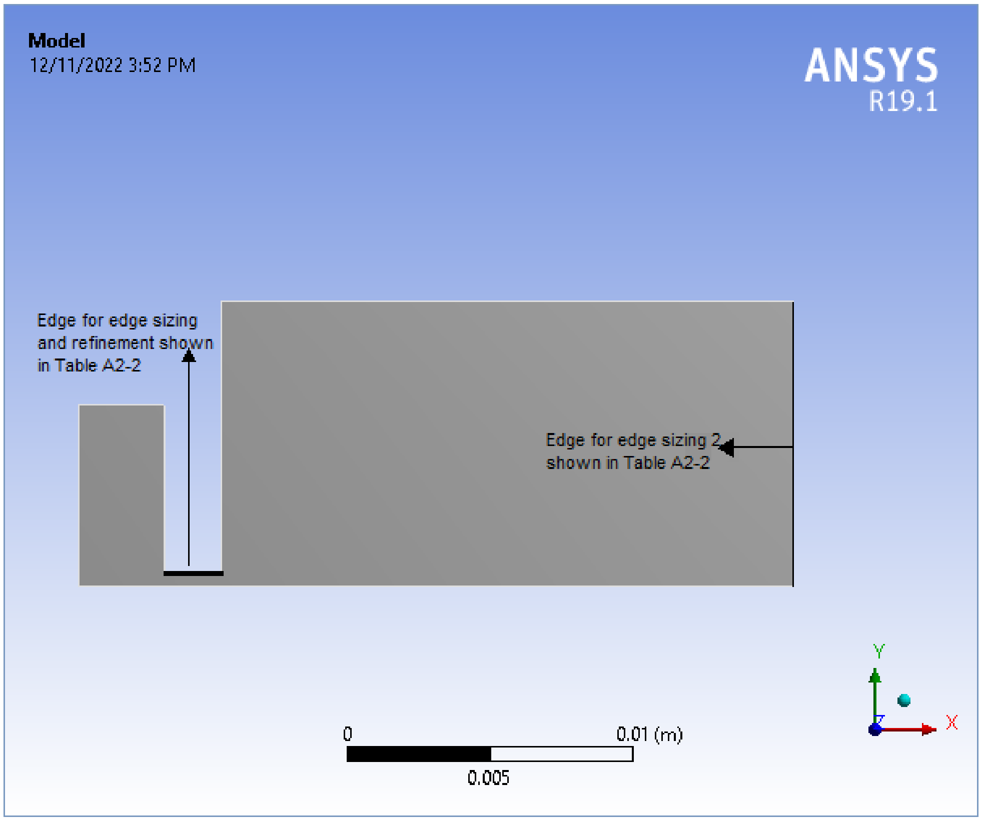

Fig. A2-2 Description of edge sizing and refinement.

Table A2-2 Edge sizing parameters

Object Name	*Refinement*	*Edge Sizing*	*Edge Sizing 2*
State	Fully Defined		
Scope			
Scoping Method	Geometry Selection		
Geometry	1 Edge		
Definition			
Suppressed	No		
Refinement	3		
Type		Element Size	
Element Size		1.e-005 m	0.1 m
Advanced			
Behavior		Soft	
Growth Rate		Default (1.2)	
Capture Curvature		No	
Capture Proximity		No	
Bias Type		No Bias	

Description of Wall Functions

Enhanced wall functions were used. Since the y^+ values, shown Fig. A2-2, obtained for the mesh were fairly high and not enough to resolve the viscous sublayer, enhanced wall functions were used. This mesh is termed a wall-function mesh in ANSYS. The enhanced wall functions allow for improved accuracy in such situations.

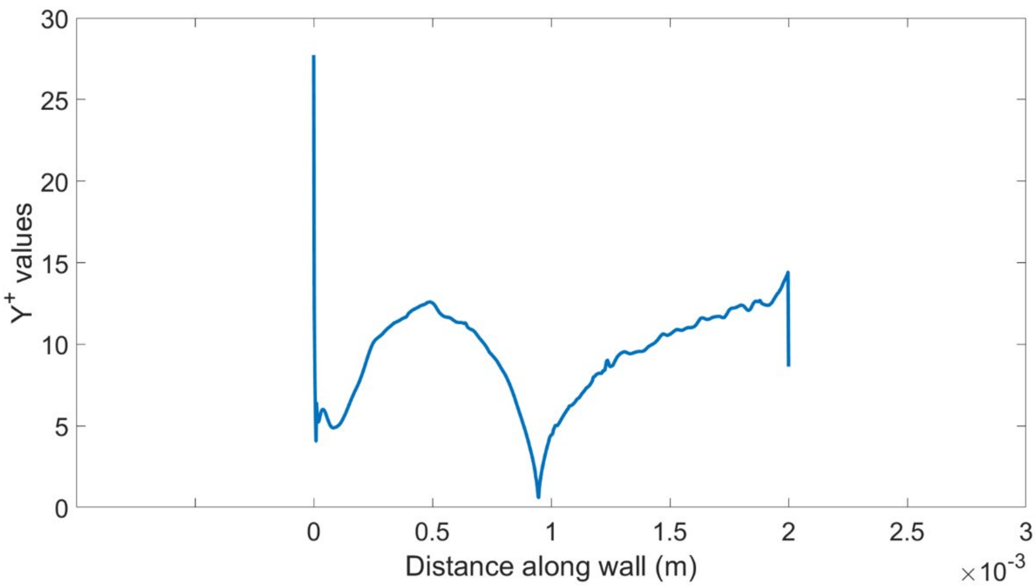

Fig. A2-3 Plot of y^+ values along the wall used for determining appropriate mesh refinement.

Solver Settings

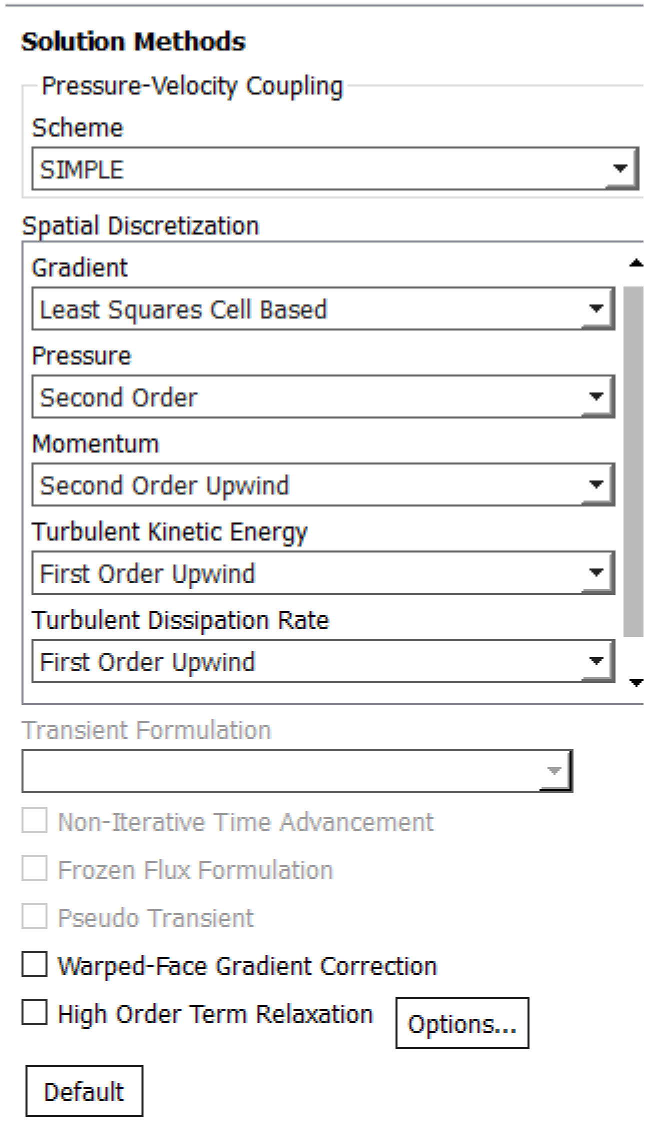

Fig. A2-4 Solver settings used.

REFERENCES

[1] Schijve, J. "Fatigue of aircraft materials and structures." International Journal of Fatigue 16.1 (1994): 21-32. https://doi.org/10.1016/0142-1123(94)90442-1

[2] Schijve, J. "Fatigue damage in aircraft structures, not wanted, but tolerated?" International Journal of Fatigue 31.6 (2009): 998-1011. https://doi.org/10.1016/j.ijfatigue.2008.05.016

[3] Waterhouse, R. "The Effect of Surface Treatments on the Fretting Wear of an Aluminium Alloy (RR58)/Steel (BS 970 080 M40) Couple." Surface Engineering 1990 (1990): 325-334. https://doi.org/10.1007/978-94-009-0773-7_33

[4] Wanhill, R., Byrnes, R., and Smith, C. "Stress corrosion cracking (SCC) in aerospace vehicles." Stress Corrosion Cracking (2011): 608-650. https://doi.org/10.1533/9780857093769.4.608

[5] Rodopoulos, C., Curtis, S., De Los Rios, E., and SolisRomero, J. "Optimisation of the fatigue resistance of 2024-T351 aluminium alloys by controlled shot peening—methodology, results and analysis." International Journal of Fatigue 26.8 (2004): 849-856. https://doi.org/10.1016/j.ijfatigue.2004.01.003

[6] Gupta, R., Pant, B., Kain, V., Kaul, R., and Bindra, K. "Laser shock peening and its applications: a review." Lasers in Manufacturing and Materials Processing 6.4 (2019): 424-463. https://doi.org/10.1007/s40516-019-00098-8

[7] Wong, C., Hartawan, A., and Teo, W. "Deep cold rolling of features on aero-engine components." Procedia CIRP 13 (2014): 350-354. https://doi.org/10.1016/j.procir.2014.04.059

[8] Zhang, T., Bugtai, N., and Marinescu, I. "Burnishing of aerospace alloy: a theoretical–experimental approach." Journal of Manufacturing Systems 37 (2015): 472-478. https://doi.org/10.1016/j.jmsy.2014.11.004

[9] Chillman, A., Ramulu, M. and Hashish, M. "Waterjet peening and surface preparation at 600 MPa: A preliminary experimental study." Journal of Fluids Engineering. 129.4 (2007): 485-490. https://doi.org/10.1115/1.2436580

[10] Nam, Y., Jeong, Y., Shin, B., and Byun, J. "Enhancing surface layer properties of an aircraft aluminum alloy by shot peening using response surface methodology." Materials & Design 83 (2015): 566-576. https://doi.org/10.1016/j.matdes.2015.06.065

[11] Vázquez, J., Navarro, C. and Domínguez, J. "Experimental results in fretting fatigue with shot and laser peened Al 7075-T651 specimens." International Journal of Fatigue 40 (2012): 143-153. https://doi.org/10.1016/j.ijfatigue.2011.12.014

[12] Al-Obaid, Y. F. "The effect of shot peening on stress corrosion cracking behaviour of 2205-duplex stainless steel." Engineering Fracture Mechanics 51, no. 1 (1995): 19-25. https://doi.org/10.1016/0013-7944(94)00213-2

[13] Suresh, S. Fatigue of Materials. Cambridge University Press, 1998. https://doi.org/10.1017/CBO9780511806575

[14] Zhang, X., Liu, D., "Effect of shot peening on fretting fatigue of Ti811 alloy at elevated temperature.", International Journal of Fatigue, 31 (2009) 889-893. http://dx.doi.org/10.1016/j.ijfatigue.2008.10.004

[15] Cunha, A., Giacomelli, R. O., Kaufman, J., Brajer, J., and Pereira, T. "An Overview on Laser Shock Peening Process: From Science to Industrial Applications." SBFoton International Optics and Photonics Conference (SBFoton IOPC) IEEE (2021): 1-6. https://doi.org/10.1109/SBFotonIOPC50774.2021.9461929

[16] Salahshoor, M., and Guo, Y. "Surface integrity of biodegradable Magnesium–Calcium orthopedic implant by burnishing." Journal of the Mechanical Behavior of Biomedical Materials 4.8 (2011): 1888-1904. https://doi.org/10.1016/j.jmbbm.2011.06.006

[17] Soyama, H., Kenichi S., and Masumi S. "Improvement of fatigue strength of aluminum alloy by cavitation shotless peening." Journal of Engineering Materials and Technology 124.2 (2002): 135-139.

[18] Bai, F., Saalbach, K., Long, Y., Twiefel, J., and Wallaschek, J. "Capability evaluation of ultrasonic cavitation peening at different standoff distances." Ultrasonics 84 (2018): 38-44. https://doi.org/10.1016/j.ultras.2017.10.013

[19] Soyama, H. "Key factors and applications of cavitation peening." International Journal of Peening Science and Technology 1.1 (2017): 3-60.

[20] Soyama, H., Kikuchi, T., Nishikawa, M., and Takakuwa, O. "Introduction of compressive residual stress into stainless steel by employing a cavitating jet in air. " Surface and Coatings Technology, 205(10) (2011): 3167-3174. https://doi.org/10.1016/j.surfcoat.2010.11.031

[21] Toh, C. "The use of ultrasonic cavitation peening to improve micro-burr-free surfaces. " The International Journal of Advanced Manufacturing Technology, 31(7) (2007): 688-693. https://doi.org/10.1007/s00170-005-0249-9

[22] Vijay, M., Zou, C., Hu, S., Remisz, J., and Tavoularis, S. "A study of the practicality of cavitating water jets." Jet Cutting Technology 13 (1992): 75-99. https://doi.org/10.1007/978-94-011-2678-6_6

[23] Ashworth, V., and Procter, R. "Cavitation damage in dilute polymer solutions." Nature 258.5530 (1975): 64-66. https://doi.org/10.1038/258064a0

[24] Shima, A., Tsujino, T., Nanjo, H., and Miura, N. "Cavitation damage in polymer aqueous solutions." Journal of Fluids Engineering 107(1) (1985): 134-138. https://doi.org/10.1115/1.3242431

[25] Nanjo, H., Shima, A., and Tsujino, T. "Formation of damage pits by cavitation in a polymer solution." Nature 320.6062 (1986): 516-517. https://doi.org/10.1038/320516a0

[26] Rodopoulos, C., Romero, J., Curtis, S., De los Rios, E., and Peyre, P. " Effect of controlled shot peening and laser shock peening on the fatigue performance of 2024-T351 aluminum alloy." Journal of Materials Engineering and Performance, 12(4) (2003): 414-419. https://doi.org/10.1361/105994903770342944

[27] Adu-Gyamfi, S., Ren, X., Larson, E., Ren, Y., and Tong, Z. "The effects of laser shock peening scanning patterns on residual stress distribution and fatigue life of AA2024 aluminium alloy. " Optics & Laser Technology, 108 (2018): 177-185. https://doi.org/10.1016/j.optlastec.2018.06.036

[28] Wagner, L., Mhaede, M., Wollmann, M., Altenberger, I., and Sano, Y. "Surface layer properties and fatigue behavior in Al 7075-T73 and Ti-6Al-4V: Comparing results after laser peening; shot peening and ball-burnishing. " International Journal of Structural Integrity Vol 2 No 2 (2011): 185-199. https://doi.org/10.1108/17579861111135923

[29] Benedetti, M., Bortolamedi, T., Fontanari, V., and Frendo, F. "Bending fatigue behaviour of differently shot peened Al 6082 T5 alloy." International Journal of Fatigue, 26, no. 8 (2004): 889-897. https://doi.org/10.1016/j.ijfatigue.2003.12.003

[30] Martín, V., Vázquez, J., Navarro, C., & Domínguez, J. " Effect of shot peening residual stresses and surface roughness on fretting fatigue strength of Al 7075-T651." Tribology International, 142 (2020): 106004. https://doi.org/10.1016/j.triboint.2019.106004

[31] Bao, L., Li, K., Zheng, J., Zhang, Y., Zhan, K., Yang, Z., Zhao, B., and Ji, V. " Surface characteristics and stress corrosion behavior of AA 7075-T6 aluminum alloys after different shot peening processes. “Surface and Coatings Technology, 440 (2022): 128481. https://doi.org/10.1016/j.surfcoat.2022.128481

[32] Wagner, L., and Luetjering, G. "Influence of shot peening on the fatigue behavior of titanium alloys." International Conference on Shot Peening, Vol. 1 (1981): 453-460.

[33] Namjoshi, S. A., Jain, V. K., & Mall, S. "Effects of shot-peening on fretting-fatigue behavior of Ti-6Al-4V." Journal of Engineering Materials and Technology, 124(2) (2002)., 222-228. https://doi.org/10.1115/1.1448323

[34] Tekeli, S. " Enhancement of fatigue strength of SAE 9245 steel by shot peening." Materials Letters, 57(3) (2002): 604-608. https://doi.org/10.1016/S0167-577X(02)00838-8

[35] Mutoh, Y., Satoh, T., and Tsunoda, E. Improving fretting fatigue strength at elevated temperatures by shot peening in steam turbine steel. In Standardization of Fretting Fatigue Test Methods and Equipment. ASTM International, 1992. https://doi.org/10.1520/STP25835S

[36] Mlikota, M., Schmauder, S., Dogahe, K., and Božić, Ž. "Influence of local residual stresses on fatigue crack initiation." Procedia Structural Integrity, 31 (2021). 3-7. https://doi.org/10.1016/j.prostr.2021.03.002

[37] Meguid, S., Shagal, G., Stranart, J and Daly, J. "Three-dimensional dynamic finite element analysis of shot-peening induced residual stresses." Finite Elements in Analysis and Design, 31 no. 3 (1999): 179-191. https://doi.org/10.1016/S0168-874X(98)00057-2

[38] Bagherifard, S., Ghelichi, R., and Guagliano, M. " On the shot peening surface coverage and its assessment by means of finite element simulation: A critical review and some original developments. " Applied Surface Science, 259 (2012): 186-194. https://doi.org/10.1016/j.apsusc.2012.07.017

[39] Schwarzer, J., Schulze, V., and Vöhringer, O. " Finite element simulation of shot peening–a method to evaluate the influence of peening parameters on surface characteristics." Shot Peening (2003):505-515. https://doi.org/10.1002/3527606580.ch65

[40] Xing, Y. M., and J. Lu. "An experimental study of residual stress induced by ultrasonic shot peening." Journal of Materials Processing Technology 152, no. 1 (2004): 56-61. https://doi.org/10.1016/j.jmatprotec.2004.02.057

[41] Bleicher, F, Lechner, C., Habersohn, C., and Kozeschnik, E., Adjassoho, B., and Kaminski, H. "Mechanism of surface modification using machine hammer peening technology." CIRP Annals 61, no. 1 (2012): 375-378. https://doi.org/10.1016/j.cirp.2012.03.139

[42] Abushgair, K. "Experimental Studies the Effect of Flap Peening Process on Aluminum Alloys." Jordan Journal of Mechanical and Industrial Engineering, 11, no. 3 (2017): 173-180.

[43] Fathallah, R., Laamouri, A., Sidhom, H., and Braham, C. "High cycle fatigue behavior prediction of shot-peened parts. " International Journal of Fatigue, 26(10) (2004): 1053-1067.

[44] Gao, Y. " Influence of shot peening on tension–tension fatigue property of two high strength Ti alloys. " Surface engineering, 22(4) (2006): 299-303. https://doi.org/10.1179/174329406X122865

[45] Peyre, P., and Fabbro. R. "Laser shock processing: a review of the physics and applications." Optical and Quantum Electronics 27, no. 12 (1995): 1213-1229. https://doi.org/10.1007/BF00326477

[46] Ghahramani, M., Khalilzadeh, J., & Mahmoud, A. " Investigation of the effect of adsorbent layer on the laser shock process of Ti-43Al-5 V-4Nb. " Journal of Optics, 51(2022): 1-7. https://doi.org/10.1007/s12596-022-00889-x

[47] Chahardehi, A., Brennan, F., and Steuwer, A. "The effect of residual stresses arising from laser shock peening on fatigue crack growth. " Engineering Fracture Mechanics, 77(11) (2010): 2033-2039.

[48] Clauer, A., Holbrook, J., and Fairand, B. Effects of laser induced shock waves on metals. Shock waves and high-strain-rate phenomena in metals, Springer,1981. https://doi.org/10.1007/978-1-4613-3219-0_38

[49] Wang, J., Zhang, Y., Chen, J., Zhou, J., Ge, M., Lu, Y., and Li, X.. "Effects of laser shock peening on stress corrosion behavior of 7075 aluminum alloy laser welded joints." Materials Science and Engineering: A, 647 (2015)., 7-14. https://doi.org/10.1016/j.msea.2015.08.084

[50] Ramulu, M., Kunaporn, S., Jenkins, M., Hashish, M., and Hopkins, J. "Fatigue performance of high-pressure waterjet-peened aluminum alloy." Journal of Pressure Vessel Technology, 124(1) (2002): 118-123. https://doi.org/10.1115/1.1398553

[51] Kunaporn, S., Ramulu, M., Jenkins, M. G., and Hashish, M. "Residual stress induced by waterjet peening: A finite element analysis." Journal of Pressure Vessel Technology, 126(3) (2004): 333-340. https://doi.org/10.1115/1.1767175

[52] Beghini, M., Bertini, L., Monelli, B., Santus, C., and Bandini, M. "Experimental parameter sensitivity analysis of residual stresses induced by deep rolling on 7075-T6 aluminium alloy." Surface and Coatings Technology, 254 (2014): 175-186. https://doi.org/10.1016/j.surfcoat.2014.06.008

[53] Rodríguez, A., de Lacalle, L., Celaya, A., Lamikiz, A., and Albizuri, J. "Surface improvement of shafts by the deep ball-burnishing technique." Surface and Coatings Technology, 206(11-12) (2012): 2817-2824. https://doi.org/10.1016/j.surfcoat.2011.11.045

[54] Lichtman, J., Kallas, D., Chatten, C., and Cochran, E. "Study of Corrosion and Cavitation-Erosion Damage." Transactions of the American Society of Mechanical Engineers, 80(6) (1958): 1325-1339. https://doi.org/10.1115/1.4012698

[55] Lichtarowicz, A. Cavitating jet apparatus for cavitation erosion testing. Erosion: Prevention and Useful Applications. ASTM International, 1979 https://doi.org/10.1520/STP35816S

[56] Endo, K., Okada, T., and Baba, Y. "Fundamental studies on cavitation erosion." Bulletin of JSME, 12(52) (1969): 729-737.

[57] Trevena, D. "Cavitation and the generation of tension in liquids." Journal of Physics D: Applied Physics, 17(11) (1984): 2139. https://doi.org/10.1088/0022-3727/17/11/003

[58] Sreedhar, B., Albert, S., and Pandit, A. " Cavitation damage: Theory and measurements–A review. " Wear, 372 (2017): 177-196. https://doi.org/10.1016/j.wear.2016.12.009

[59] Choi, J., Jayaprakash, A, Kapahi, A., Hsiao, C., and Chahine, G. "Relationship between space and time characteristics of cavitation impact pressures and resulting pits in materials. " Journal of Materials Science, 49(8) (2014): 3034-3051. https://doi.org/10.1007/s10853-013-8002-5

[60] Karimi, A., & Martin, J. "Cavitation erosion of materials." International Metals Reviews, 31(1) (1986): 1-26. https://doi.org/10.1179/imtr.1986.31.1.1

[61] Richman, R., & McNaughton, W. "Correlation of cavitation erosion behavior with mechanical properties of metals." Wear, 140(1) (1990), 63-82. https://doi.org/10.1016/0043-1648(90)90122-Q

[62] Krause, H., and Mathias, M. "Investigation of cavitation erosion using X-ray residual stress analysis. " Wear, 119(3) (1987): 343-352. https://doi.org/10.1016/0043-1648(87)90040-8

[63] Carnelli, D., Karimi, A., and Franc, J. "Application of spherical nanoindentation to determine the pressure of cavitation impacts from pitting tests." Journal of Materials Research, 27(1) (2012): 91-99.

[64] Marcon, A., Melkote, S., Yoda, M., and Sanders, D. " Analysis of co-flow water cavitation peening of Al7075-T651 alloy using high-speed imaging and surface pitting tests. " Materials Performance and Characterization, 7(5) (2018): 1018-1040. https://doi.org/10.1557/jmr.2011.259

[65] Marcon, A. Water cavitation peening for aerospace materials, Doctoral Dissertation, Georgia Institute of Technology, 2017.

[66] Singh, S., Choi, J. and Chahine, G. "Characterization of cavitation fields from measured pressure signals of cavitating jets and ultrasonic horns." Journal of Fluids Engineering 135.9 (2013): 091302. https://doi.org/10.1115/1.4024263

[67] Soyama, H., Sekine, Y., and Saito, K. "Evaluation of the enhanced cavitation impact energy using a PVDF transducer with an acrylic resin backing." Measurement 44(7) (2011): 1279-1283. https://doi.org/10.1016/j.measurement.2011.03.027

[68] Wu, P., Wang, X., Lin, W., and Bai, L. "Acoustic characterization of cavitation intensity: A review." Ultrasonics Sonochemistry 82(2022): 105878. https://doi.org/10.1016/j.ultsonch.2021.105878

[69] Song, J., Johansen, K., and Prentice, P. “An analysis of the acoustic cavitation noise spectrum: The role of periodic shock waves.” The Journal of the Acoustical Society of America, 140(4) (2016), 2494-2505. https://doi.org/10.1121/1.4964633

[70] Soyama, H. "Improvement in fatigue strength of silicon manganese steel SUP7 by using a cavitating jet. " JSME International Journal Series A Solid Mechanics and Material Engineering 43(2) (2000): 173-178. https://doi.org/10.1299/jsmea.43.173

[71] Soyama, H., Park, J. and Saka, M. "Use of cavitating jet for introducing compressive residual stress." Journal of Manufacturing Science and Engineering 122.1 (2000): 83-89. https://doi.org/10.1115/1.538911

[72] Gao, Y., Wu, B., Liu, Z., Zhou, Y., Shen, N., and Ding, H. "Ultrasonic cavitation peening of stainless steel and nickel alloy. " Journal of Manufacturing Science and Engineering, 136(1) (2014): 014502-08. https://doi.org/10.1115/1.4025756

[73] Soyama, H., Yamauchi, Y., Adachi, Y., Sato, K., Shindo, T., and Oba, R. "High-speed observations of the cavitation cloud around a high-speed submerged water jet." JSME International Journal Series B Fluids and Thermal Engineering 38(2) (1995): 245-251. https://doi.org/10.1299/jsmeb.38.245

[74] Yamauchi, Y., Soyama, H., Adachi, Y., Sato, K., Shindo, T., Oba, R., Oshima, R., and Yamabe, M. "Suitable region of high-speed submerged water jets for cutting and peening."

JSME International Journal Series B Fluids and Thermal Engineering 38(1) (1995): 31-38. https://doi.org/10.1299/jsmeb.38.31

[75] Soyama, H. "Improvement of fatigue strength by using cavitating jets in air and water." Journal of Materials Science, 42(16) (2007): 6638-6641. https://doi.org/10.1007/s10853-007-1535-8

[76] Marcon, A., Melkote, S. and Yoda, M. "Effect of nozzle size scaling in co-flow water cavitation jet peening." Journal of Manufacturing Processes, 31(2018)., 372-381. https://doi.org/10.1016/j.jmapro.2017.12.002

[77] Qin, M., D. Y. Ju, and R. Oba. "Improvement on the process capability of water cavitation peening by aeration." Surface and coatings technology 200.18-19 (2006): 5364-5369. https://doi.org/10.1016/j.surfcoat.2005.06.024

[78] Peng, C., Tian, S., Li, G., & Wei, M. "Enhancement of cavitation intensity and erosion ability of submerged cavitation jet by adding micro-particles." Ocean Engineering 209 (2020): 107516. https://doi.org/10.1016/j.oceaneng.2020.107516

[79] Soyama, H. "Enhancing the aggressive intensity of a cavitating jet by introducing a cavitator and a guide pipe." Journal of Fluid Science and Technology 9.1 (2014): JFST0001-JFST0001. https://doi.org/10.1115/1.4004905

[80] Soyama, H. "Enhancing the aggressive intensity of a cavitating jet by means of the nozzle outlet geometry." Journal of Fluids Engineering 133.10 (2011): 101301. https://doi.org/10.1115/1.4004905

[81] White, F. Fluid Mechanics. WCB/McGraw-Hill, 1999

[82] Johnson Jr, V., Chahine, G., Lindenmuth, W., Conn, A., Frederick, G., and Giacchino Jr, G. "Cavitating and structured jets for mechanical bits to increase drilling rate—Part I: Theory and concepts." Journal of Energy Resources Technology 106.2 (1984): 282-288. https://doi.org/10.1115/1.3231053

[83] Johnson Jr, V., Chahine, G., Lindenmuth, W., Conn, A., Frederick, G., and Giacchino Jr, G. "Cavitating and structured jets for mechanical bits to increase drilling rate. Part II: experimental results." Journal of Energy Resources Technology 106.2 (1984):289-294. https://doi.org/10.1115/1.3231054

[84] Crow, S., and Champagne, F. "Orderly structure in jet turbulence." Journal of Fluid Mechanics 48.3 (1971): 547-591. https://doi.org/10.1017/s0022112071001745

[85] Macián, V., Payri, R., Margot, X., and Salvador, F. "A CFD analysis of the influence of diesel nozzle geometry on the inception of cavitation." Atomization and Sprays 13.5&6 (2003): 579-604. https://doi.org/10.1615/atomizspr.v13.i56.80

[86] Payri, F., Bermudez, V., Payri, R., and Salvador, F. "The influence of cavitation on the internal flow and the spray characteristics in diesel injection nozzles." Fuel 83.4-5 (2004): 419-431. https://doi.org/10.1016/j.fuel.2003.09.010

[87] He, Z., Guo, G., Tao, X., Zhong, W., Leng, X., Wang, Q "Study of the effect of nozzle hole shape on internal flow and spray characteristics" International Communications in Heat and Mass Transfer 71 (2016): 1-8. https://doi.org/10.1016/j.icheatmasstransfer.2015.12.002

[88] Soyama, H. "Effect of nozzle geometry on a standard cavitation erosion test using a cavitating jet." Wear 297.1-2 (2013): 895-902. https://doi.org/10.1016/j.wear.2012.11.008

[89] Begenir, A., Tafreshi, H., & Pourdeyhimi, B. "Effect of nozzle geometry on hydroentangling water jets: experimental observations. " Textile Research Journal, 74(2) (2004): 178-184. https://doi.org/10.1177/004051750407400

[90] Shimizu, M., Arai, M. and Hiroyasu, H., "Measurements of breakup length in high-speed jet." Bulletin of JSME 27.230 (1984): 1709-1715. https://doi.org/10.1299/jsme1958.27.1709

[91] Tamaki, N., Shimizu, M., Nishida, K., and Hiroyasu, H. "Effects of cavitation and internal flow on atomization of a liquid jet." Atomization and sprays 8.2 (1998): 179-197. https://doi.org/10.1615/atomizspr.v8.i2.30

[92] Lefebvre, A., and McDonell V. Atomization and sprays. CRC press, 2017. https://doi.org/10.1201/9781315120911

[93] Hoyt, J. "Effect of polymer additives on jet cavitation." Journal of Fluids Engineering 98 (1976): 106-111. https://doi.org/10.1115/1.3448157

[94] Chahine, G., and Fruman, D. "Dilute polymer solution effects on bubble growth and collapse" Physics of Fluids 22(7) (1979): 1406-1407. https://doi.org/10.1063/1.862754

[95] Brujan, E., Al-Hussany, A., Williams, R., and Williams, P. "Cavitation erosion in polymer aqueous solutions." Wear 264.11-12 (2008): 1035-1042. https://doi.org/10.1016/j.wear.2007.08.007

[96] Gilányi, T., Varga, I., Gilányi, M., & Mészáros, R. "Adsorption of poly (ethylene oxide) at the air/water interface: A dynamic and static surface tension study." Journal of colloid and interface science, 301(2) (2006), 428-435. https://doi.org/10.1016/j.jcis.2006.05.034

[97] Iwai, Y., and Shengcai L. "Cavitation erosion in waters having different surface tensions." Wear 254, no. 1-2 (2003): 1-9. https://doi.org/10.1016/S0043-1648(02)00305-8

[98] Summers, D. Waterjetting Technology. CRC Press, 2003. https://doi.org/10.1201/9781482294828

[99] Marcon, A., Melkote, S., Castle, J., Sanders, D., and Yoda, M. "Effect of jet velocity in co-flow water cavitation jet peening." Wear. 360 (2016): 38-50. https://doi.org/10.1016/j.wear.2016.03.027

[100] Franc, J., and Michel, J. Fundamentals of Cavitation. Springer Science & Business Media, 2006.

[101] Gere, J., and Goodno, B. Mechanics of Materials. Cengage Learning, 2017.

[102] Deng, L., Kang, Y., Ding, X., Wang, X., and Fang, Z. "An experimental investigation on the pressure characteristics of high-speed self-resonating pulsed waterjets influenced by feeding pipe diameter." Journal of Mechanical Science and Technology 30.11 (2016): 4997-5007. https://doi.org/10.1007/s12206-016-1019-3

[103] "Residual Stress Measurement by X-ray Diffraction." HS-784 SAE. 2003.

[104] Prevéy, P. "Current applications of X-ray diffraction residual stress measurement." Developments in Materials Characterization Technologies (1996): 103-110.

[105] Soyama, H. "High-speed observation of a cavitating jet in air." Journal of Fluids Engineering 127.6 (2005): 1095-1101. https://doi.org/10.1115/1.2060737

[106] Soyama, H., Park, J., and Saka, M. "Use of cavitating jet for introducing compressive residual stress." Journal of Manufacturing Science and Engineering 122, no. 1 (2000): 83-89. https://doi.org/10.1115/1.538911

[107] Benedetti, M., Fontanari, V., Scardi, P., Ricardo, C., and Bandini, M. "Reverse bending fatigue of shot peened 7075-T651 aluminium alloy: The role of residual stress relaxation." International Journal of Fatigue 31.8-9 (2009): 1225-1236. https://doi.org/10.1016/j.ijfatigue.2008.11.017

[108] Yoshimura, T., Nishijima, N., Hashimoto, D., and Ijiri, M. "Sonoluminescence from ultra-high temperature and pressure cavitation produced by a narrow water jet." Heliyon, 7(8) (2021), e07767.

[109] Auret, J., Damm, O., Wright, G., and Robinson, F. "Cavitation erosion of copper and aluminium in water at elevated temperature." Tribology international 26, no. 6 (1993): 421-429. https://doi.org/10.1016/0301-679X(93)90082-C

[110] Miao, H., Demers, D., Larose, S., Perron, C., and Lévesque, M. "Experimental study of shot peening and stress peen forming." Journal of Materials Processing Technology, 210(15) (2010) 2089-2102. https://doi.org/10.1016/j.jmatprotec.2010.07.016

[111] Soyama, H. "Surface mechanics design by cavitation peening." The Journal of Engineering, 2015(13) (2015): 110-114. https://doi.org/10.1049/joe.2015.0055

[112] Kim, K., Chahine, G., Franc, J., and Karimi, A., "Advanced experimental and numerical techniques for cavitation erosion prediction". Vol. 106. Springer, 2014.

[113] ANSYS Fluent 12.0 Theory Guide, ANSYS Inc.

[114] S.A. Orszag, V. Yakhot, W.S. Flannery, F. Boysan, D. Choudhury, J. Maruzewski, and B. Patel." Renormalization Group Modeling and Turbulence Simulations." In International Conference on Near-Wall Turbulent Flows, Tempe, Arizona, 1993.

[115] Smirnov, P. and Menter, F. Predictions of basic turbulent flows with Fluent. Fluent Validation Report

[116] Jan,H. and Müller, M. "Calibration of PVDF Film Transducers for the Cavitation Impact Measurement." EPJ Web of Conferences Vol. 180. (2018): 1-4. https://doi.org/10.1051/epjconf/201818002036

[117] Bai, F., Wang, L., Yang, K., He, Z., Liu, C., and Twiefel, J. "A novel inner surface enhancement method for holes utilizing ultrasonic cavitation." Ultrasonics (2021) 115: 106453. https://doi.org/10.1016/j.ultras.2021.106453

[118] Brennen, C. "Cavitation and bubble dynamics." Cambridge University Press, New York 2014.

[119] Li, B., Youwei G., and Min C. "Cavitation inception of water with solid nanoparticles: A molecular dynamics study." Ultrasonics Sonochemistry 51 (2019): 120-128. https://doi.org/10.1016/j.ultsonch.2018.10.036